Chemical Industry & Chemical Engineering Quarterly

SERBIA

Belgrade

AChE

The activities of the Association of Chemical Engineers of Serbia are supported by:

**MINISTRY OF SCIENCE,
TECHNOLOGICAL DEVELOPMENT
AND INNOVATION
OF REPUBLIC OF SERBIA**

Faculty of Technology and
Metallurgy, University of Belgrade

Faculty of Science, University of Novi Sad

Institute for Technology of Nuclear
and Other Mineral Raw Materials,
Bekgrade

Faculty of Technology,
University of Novi Sad

Institute of Chemistry, Technology and Metallurgy,
University of Belgrade

Faculty of Technical Sciences
University of Novi Sad

Faculty of Technology,
University of Niš, Leskovac

Faculty of Technical Sciences,
University of Priština, Kosovska Mitrovica

IMS Institute, Belgrade

DCP HEMIGAL
Leskovac

Elixir Prahovo

Chemical Industry & Chemical Engineering CI&CE Quarterly

| Vol. 32 | Belgrade, January-March 2026 | No. 1 |

CONTENTS

PRAKASH CHAKRAPANI[1]

PRAKASH JAYARAMAN[2]

[1]Department of Automobile Engineering, School of Engineering and Technology, Surya Group of Institutions, Anna University, Tamilnadu, India.

[2]Department of Mechanical Engineering, School of Engineering and Technology, Surya Group of Institutions, Anna University, Tamilnadu, India

SLOT MILLING OF AA7075 REINFORCED WITH NANO SILICON CARBIDE PARTICLES - AN EXPERIMENTAL AND FINITE ELEMENT APPROACH

Highlights

- The aluminum nanocomposite is fabricated, and machinability studies are performed.
- The nSiCp reinforcement improves the mechanical characteristics of the AA7075 material.
- Experimental slot milling is performed and cutting force, chip morphology studies are carried out.
- Slot milling is simulated using 3D FEM and the Experimental Vs 3DFEM correlation studies are done.
- The influence of cutting parameters on machinability of the nanocomposite is evaluated.

Abstract

In the current trend, industries prefer to optimize machining processes using finite element-based machining simulation techniques. Aluminum alloy 7075 (AA7075) strengthened with nano silicon carbide particles (nSiCp) is utilized by industries as they exhibit good physical and mechanical properties. Slot milling is the essential machining operation to convert the component to the designed shape and size. However, excellent knowledge is required in selecting the appropriate machining parameters such as cutting velocity, feed, and cutting tool material to ensure the quality of the components milled. In this research work, slot milling operation is carried out in the sample plates of AA7075 fortified with nSiCp content to 1.5% of the weight. A 3D finite element model (3D FEM) is developed using ABAQUS software for simulating slot milling operations to understand the influence of machining parameters on cutting forces, chip formation, and chip morphology. The cutting force signals predicted by 3D FEM correlates 85 to 90% with experimental data. The maximum shear stress of 175 MPa and Von Mises stress of 459 MPa were observed at the tool-workpiece interface. This validated 3D FEM facilitates to visualize and investigate the milling process and assists in selecting appropriate machining parameter settings. The effects of cutting velocity and feed on cutting forces, chip characteristics, stress, and chip formation are reported.

Keywords: Aluminum nanocomposite, slot milling, 3D FEM, cutting forces, chip morphology.

INTRODUCTION

The machinability of the aluminum nanocomposite investigated in this research work is an aluminum-based metal matrix composite (MMC) reinforced with nano SiC particles (<100 nm) to improve the mechanical properties of AA7075 based on the requirements in modern industries.

These MMCs are extensively utilized by the automo-bile and aircraft industries due to their intrinsic mechanical properties when compared to steel such as being lighter in weight, ductility, good stiffness, fracture toughness, and corrosion resistance even at extreme operating conditions. It attracts the attention of researchers and makes it necessary to investigate the machinability of aluminum-based nanocomposites [1-3]. It has been projected that, by 2025 the increase in utilization of aluminum in a car will reach 250 kg from 150 kg as of now [4].

The aluminum-based MMCs reinforced with SiC parti-cles have potential applications in the aviation and trans-port fields, bearings, fins of aircraft fuselage, struts of avionics systems and aero engine compressor blades [5],

brake wheels of four-wheelers and high-speed trains [6]. The milling process is mostly utilized to bring the raw material / semi-finished product to the designed shape and size. However, machining defect-free products/components with good quality is challenging in aluminum nano-composite due to the nSiCp reinforcement in aluminum nanocomposite, which is greatly influenced by the machining parameters selected and the machining conditions [7]. The challenging issues in the milling of aluminum-based MMCs are dimensional inaccuracy, chip built-up edge, unstable cutting forces due to reinforcement material (nSiCp), higher cutting forces, surface roughness, stress concentration, accelerated tool wear, exit burr formation, surface finish and reduction of fatigue life, etc. Hence, ensuring the dimensional accuracy, quality, and reliability of the machined components by eradicating these damages caused while machining is very much essential. Moreover, it is also mandatory to explore the basics of machining the MMCs by investigating the importance of the volume and distribution of the nano SiC particles on the damage mechanism of MMC, the interaction of the mill tool with SiC particles, and the effect of machining parameter combinations (feed rate, depth of cut, cutting velocity, etc.) on dimensional accuracy, quality of the machined surface and ease in machinability. This motivates the engineers, researchers, and industries to investigate on milling of aluminum-based MMC to understand the effects of SiC reinforcement in its machinability [8].

To eradicate the machining difficulties experimental studies are mandatory which is time-consuming and highly expensive, particularly at extensive machinability metrics (i.e. combination of machinery, tool material, tool geometry, machining parameters, and machining environment selected for machining studies) [9]. However, interpreting the experimental results highly depends on the quality of the machinery and data acquisition equipment used. Moreover, it is essential to have a complete understanding of the behavior of metal matrix composites while machining under different machining parameter combinations, which could optimistically ease the machining operations. Hence, the researchers and industries wish to utilize 3D FEM for investigating the machining of MMCs. Using 3D FEM the complex milling process is simulated in three dimensions to predict the cutting forces and cutting stress and to visualize for understanding the chip formation process.

Bhuvanesh *et al.* [10] reported the influence of machining parameters on surface roughness while performing slot milling in aluminum-based hybrid composite strengthened with SiC and B₄C materials. The reduction in plastic deformation is observed with the increased percentage of reinforcement particles while machining. Hence, it is suggested to perform slot milling operations at larger cutting velocities and minimum feed rates to remove the reinforcement material easily and to achieve a good surface finish. Ma *et al.* [11] performed the experimental milling in aluminum alloy 7075 and reported the cutting forces, stress, and chip morphology. The finite element analysis (FEA) simulation studies are also made and the results were correlated with the experimental findings and seem to be similar. Davoudine-jad *et al.* [12]

simulated the slot milling process using a 3D FE model for different machining parameter combinations and reported the cutting forces, chip morphology, cutting temperature, and stress obtained from experimental and finite element (FE) studies.

Raghuvaran *et al.* [13] reviewed the mechanical properties of aluminum-based MMC. It is reported that AMCs find extensive applications in the aerospace and automobile industries and thereby they replace conventional metals and materials. Reinforcement of SiC 10% of weight with AA7075 increases the tensile strength of the composite by 9.67% which creates interest among researchers. Cui *et al.* [14] established a 3D FEM using ABAQUS/Explicit and simulated the milling operation in aluminum alloy 7075-T7451. The authors also reported the cutting force data and chip morphology. Umer *et al.* [15] investigated the subsurface damages caused while machining the aluminum-based MMCs using a 2D FE model. The researchers revealed the machined surface damages such as damage depth, particle debonding, and the effects of cutting velocity and feed on the quality of the machined surface. The researchers also developed 2D micromechanical and 3D equivalent homogeneous models to simulate the orthogonal cutting of aluminum-based (Al359) SiC-reinforced MMC. The EHM model proves its ability in predicting and simulating the cutting process effectively by Umer *et al.* [16]. Zhou *et al.* [17] developed a 2D FEM and simulated the orthogonal cutting process. The researchers reported the effects of machining parameters on residual stress, surface roughness, dimensional accuracy, and shape.

Prakash *et al.* [18] developed a 3D FEM to simulate the slot milling process in unidirectional Carbon fiber-reinforced polymer composites. The investigation reveals how the machining parameters such as cutting velocity and feed influence cutting forces, stress, chip formation, chip morphology, and machining-induced damages. The developed 3D FEM also assists in selecting appropriate machining parameter settings to enhance the machining quality and dimensional accuracy. Prakash *et al.* [19] utilized the developed 3D FEM from the earlier research work and simulated the high-speed milling of AA7075 Reinforced with nB4Cp. The 3D FEM-based milling simulations suggested milling the MMC with higher cutting velocity and at a lower feed rate. Pedroso *et al.* [20] concisely summarised the utilization of FEA strategies for predicting the machining process in INCONEL material and briefed the recent advancements in machining simulations from 2013 to 2023. The review work carried out by the authors revealed the necessity to investigate more for developing new 3D FEMs for enhancing their accuracy and reliability.

Dodla *et al.* [21] studied conventional and ultrasonic vibration-assisted machining of aluminum alloys, titanium alloys, and Inconel – 718 materials. Numerical methods of both machining techniques reported the cutting forces, thermal effects, and chip morphology. The authors suggested utilizing UVA machining to reduce machining forces and machining-induced damages. Deshmukh *et al.* [22] reported a brief review on the machining of aluminum-

based Metal Matrix Composites which guides the researchers to work on cutting tool methodology. The authors reported the recent advancements in the machining of MMCs in their review article. The authors also highlighted the various types of MMCs available and their inherent mechanical behaviors which suit specific industry applications and also create the interest for the researchers to evolve new hybrid MMCs. Liangchi *et al.* [23] reviewed the recent advancements in modeling the machining of fiber-reinforced and particulate-reinforced composites. The review reveals that the accuracy and reliability of the numerical model highly relies on the correctness of constitutive models incorporated in the FEM.

Prakash *et al.* [24-30] have presented a recent work focusing on developing 3D FEM and simulated the drilling and slot milling operation in GFRP, CFRP composites, Aluminum-based MMCs, and investigated the influence of cutting velocity and feed on cutting forces, stress, chip formation, and chip morphology. These researchers provided insight to understand and visualize the drilling and slot milling process in those composites. The experimental findings and 3D FE predictions are excellent in similarity and the developed 3D FE model is novel and reliable in simulating and predicting the optimum machining parameter settings. Prakash Jayaraman *et al.* [31,32], the co-author of this fabricated and investigated the mechanical properties of aluminum nanocomposite, also studied the quality of the holes drilled in the fabricated composite. The researchers suggested AA7075 with 1.5% nSiCp composition is an optimum MMC for wider applications. Since it shows improved mechanical properties as expected by the aerospace industries [33,34].

The literature review reveals that most of the researchers concentrate on developing some 2D and 3D FE Models and simulating the milling process. From the earlier research, it is understood that 3D FE Models are comparatively more reliable and effective in predicting the cutting force data, chip formation process, chip characteristics, and machining-induced damages than 2D FE models. However, the 3D FEM developed so far is not so reliable and efficient in simulating the milling operation in MMCs. Since, it requires huge computation resources, more knowledge in Finite Element studies in developing 3D FEM, time, and complexity in the geometry of the modern tools. Moreover, there are no correlation studies on chip failure and chip characterization from an experiment Vs. FEM simulation particularly in 3D.

Therefore in this research work, slot milling experiments were done in aluminum nanocomposite, followed by the development of a 3D FEM in Abaqus/Explicit. The experimental and FEM simulation results were correlated for FEM validation. Moreover, this validated 3D FE Model is an effective and reliable virtual tool to assist in selecting the optimum machining parameter settings [35] to ease the slot milling process thereby ensuring the dimensional accuracy and quality of the components milled by minimizing the machining-induced damages such as crack formation and surface finish.

METHODOLOGY

Material Selection

In this research work, the aluminum nanocomposite (AA 7075 + 1.5% nSiCp) was fabricated by introducing the nano-sized SiC particles as reinforcement into the matrix of AA7075 aluminum alloy. The reinforced particles (nSiCp) used in this research work were in the 45-65 nm range. AA7075 is a matrix material that owns excellent mechanical properties such as less density, good thermal behavior, high tensile strength, and a better surface. The nano silicon carbide particles possess good mechanical behavior such as heat conductivity, good wear resistance, low thermal expansion coefficient, and good temperature resistance. Hence, SiC was used as the reinforcement material to enhance the mechanical properties of AA7075. The composition of the AA 7075 + 1.5% nSiCp can be referred from the articles of the co-author [31,32].

The aluminum nanocomposite is made up of a stir casting method (shown in Figure 1a) with five different AA7075 + nSiCp compositions and mechanical characterization studies were carried out by Prakash *et al.* [32]. The mechanical properties of the aluminum nanocomposite with the composition, of 985 grams of AA7075 + 15 grams of nSiCp (1.5% by weight) are comparatively outstanding. Therefore, based on the literature review [29,30] and the former research work carried out by the co-author, the suggested composition (AA 7075 + 1.5% nSiCp) was preferred for the current research work. The field emission scanning electron microscope (FESEM) image of the fabricated aluminum nanocomposite was taken using the CARL ZEISS (Model: Sigma with Gemini Column) FESEM equipment. This equipment with features such as a resolution of 1.5 nm, In lens Detector, SE2 detector, and BSD detectors is good enough to capture the surface topography of the fabricated MMC at the required resolution.

The captured FESEM image shown in Figure 1b reveals how SiC nanoparticles are distributed within AA7075 matrix material by Prakash *et al.* [32]. The fabricated aluminum nanocomposite is a very good alternative to steel. The former research carried out by the co-author reveals the enhancement in the mechanical properties, when AA7075 is reinforced with 1.5% nSiCp. The mechanical properties of AA7075 with 1.5% nSiCp are found to be excellent from the earlier studies [32].

EXPERIMENTAL SETUP

The slot milling experiments were carried out in a BMV 51 TC24 vertical milling center with the machining parameters listed in Table 1. Figure 1c shows the experimental setup which comprises of milling center, tool, workpiece, and the mill tool dynamometer with a data-acquisition system. The TiAlN coated solid carbide end mill cutter is used for experiment studies which was supplied by Ultimate Machine Tools, Chennai, India. End Mill Tool – The CoroMill model, which was specially designed for milling composites, is used for this investigation [26]. Moreover, an

end mill cutter with a helix angle of 30^0 and a point angle of 130^0 to 140^0 is selected for this experimental investigation as it is highly preferred by recent researchers and tool manufacturers [9,25,38]. The slot milling experiments were conducted with different cutting velocities and feed combinations presented in Table 1. However, the machining parameter values were selected based on the suggestions of the researchers and the information from the earlier investigations carried out by the authors. The key

(a)

(b)

(c)

Figure 1. a) Stir-casting with ultrasonic cavitation setup [25]; b) FESEM micrograph of the composite [25]; and c) milling experiment set up with Data - acquisition system.

objective of this research was to perform chip morphological studies to evaluate, to report the chip formation and machinability of the aluminum nanocomposite, and to correlate with the 3D FEM simulation studies. This chip correlation study ensured the reliability of the developed 3D FEM. Hence, selecting the moderate and below moderate cutting velocity and feed rate combinations was mandatory for this current research work (given in Table 1). Since the chips obtained for these machining parameter combinations were good enough to visualize and categorize for correlating with FEM results [19,38]. However, the higher cutting velocity with a lower feed rate was preferred to minimize the cutting forces [9] whereas this cutting parameter combination produced very fragile and tiny chips that resembled dust particles. Moreover, these chips were found unsuitable for performing morphological studies. Cutting forces were recorded using

a SYSCON mill tool dynamometer which was supplied by SYSCON Instruments Private Limited, Bangalore, India (shown in Figure 1c). The strain gauge-based milling dynamometer (Max Load capacity of 500 kgf, Model Name - SPL, Type - strain gauge) with full bridge component for each direction was utilized for this experimentation. The acquired analog signal was converted and communicated to the computer through an analog-digital converter, which was then displayed in the form of a graphical output to capture the cutting force data while performing experimental slot milling.

Table 1. Machining parameters settings for experimental slot milling of aluminum nanocomposite.

Machining parameters	Values
Spindle speeds, N (rpm)	250, 500, 1000, 1500
Cutting Velocity, Vc (m/min)	7.85, 15.7, 31.4, 47.1
In feed rate, f (mm/min)	50, 150, 250
Slot depth (mm)	1

Finite element analysis

FEA methodology

In this research work, a Lagrangian 3D FEM was developed to simulate and visualize the slot milling operation in the aluminum nanocomposite using the ABAQUS FEA software [39]. 3D FE simulation trials were performed for different machining parameter combinations given in Table 2 and the critical cutting force, stress, and chip formation phenomenon were predicted (described in the results and discussion section). The milling simulation created by the 3D FEM technique helped in visualizing the interaction of the end mill and the MMC very effectively and provided insight into the machinability of the aluminum nanocomposite from a different perspective. Moreover, 3D FEM is the only effective technique to visualize the dynamic metal cutting process which involves the interaction of complex tool surfaces with workpieces [8].

3D model of tool and aluminum nanocomposite.

The three-dimensional model of the end mill tool with two flutes was modeled in CATIA V5 using the part module [40] (shown in Figure 2a) as per the tool nomenclature described elsewhere [26]. The 3D model of the four fluted end mill cutters was modeled in CATIA V5 and saved in the interactive graphics exchange system (IGES) format which was imported to ABAQUS to develop 3D FEM. The 3D equivalent homogeneous model $(25 \times 25 \times 10)$ mm^3 of the aluminum nanocomposite was created as shown in Figure 2b using the part module in ABAQUS.

3D finite element model

The 3D FEM was developed by assembling and positioning the 3D model of the end mill cutter and the MMC. Furthermore, tool and MMC models were discretized with suitable element types and element numbers based on the requirement to simulate the machining process optimistically (the FE input details are given in Table. 2). Element mesh optimization (selection of suitable mesh
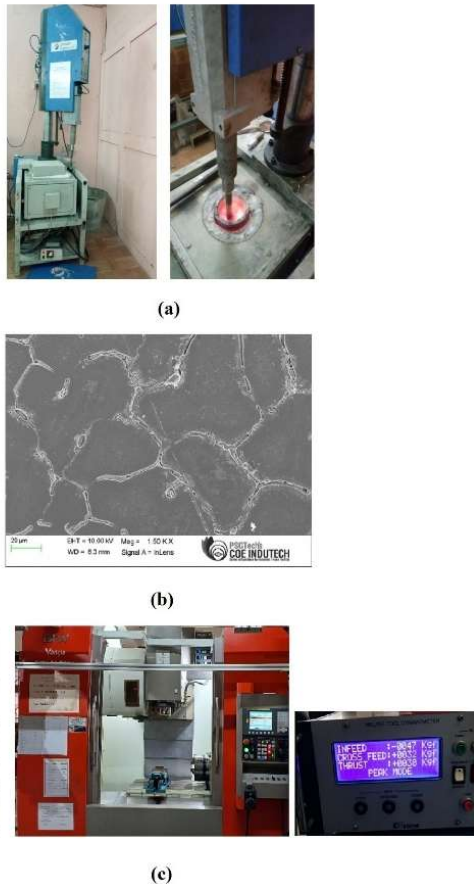
Figure 2. a) Three-dimensional model of the solid carbide end mill cutter and b) three-dimensional finite element model of end milling aluminum nanocomposite.

size) of the 3D FEM is mandatory to simulate the machining process effectively to compromise between the available computational resources, solving time and the efficiency & reliability of the FE results. The 3D model of the end mill tool was considered a rigid body [8,19,39] to reduce the computing efforts. Moreover, the mechanical properties of the mill tool were superior to the MMC, and in addition, tool wear studies were not in focus in the current research work which would be considered in our future investigations.

Table 2. 3D FEM-input data

Workpiece	Aluminum nanocomposite
Tool	End Mill cutter - 10 mm diameter
Dimensions of workpiece (MMC)	25 X 25 X10 mm
Element type for MMC	C3D8R
Number of elements in MMC	50,000
Number of nodes in MMC	54,621
Element size in MMC	0.25 mm
Type of Element in end mill	C3D10M
Number of elements in end mill	32,895
Number of nodes in end mill	49,665
Element size in end mill	1 mm
Total elements & nodes in 3D FEM	82,895 & 1,04,286
Friction factor	0.6 & Coulomb friction [35]
Damage initiation	1E-4
Failure criteria	Johnson-Cook model

The assumptions in developing the 3D FEM for performing slot milling simulation studies are as follows:

- The composite model developed for this current study is an equivalent homogeneous model (EHM).
- The 3D model of the twist drill is assumed to be a

rigid body since tool wear is not considered in the current investigation to reduce computational efforts.

- Tool wear is not considered in this investigation, which is not the main focus of the study.
- In friction modeling the frictional stress developed in the tool-workpiece interaction zone during slot milling operation is proportional to the normal stress.
- Thermal issues are not considered as the temperature recorded during slot milling experimentation is less than 5 °C only, which is kept as our future scope of study.

Material modeling and failure criterion of AA 7075 + 1.5% SiC

The fabricated MMC with the chemical composition listed in Table 3 shows excellent mechanical properties. Johnson's cook failure model available in the material model of the ABAQUS software was incorporated in the developed 3D FEM to simulate the plastic behavior of the aluminum nanocomposite. The Johnson-Cook (J-C) failure criterion (Eq. 1) was preferred for this investigation because it was good enough to predict the cutting forces, stress, chip morphology, flow stress, and plastic deformation for ductile materials and metals. It is widely used by researchers for machining simulation studies [26,41,42]. The features of the J-C parameters are as follows,

Advantages of the J-C failure model in the 3D FEM-based machining simulation [39]

- The J-C failure model is best suited for materials that experience high strain rate, large strain, and larger deformation.
- It also considers plasticity, flow stress, work/strain hardening, and temperature softening of metallic materials.
- The J-C failure model is excellent for exhibiting the material behavior under dynamic (dynamic explicit) situations like machining simulation.
- Supports progressive degradation of material stiffness and removal of mesh elements by incorporating appropriate damage initiation and evolution factors. This assists in chip formation and separation in 3D FEM machining simulation.

Disadvantages and limitations of the J-C failure model in the 3D FEM-based machining simulation [39]

- The seven parameters need to be determined for each structural material, which makes the investigation costlier and time-consuming.
- The solving time of the machining simulation using 3D FEM takes a long time.
- It is mandatory to correlate the simulation results with experimental results to be validated.

The J-C failure criterion is utilized to define the mechanical properties of the aluminum nanocomposite, J-C constitutive material parameters, and J-C damage parameters d_1 to d_5 (all given in Table 3) [42-44]. The damage evolution and element removal are initiated by the J-C damage initiation criterion. At the damage initiation parameter d = 0.001, it facilitates the FEM to activate chip

formation [35]. Enough preliminary trial simulation studies were carried out and appropriate damage initiation parameters were selected.

$$\sigma = (A + B\varepsilon^n)\left(1 + C\,ln\frac{\varepsilon_1}{\varepsilon_0}\right)\left[1 - \left(\frac{T-T_r}{T_m-T_r}\right)^m\right] \qquad (1)$$

The constants A, B, C, n, m, and T are listed in Table 3.

Boundary conditions

The loading conditions (cutting velocity and feed rate combination listed in Table 1) and the boundary conditions

Table 3. Chemical composition, mechanical properties, J-C parameters, and damage criterion of aluminum nanocomposite [17,25].

Composition of aluminum nanocomposite - AA7075 + 1.5% nSiCp (percentage by weight) [27,28]									
Cr	Mg	Zn	Cu	Si	Mn	Ti	Fe	SiC	Al
0.2	2.4	5.7	2.0	0.3	0.1	0.1	0.22	1.5	Bal

Mechanical properties of the composite [25]				
Specifications	Value(s)	Specifications		Value(s)
Modulus of elasticity, E (GPa)	71	Tensile strength (MPa)		285.64
Poisson's ratio	0.27	Yield strength (MPa)		245.12
Thermal expansion coefficient, (1/K)	23.6 E-6	Ultimate strength (MPa)		260.56
Thermal conductivity, k (W/mK)	180	Shear strength (MPa)		150.53
Specific heat (J/kg K)	880	Density of the composite (kg/m3)		2790

Johnson-Cook parameters [35]						
A (MPa)	B (MPa)	n	m	C	Temperature (K)	Damage initiation
251	1443	0.749	1.571	0.0166	305	0.001

Damage parameters				
d_1	d_2	d_3	d_4	d_5
-0.77	1.45	-0.47	0	1.60

that prevailed in the real-time slot milling process were applied to the 3D FEM [24,25]. The aluminum nanocomposite-workpiece FE model was constrained for all degrees of freedom for the outer four sides and the bottom surface (as shown in Figure 2b). The tool was constrained for degrees of freedom except for feed direction (X-axis) and tool rotation axis (rotation along Z-axis). Furthermore, the feed rate and spindle speed values were given as input to the reference point which is created at the tip of the end mill cutter as shown in Figure 2b.

Interaction properties

The coulomb friction concept (sliding and sticking friction) was introduced in the developed 3D FEM which characterized the interaction between the tool and the aluminum nanocomposite (governed by Eq 2). This interaction behavior characterizes the frictional effect produced while performing slot milling operations in the MMCs [45]. The friction coefficient between the composite and end mill cutter was taken as 0.6 [8,42].

$$\tau_n = \mu\sigma_n \qquad (2)$$

RESULTS AND DISCUSSION

Cutting force

The elevated cutting forces developed while machining the MMCs cause machining-induced damages such as surface roughness, dimensional inaccuracy, residual stress, internal cracks, etc. Moreover, the cutting force is

the key parameter that influences more in chip formation, stress, chip morphology, and tool wear while performing slot milling operations in the aluminum nanocomposite. The machining accuracy, quality, and reliability of the machined components are to be ensured by minimizing the milling-induced damages by reducing these cutting forces. However, minimizing the cutting forces while milling is quite challenging, which creates interest for the researchers to investigate machinability studies of MMC. However, evaluating the exact magnitude of critical cutting forces is very difficult which depends on the experimental procedures and quality of the testing equipment utilized [8]. On the other hand 3D FEM technique is the only efficient method to predict these critical cutting forces by simulating the slot milling operation.

Figures 3a and 3b reveal a fluctuating pattern in the cutting force profile since the cutting edge angle varies with respect to the reinforced nano SiC particles while milling the aluminum nanocomposite. Whenever the cutting edge of the end mill interacts with reinforcement material (nano SiC particle) the magnitude of the cutting force increases since the nSiC particles are harder to break down while machining when compared to AA7075 [46]. Moreover, the AA7075 undergoes ductile failure whereas the SiC particle undergoes brittle failure [17]. The cutting force profile acquired from experimental and 3D FE simulations at $Vc = 47.1$ m/min and $f = 150$ mm/min is displayed in Figure 3b.

Figures 3c and 3d show the critical cutting forces generated for the corresponding cutting velocity and rate of feed (also listed in Table 4). Table 4 displays the cutting

feed (also listed in Table 4). Table 4 displays the cutting force components F_x, F_y, and F_z for different cutting parameter combinations. It is also observed that the infeed force, F_x, and the cross-feed force, F_y is comparatively

Figure 3. a) Comparison of experimental and 3D FEM cutting force (Fx) during slot milling of aluminum nanocomposite when Vc = 47.1 m/min and f = 150 mm/min; b) comparison of experimental and 3D FEM cutting force (Fy) during slot milling of aluminum nanocomposite when Vc = 47.1 m/min and f = 150 mm/min; c) cutting velocity and feed rate vs. critical cutting force (Fx); and d) cutting velocity and feed rate vs. critical cutting force (Fy).

higher than the thrust force, F_z. When the slot milling operation is carried out at a higher cutting velocity the cutting forces developed are minimal and vice-versa. Hence, it is highly recommended to perform the slot milling operation in aluminum nanocomposite at higher cutting velocity or lower feed/tooth to minimize the machining-induced damages caused due to critical cutting force [9].

The critical cutting force values captured from the experimental investigation and 3D FE simulation are correlated and the similarity error is found to be in the acceptable range [47]. Figure 3 shows the acceptable deviation of 10 to 15% in the correlation of 3D FE and experimental results which is mainly due to the tool run-out during cutting action [12].

Stress

The shearing action of the end mill cutter when it interfaces with the MMC during the slot milling operation results in chip formation and material removal [25]. Hence, investigating the shear stress developed at the tool-workpiece interface region is vital, since it is the major influencer for chip formation, chip progression, and chip characteristics during the slot milling operation in the aluminum nanocomposite. The significance of the investigation on shear stress generation in the cutting zone is revealed in Figure 4a. The maximum shear stress (S_{12}) observed in the cutting zone is 175 MPa which effectively assists in the shearing of MMC.

3D FE simulation plots revealed that the von Mises stress obtained is 459 MPa (shown in Figure. 4 a) which is greater than the ultimate strength of the MMC listed in Table 3. The highest stress value of 459 MPa is observed in the cutting zone which is mainly due to the strength of the reinforcement material (nSiCp). Especially in the case of AA7075 reinforced with nanoparticles, more plastic deformation of the aluminum matrix is observed which is mainly due to the very high interaction frequency of the tool with the reinforcement particle. This phenomenon is lesser if the reinforcement particle size is larger comparatively by [15]. The highest stress value is observed at the root section of the milled chip (shown in Figure. 4a) which causes the chip to be in the yielding state for some time. This phenomenon results in the formation of curved-shaped chips, lamella structure, and twisted & rolled chip morphologies. Lamella structure in milled chips is observed for a few machining parameter combinations which is particularly due to the strained bands caused by the localized very high plastic von Mises stress during material removal.

Chip formation process in FEA

The 3D FEM developed is utilized and the slot milling operation is simulated which is displayed in Figure 4b. The quality of the machined surface is a vital factor that influences the performance of the milled component from its application point of view. Achieving a good surface finish in the milling of nSiCp-reinforced MMCs very challenging since the formation of scratches and undercutting are quite common [46] which could be avoided only by paying special attention to the selection of suitable cutting velocity and feed. The 3D FEM is an excellent technique in revealing the metal cutting phenomenon to visualize if any machining-induced defect occurs.

Figure 4b reveals the ability of 3D FEM in simulating the chip formation phenomenon while performing slot milling in the aluminum nanocomposite. The effects of the selected cutting velocity and feed-on-chip morphology can
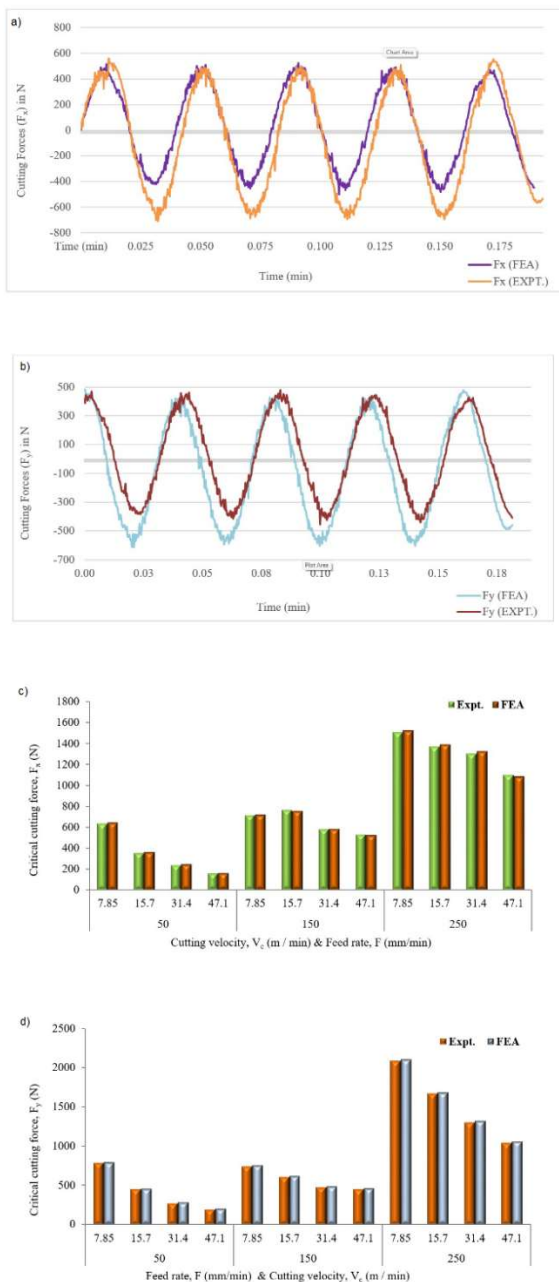
be visualized in 3D FE simulations. The chip morphology is mainly influenced by the shearing effect of the tool with the MMC, a variety of chips with different varieties [12] are obtained for respective cutting velocity and feed combinations which are visualized in Figure 5. The chip flows out of the workpiece through the flute region and it breaks into small curled chips. These small curled 'C' shaped chips are observed for most of the machining parameter combinations which is due to the effect of the interaction of the plastically deformed chip with the rake surface of the end mill cutter. However, the cutting velocity and feed highly influence the chip size, shape, and thickness. Moreover, nano-sized particle reinforcement enhances the yield property of the aluminum matrix [15,16] and thereby plastic deformation occurs easily resulting in the formation of 'C' and 'S' shaped curled chips which are

witnessed in experimental as well as 3D FEM simulation (shown in Figures 4b).

Chip characteristics

Chip morphology and chip formation pattern directly influence the dimensional accuracy, quality, and reliability of the milling operation. Therefore, the effects of cutting velocity and feed-on-chip generation are to be witnessed for a better understanding of chip formation and to facilitate the machining of defect-free components. Moreover, the tool geometry also significantly influences the chip characteristics. Figures 5 and 6 show samples of chips collected from experimental slot milling for various machining parameter combinations. It is witnessed that

Table 4. Critical cutting force data recorded for various cutting velocities and cutting feed combinations.

Feed, f (mm/min)	Cutting velocity, V_c (m/min)	Critical cutting force (N)					
		Infeed (F_x)		Cross Feed (F_y)		Thrust force (F_z)	
		Expt.	FEA	Expt.	FEA	Expt.	FEA
50	7.85	638	647	785	792	118	122
	15.7	353	361	451	462	69	73
	31.4	235	246	275	286	49	46
	47.1	157	162	196	206	39	34
150	7.85	716	719	746	759	167	156
	15.7	765	754	608	619	118	111
	31.4	579	586	481	493	59	57
	47.1	530	524	451	464	49	48
250	7.85	1511	1526	2080	2099	88	86
	15.7	1373	1392	1668	1679	59	55
	31.4	1305	1328	1305	1321	39	34
	47.1	1099	1086	1040	1062	29	27

collected are mostly 'C' shaped with a wider range of sizes, thickness, and length which is mainly influenced by the machining parameter combination selected for slot milling. The formation of a shorter 'C' shaped chip is predominant, which is mainly due to the reinforcement of nSiCp. The even distribution of nano SiC particles in the aluminum nanocomposite improves its ductile behavior, which causes plastic deformation during milling followed by the generation of curved and twisted chips. It is also observed that the chip thickness decreases while increasing the cutting velocity. However, chip thickness increases when the feed rate is increased. A chip with lamella structure is observed when $N = 250$ rpm and $f = 250$ mm/min since the thickness of the chip generated is comparatively higher. Moreover, the stress plots of the chips show highly strained bands across the chips which mainly contributes to the formation of lamellar structure in the milled chips. The

localization of very high plastic Von Mises stress bands is the major contributor to these highly strained bands which results in lamella structure formation [15].

Figure 6a shows the magnified view (5X) of the milled chip at $f = 50$ mm/min and $N = 250$, 500, and 1000 rpm. The chips collected from the slot milling experiments for this particular feed rate mostly reveal very thin, curled, and 'C' shaped morphology. Cracks with saw tooth were observed in these "C" shaped chips which is because of the shearing action of the end mill cutter with the aluminum nanocomposite. Figure 6 (a) shows the magnified photographic images (5X) of the milled chip, $f = 150$ mm/min and $N = 250$, 500, 1000 rpm. In this case, the chip formation is short and thin shaped with lamella structure with cracks and saw tooth.

Mostly the milled chips possess 'C' or 'S' shaped morphology, which is due to the influence of the increased

feed rate when compared to the previous machining parameter conditions [12] for slot milling experimentation. Figure 6a displays the magnified image (5X) of the milled chip at f = 250 mm/min. The milled chips show very good lamella structure at N = 250 rpm which is due to the effect of higher chip thickness. At N = 1000 and 1500 rpm, the chips show twisted and rolled-shaped morphologies.

The chips collected from experimental slot milling show good similarity when correlated with the chip plots captured from 3D FE simulation results as shown in the Figure 6b. The chip images obtained from experimental and 3D FE-based simulations show good similarity. The displayed
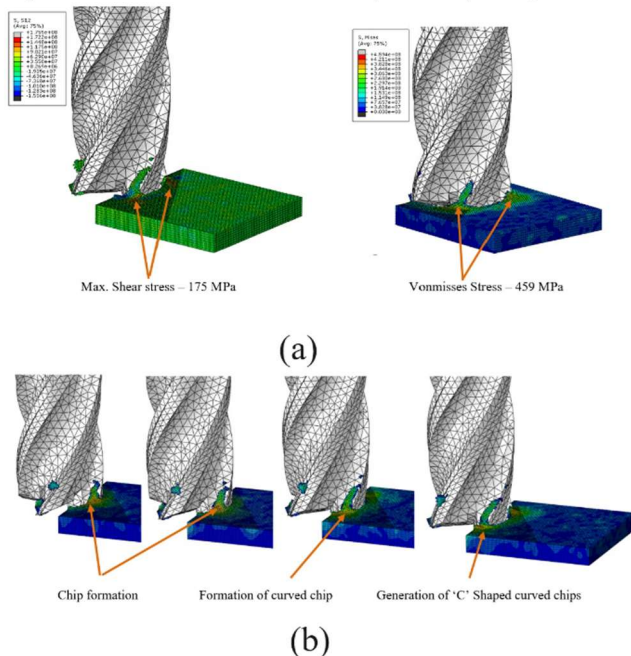
Figure 4. a) Stress Plots from 3D FEA simulation when V_c = 15.7 m/min and feed rate = 50 mm/min; b) 3D FEA slot milling simulation of chip formation at V_c = 15.7 m/min, feed rate = 50 mm/min.

Figure 5. Chip morphology of aluminum nanocomposite while slot milling with different cutting parameter combinations.
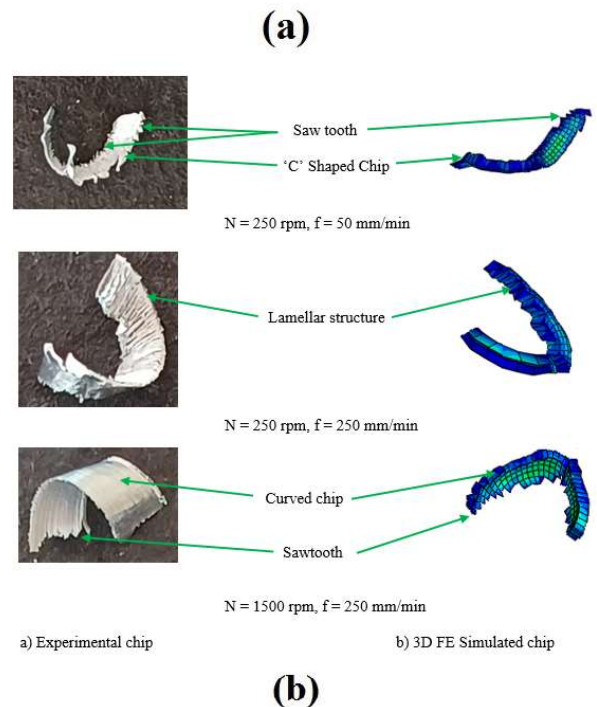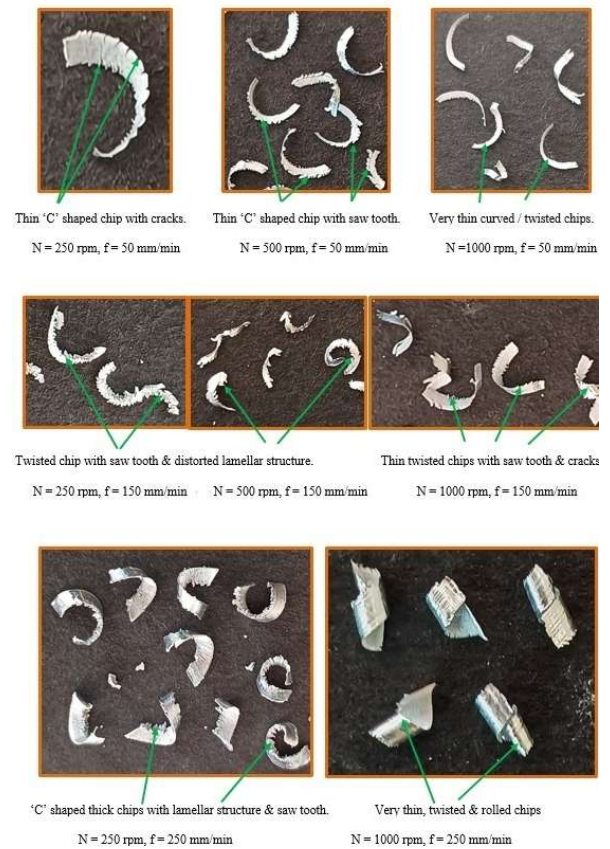
Figure 6. a) Experimental chip characteristics at different spindle speeds and feed and b) comparison of chips morphology - experimental results vs. 3D FE simulation results

images reveal the presence of cracks, lamella structure, and saw teeth. This ensures that 3D FEM-based simulations well exhibit the actual slot milling process and it is also significant in investigating the complex milling operation in a cost-effective and time-consuming way instead of arduous cutting experiments [11,48]. The chip images displayed below show the reliability and

effectiveness of 3D FE simulation in predicting the chip morphology in slot milling of AA 7075 + 1.5% nSiCp nanocomposites.

The dimensions of the milled chip play a major role in enhancing the accuracy, surface finish, and quality of the machined component. The length of the milled chips for most of the cutting conditions is in the 5 to 8 mm range, which is observed from both experimental and 3D FEM simulation results. The cutting depth used in the current research is 1 mm and hence the width of the chips is uniform around 1 mm for all the machining conditions. The experimentation and 3D Fem results reveal that the cutting parameters such as spindle speed and feed rate do not influence on-chip dimensions much. However, the chip thickness varies with respect to cutting speed and feed rate. For higher cutting speeds the thickness of the chip reduces relatively and the chip is fragile.

Future Scope of Study

This research work encourages the researchers and industry to focus more on developing optimistic and reliable 3D FE models to perform machining simulations, which could ease the machining process and make it cost-effective and time-saving. In addition, the 3D FEMs are also capable of estimating critical cutting force, chip characteristics, and cutting stress even for worn-out tools and complex tool geometries. Hence this research work can be extended in the future to investigate further with new tool geometries, MMCs, and other machining operations, which could provide an insight for the industries and researchers.

CONCLUSIONS

The experimental and 3D FEM simulation studies of the slot milling operation were carried out and investigated in aluminum nanocomposite. The 3D FE simulation outcomes are compared with the experimental data for 3D FE model validation. The validated 3D FE model was utilized to perform simulation studies in slot milling of aluminum nanocomposites and it was found to be more reliable and accurate.

Experimental results show that critical cutting force (F_x and F_y) rises when the cutting velocity is reduced. However, when cutting velocity is increased the reduction of critical cutting force is observed, critical cutting force recorded is F_y = 2080 N for V_c = 7.85 m/min and f = 250 mm/min. The low cutting feed and higher cutting velocity are suggested to minimize the milling-induced damages. The cutting force signals predicted by the 3D FEM correlates 85 to 90% with experimental data.

The maximum shear stress, S_{12} = 175 MPa, and von Mises stress, S = 459 Mpa, were observed at the tool-MMC interface region. The chip morphology studies disclose the mode of failure in the milled chips. The chip images captured from 3D FE simulations showed a good correlation with the milled chips. The correlation studies of experimental investigations and 3D FEM-based machining simulations prove the accuracy and reliability of the developed 3D FEM. This 3D FEM could assist researchers and industries in selecting appropriate machining parameter settings to achieve defect-free machining without any machining-induced damages. Moreover, it reduces the machining trials, time, and cost.

Nomenclature

A - yield strength of the material, (MPa)

B - hardening modulus, (MPa)

C - strain rate sensitivity coefficient

D - material constant

f - feed rate, (mm/min)

F_x - infeed force

F_y - cross-feed force

F_z - thrust force

m - temperature sensitivity coefficient

N - spindle speed, (rpm)

n - coefficients related to strain hardening, (MPa)

S - maximum Von Mises stress (MPa)

T - temperature of the parts (∘C)

T_r - ambient temperature (∘C)

T_m - melting temperature (∘C)

V_c - cutting velocity, (m/sec)

Greek symbols:

ε - equivalent plastic strain

ε_1 - equivalent plastic strain rate, (S-1)

ε_0 - reference equivalent plastic strain rate, (S-1)

Σ - flow stress, (MPa)

τ - shear stress, (MPa)

τ_n - frictional stresses, (MPa)

σ_n - normal stresses, (MPa)

σ - Johnson-Cook flow stress, (MPa)

σ_1 - maximum principal stress, (MPa)

μ - coefficient of friction

REFERENCES

[1] Macke, B.F. Schultz, P. Rohatgi, Adv. Mater. Processes 170(3) (2012) 19-23. https://doi.org/10.31399/asm.amp.2012-03.p019.

[2] N. Shetty, S.M. Shahabaz, S.S. Sharma, S. Divakara, Shetty, Compos. Struct. 176 (2017) 790-802. https://doi.org/10.1016/j.compstruct.2017.06.012.

[3] D. Giugliano, N.K. Cho, H. Chen, L. Gentile, Compos. Struct. 218 (2019) 204-216. https://doi.org/10.1016/j.compstruct.2019.03.030.

[4] R. Bach, Aluminum in transport (2020). Available from: https://www.aluminumleader.com/application/transport/[accessed 16th August 2024]

[5] Y. Peng, H. Zhao, J. Ye, M. Yuan, L. Tian, Z. Li, Z. Wang, J. Chen, Compos. Struct. 288 (2022) 115425. https://doi.org/10.1016/j.compstruct.2022.115425.

[6] X.D. Nong, Y.L. Jiang, M. Fang, L. Yu, C.Y. Liu, Int. J. Heat Mass Transfer 108 (2017) 1374-1382. https://doi.org/10.1016/j.ijheatmasstransfer.2016.11.108.

[7] K. Palanikumar, N. Muthukrishnan, K.S. Hariprasad, Mach. Sci. Technol. 12(4) (2008) 529-545. https://doi.org/10.1080/10910340802518850.

[8] K. Giasin, A. Hodzic, V. Phadnis, S. Ayvar-Soberanis, Int. J. Adv. Manuf. Technol. 87(5) (2016) 2041-2061. https://doi.org/10.1007/s00170-016-8563-y.

[9] M. Aamir, K. Giasin, M. Tolouei-Rad, A. Vafadar, J. Mater. Res. Technol. 9(6) (2020) 12484-12500. https://doi.org/10.1016/j.jmrt.2020.09.003.

[10] M. Bhuvanesh Kumar, R. Parameshwaran, K. Deepandurai, S.M. Senthil, Trans. Indian Inst. Met. (2020). https://doi.org/10.1007/s12666-020-01960-6.

[11] W. Ma, R. Wang, X. Zhou, X. Xie, Proc. Inst. Mech. Eng., Part B 235(1-2) (2021) 265-277. https://doi.org/10.1177/0954405420932442.

[12] Davoudinejad, G. Tosello, P. Parenti, M. Annoni, Micromachines 8(6) (2017) 187. https://doi.org/10.3390/mi8060187.

[13] P. Raghuvaran, M. Suresh, S. Aakash, M. Balaji, K. Dinesh Kumar, S. H. Prasath, IOP Conf. Ser. Mater. Sci. Eng. 995 (2020). https://doi.org/10.1088/1757-899X/995/1/012040.

[14] K.H. Cui, C.Z. Ren, G. Chen, Key Eng. Mater. (589-590) (2013) 3-7. https://www.scientific.net/KEM.589-590.3.

[15] U. Usama, A. Hisham, H.A. Mustufa, M.M. Khan, H.A. Kishawy, Adv. Mech. Eng. 13 (2021). https://doi.org/10.1177/16878140211070446.

[16] U. Umer, M.H. Abidi, J.A. Qudeiri, H. Alkhalefah, Mater. Today: Proc. 44 (2021) 764-770. https://doi.org/10.1016/j.matpr.2020.10.679.

[17] L. Zhou, C. Cui, P. Zhang, Int. J. Adv. Manuf. Technol. 91 (2017) 1935-1944. https://doi.org/10.1007/s00170-016-9933-1.

[18] Prakash, K.S. Vijay Sekar, J. Balk. Tribol. Assoc. 23(3) (2017) 497-514.

[19] Prakash, A. Arockia Selvakumar, J. Prakash, AIP Conf. Proc. 3216(1) (2024) 040002. https://doi.org/10.1063/5.0226489

[20] A.F.V. Pedroso, N.P.V. Sebbe, R.D.F.S.Costa, M.L.S. Barbosa, R.C.M. Sales-Contini, F.J.G. Silva, R.D.S.G. Campilho, A.M.P. de Jesus, An Extended Review. J. Manuf. Mater. Process. 8(1) (2024) 37. https://doi.org/10.3390/jmmp8010037.

[21] S. Dodla, K.J. Kirpalani Idnani, A. Katyal, Mater. Today: Proc. (2021). https://doi.org/10.1016/j.matpr.2021.01.136.

[22] S. Deshmukh, G. Joshi, A. Ingle, D. Thakur, Mater. Today: Proc. 46 (2021) 8410-8416. https://doi.org/10.1016/j.matpr.2021.03.450.

[23] L. Zhang, Z. Wu, C. Wu, Q. Wu, Compos. B Eng. 241, (2022) 110023. https://doi.org/10.1016/j.compositesb.2022.110023.

[24] Prakash, K.S. Vijay Sekar, Adv. Sci., Eng. Med. 10(3) (2018) 308-312. https://doi.org/10.1166/asem.2018.2125.

[25] C. Prakash, K.S. Vijay Sekar, J. Braz. Soc. Mech. Sci. Eng. 40(6) (2018) 279. https://doi.org/10.1007/s40430-018-1195-4.

[26] C. Prakash, K.S. Vijay Sekar, IOSR J. Eng. (2018) 22-28. https://iosrjen.org/Papers/ICPRASET%202K18/surya/Volume%201/auto/5.%2022-28.pdf.

[27] C. Prakash, K.S. Vijay Sekar, Lect. Notes Mech. Eng. (2019) 81-89. https://doi.org/10.1007/978-981-13-1724-8_8.

[28] C. Prakash, K.S. Vijay Sekar, IOP Conf. Ser. Mater. Sci. Eng. (2021). https://doi.org/10.1088/1757-899X/1128/1/012050.

[29] C. Prakash, A. Arockia Selvakumar, K.S. Vijay Sekar, Mater. Today: Proc. (2023). https://doi.org/10.1016/j.matpr.2023.08.234.

[30] C. Prakash, Int. J. Interact. Des. Manuf. (2024). https://doi.org/10.1007/s12008-024-02089-2.

[31] J. Prakash, S. Gopalakannan, Silicon 13 (2021) 409-432. https://doi.org/10.1007/s12633-020-00434-0.

[32] J. Prakash, S. Gopalakannan, V.K. Chakravarthy, Silicon 14(4) (2022) 1683-1694. https://doi.org/10.1007/s12633-021-00979-8.

[33] H. Liu, W. Zhu, H. Dong, Ke. Yinglin, Mechatronics 46 (2017) 101-114. https://doi.org/10.1016/j.mechatronics.2017.07.004.

[34] R.K. Bhushan, Adv. Compos. Hybrid Mater. 4(1) (2021) 74-85. https://doi.org/10.1007/s42114-020-00175-z.

[35] Boughdiri, T. Mabrouki, R. Zitoune, K. Giasin, M.F. Ameur, Compos. Struct. 304 (2023) 116458. https://doi.org/10.1016/j.compstruct.2022.116458.

[36] T. Ozben, E. Kilickap, O. Çakır, J. Mater. Process. Technol. 198(1-3) (2008) 220-225. https://doi.org/10.1016/j.jmatprotec.2007.06.082.

[37] S. Deshmukh, G. Joshi, A. Ingle, D.S. Thakur, Mater. Today: Proc. 46(17) (2021) 8410-8416. https://doi.org/10.1016/j.matpr.2021.03.450.

[38] S.S. Babu, C. Dhanasekaran, G. Anbuchezhiyan, K. Palani, Eng. Res. Express. 4 (2022) 025036. https://doi.org/10.1088/2631-8695/ac7038.

[39] Simulia, Abaqus 6.14 User's Manual (2014) Dassault systems.

[40] CATIA V5R14, User Manual (2014) Dassault systems. https://www.maruf.ca/files/catiahelp/CATIA_P3_default.htm.

[41] T. Mabrouki, F. Girardin, M. Asad, J.F. Rigal, Int. J. Mach. Tools Manuf. 48 (2008) 1187-97. https://doi.org/10.1016/j.ijmachtools.2008.03.013.

[42] C. Prakash, J. Prakash, Proc. Inst. Mech. Eng., Part D (2024). https://doi.org/10.1177/09544070241254148.

[43] Johnson, W. Cook, Eng. Fract. Mech. 21(1) (1985) 31-48. https://doi.org/10.1016/00137944(85)90052-9.

[44] S. Rasaee, A.H. Mirzaei, D. Almasi, Bull. Mater. Sci. 43(1) (2020) 1-8. https://doi.org/10.1007/s12034-019-1987-x.

[45] J.Y. Sheikh-Ahmad, Textbook of Machining of Polymer Composites, Springer New York, NY (2009). https://doi.org/10.1007/978-0-387-68619-6.

[46] Yu, Z. He, J. Li, Int. J. Adv. Manuf. Technol. 124 (2023) 97-110. https://doi.org/10.1007/s00170-022-10476-w.

[47] Li, M. Liu, S. Zhao, Mach. Sci. Technol. 25(4) (2021) 558-584. https://doi.org/10.1080/10910344.2020.1855651.

[48] C. Prakash, J. Prakash, Arch. Metall. Mater. 70(2) (2025) 583-600. https://doi.org/10.24425/amm.2025.153459.

PRAKASH CHAKRAPANI[1]

PRAKASH JAYARAMAN[2]

[1]Department of Automobile Engineering, School of Engineering and Technology, Surya Group of Institutions, Anna University, Tamilnadu, India.

[2]Department of Mechanical Engineering, School of Engineering and Technology, Surya Group of Institutions, Anna University, Tamilnadu, India.

NAUČNI RAD

GLODANJE OTVORA NA PLOČAMA OD LEGURE AA7075 POJAČANE NANOČESTICIMA SILICIJUM-KARBIDA – EKSPERIMENTALNI PRISTUP I MODELOVANJE KONAČNIM ELEMENTIMA

U trenutnom trendu, industrije radije optimizuju procese obrade koristeći tehnike simulacije obrade zasnovane na konačnim elementima. Legura aluminijuma 7075 (AA7075) ojačana nanočesticama silicijum-karbida se koristi u industriji jer pokazuju dobra fizička i mehanička svojstva. Glodanje otvora je suštinska operacija mašinske obrade za pretvaranje komponente u projektovani oblik i veličinu. Međutim, potrebno je odlično znanje u odabiru odgovarajućih parametara obrade, kao što su brzina rezanja, pomak i materijal reznog alata, kako bi se osigurao kvalitet glodanih komponenti. U ovom istraživačkom radu, operacija glodanja otvora je izvedena na pločama uzorka od AA7075 obogaćenom nanočesticama silicijum-karbida do 1,5% težine. 3D model konačnih elemenata (3D FEM) je razvijen korišćenjem softvera ABAQUS za simulaciju operacija glodanja otvora da bi se razumeo uticaj parametara obrade na sile rezanja, formiranje strugotine i morfologiju strugotine. Sile rezanja predviđene 3D FEM modelom koreliraju 85% do 90% sa eksperimentalnim podacima. Maksimalni napon smicanja od 175 MPa i Fon Mizesov napon od 459 MPa primećeni su na interfejsu alat-obradak. Ovaj validirani 3D FEM olakšava vizualizaciju i istraživanje procesa glodanja i pomaže u odabiru odgovarajućih postavki parametara obrade. Prikazani su efekti brzine rezanja na sile rezanja, karakteristike strugotine, naprezanje i formiranje strugotine.

Ključne reči: Aluminijumski nanokompozit, glodanje otvora, 3D FEM, sile rezanja, morfologija strugotina.

SEMAA IBRAHEEM
KHALEEL

University of Mosul, College of
Petroleum and Mining
Engineering, Department of
Petroleum and Refining
Engineering, Mosul, Iraq

SYNTHESIS AND CHARACTERIZATION OF ACTIVATED CARBON PRODUCED FROM HAZELNUT- PEELS BY CHEMICAL ACTIVATION

Highlights

- The objective is to study the effect of the composite depressant additive (CDA).
- Assumptions were made regarding the mechanism of paraffin crystal formation.
- The developed composite additive exhibits high depressant activity.

Abstract

Activated carbon was prepared in this research from hazelnut (Corylus avellana) peels with some additives, which included polymeric waste (polymethyl methacrylate, PMMA), and the raw material was ground to facilitate handling and different amounts of sodium hydroxide were added to it and the ratio peels:NaOH was 1:0.5-1:2.5. The peels were also treated with polymeric waste materials at ratios of 5-25% and a basic ratio of 1:2 at a temperature of 550 °C as it is considered an environmental pollutant and then part of it was disposed of by preparing a material with great economic feasibility. Then, the adsorption properties of the prepared samples (methylene dye), iodine number, density, humidity, and yield were evaluated and compared with the British and Russian commercial models, and SEM, and FT-IR techniques were used to characterize the prepared activated samples. The results showed that activated carbon samples prepared from hazelnut peels were characterized by a high iodine number (895 mg/g), methylene blue dye adsorption capacity (98.4 mg/g), and yield (15.0%). As for the samples prepared from hazelnut peels with PMMA, an increase was observed in the iodine values (1015 mg/g) and the adsorption capacity for methylene blue dye reached (148 mg/g) and yield also increased. This indicates that the addition process was a positive step in improving the specifications and productivity of activated carbon. As for the density and ash, humidity values, they were within the permissible limits for all the prepared activated carbon samples, and thus they greatly exceeded the specifications of commercial carbon samples.

Keywords: Carbonation, polymeric waste, polymethyl methacrylate, methylene blue dye, physical properties.

INTRODUCTION

Activated carbon can be defined as a carbon material that has high porosity as well as a large surface area between particles, which is ready for chemical reactions or adsorption [1,2]. The pore size distribution of activated carbon and its adsorption properties depend on the chemical composition and physical properties of the primary material as well as the process conditions and methods used for activation [3]. The composition of matter is one of the factors that distinguish one from the other. Whereas cellulose, lignin, and materials that contain large percentages of lignin, such as cherry pits and grape seeds, develop activated carbon with a predominance of large pores, while other raw materials that contain large percentages of cellulose, such as almond shells and apricot stones, produce activated carbon with a highly porous structure mostly [4,5].

Activated carbon is used in various media, such as liquid and gaseous, either in powder or granular form. It is applied in liquids by treating water by removing compounds

that affect taste, smell, and color. It can also be used to purify proteins or separate metal compounds such as gold and silver [1]. Activated carbon is mainly prepared in two ways: chemical activation and physical activation. It is manufactured in two basic stages: the first includes carbonization of the raw material and the second includes activated coal. The first method includes carbonizing the raw material and then activating it at a high temperature in the presence of steam or carbon dioxide, while the second method includes carbonating the raw material that was previously impregnated using a chemical agent such as potassium hydroxide [6], zinc chloride [7], and phosphoric acid [8]. Activated carbon is prepared from many resources that depend on plants as a raw material.

Kumar and Jena [9] prepared activated carbon from fox nut (Euryale ferox) shells by chemical activation with H_3PO_4 in a nitrogen atmosphere. The effect of both temperature and impregnation ratio was studied and found that the best activation temperature was 700 °C with an impregnation ratio of 1.5 and a time of activation of one hour. It was also found that the surface area of the prepared activated carbon was 2636 m^2/g and contained many active groups. Jamion and Hashim [10] prepared activated carbon from tamarind seeds Tamarindus indica and activated it using phosphoric acid in a ratio of 1:1 at a temperature of 500 °C for 4 hours. The BET surface area analysis gave a value of 594 m^2/g. The Field emission scanning electron microscopy (FESEM) analysis showed that the development and formation of pores were mostly in a circular and oval pattern and the highest adsorption capacity for methylene blue (MB) dye was equal to 103 mg/g).

Ramalingam et al. [11] prepared activated carbon from dead (Eucalyptus tereticornis) and neem (Azadirachta indica) leaves by washing, drying, grinding, and mixing them in equal proportions and placing them in an oven at a high temperature of up to 750 °C for 6 hours. The carbon powders were then characterized. The results obtained using scanning electron microscopy (SEM), Energy dispersive X-ray analysis (EDAX), and X-ray diffraction (XRD) analyses showed that the prepared carbon has good properties that enable it to be used in medical fields. Viena et al. [12] prepared activated carbon from banana peels using different activation agents like H_2SO_4, KOH, and $ZnCl_2$ for three hours. The resulting activated carbon had a low moisture content and better ability to absorb iodine and was used as an adsorbent to remove gases emitted from motorcycles.

Mistar et al. [13] were able to produce activated carbon from the plant Bambusa vulgaris striata through a chemical activation process using KOH [1:3] and an activation temperature of 800 °C for an hour. The porosity and advanced surface chemistry were examined using BET, SEM, and Fourier transform Infrared spectrum (FTIR) analyses. The BET results were 980 m^2/g , and the SEM images showed an advanced development of high porosity. Using FTIR technology, it was found that its surface contains different functional groups. Abudaia [14] was able to prepare activated carbon from rice hulls and corncobs as an available and inexpensive material to study the

absorption of dimethoate from its aqueous solution. It was prepared by chemical activation with KOH and obtained a high yield, so it can be used in wide application fields. It was concluded that it is possible to use agricultural residue with low cost, such as rice husk and corncob adsorbent materials to remove water pollutants due to their high ability to absorb various pollutants. Ramutshatsha-Makhwedzha et al. [15] were able to manufacture an activated carbon derived from orange and lemon peels using H_3PO_4. Characterization was performed on OLAPC and the material was used to remove methyl orange and MB dyes from wastewater. The method was successfully applicable to real wastewater samples with a satisfactory percentage of methyl orange and MB removal of 99%. Islam et al. [16] prepared activated carbon from jute sticks by chemical activation using H_3PO_4, $ZnCl_2$, and H_2SO_4 to study the effect of activation factors and carbonization temperatures in a range of 300-350 °C. The properties of prepared samples were studied by iodine absorption and FTIR spectroscopy.

Gomaa et al. [17] prepared activated carbon from olive seed residue by chemical treatment with KOH (1:1), then dried at a temperature of 150 °C for 60 minutes, where 100 g of the material was activated at 250, 350, 450, and 550 °C for 15, 20, 25, and 30 minutes at 1, 3, 1.6, and 1.9 bars in the presence of nitrogen at a flow rate of 50 cm3/min. The results indicated that the surface area of the prepared activated carbon had a significant effect, which amounted to 1092 m^2/g at an uttermost rotation of 1100 mg/g, a temperature of 450 °C, and an activation time of 25 minutes.

Sarici et al. [18] were able to prepare activated carbon from hazelnut shells using potassium carbonate for activation at different ratios of 1:1, 1:2, and 1:3 and carried out a carbonization process under nitrogen gas pressure and characterized the prepared activated carbon using X-ray, FT-IR, and SEM techniques after drying the sample. The BET value was equal to 644 m^2/g while the absorption numbers of iodine and MB dye were equal to 489 mg/g and 1974 mg/L, respectively. They also conducted a thermodynamic and kinetic study.

Altintig et al. [19] prepared activated carbon from hazelnut shells using H_3PO_4 as an activating agent. And coated with silver ions to prepare nanoparticles and mixed them in different ratios (1:0.5 or 1:1) using the chemical reduction method. It was found that the prepared activated carbon has a high adsorption capacity through the BET value equal to 1208 m^2/g. The results showed that the prepared model contains 66.01% carbon with an efficiency rate of 36.22%. The prepared activated carbon was distinguished by its use in drinking water applications.

Abo Hay Allah and Alshamsi [20] prepared activated carbon from Pontederia rassipe leaves and used it to remove Malachite Green, Congo Red dyes. The prepared materials were studied using diagnostic techniques including FT-IR, XRD, SEM, EDX, and TEM. Raman results showed that the optimum efficiency for removing both dyes was achieved at 98.9% for Congo Red dye and 99.2% for Malachite Green dye.

Olam [21] was able to carbonize waste coffee and

duckweed together and separately at 800 °C and N₂ (flow rate of 100 ml/min) in a tubular reactor for 90 minutes and the results showed that it is an effective adsorbent for removing Crystal Violet dye from wastewater with a removal rate of 83%. He was also able to prepare activated carbon by carbonizing gelidium corneum at a temperature of 800 ºC for 90 minutes. The prepared activated carbon was characterized using SEM, EDX, FT-IR, XRD, and UV, and it was found a suitable adsorbent for removing dyes from their aqueous solutions [22]. He prepared activated carbon by carbonizing Lemna minor and hazelnut shell at a temperature of 800 ºC in the presence of N₂ (100 mL/min) for 90 minutes. The prepared activated carbon was examined using spectroscopic methods, which showed that the resulting carbon is a good adsorbent for removing Crystal Violet dye, as the adsorption capacity reached about 88 mg/g while and the removal capacity was 88% [23].

Khaleel *et. al* [24] prepared activated carbon from pomegranate peels alone and treated it with polymeric additives (Novolak resin) and asphalt by carbonization and activation at a temperature of 550 ± 25 °C using potassium hydroxide in different proportions. It was found that the best proportion was 1:2.5. The prepared activated carbon samples were excellent adsorbents for removing Bromocresol Green and Bromocresol Purple dyes from their aqueous solutions.

In this research, activated carbon was prepared from Corylus avellana peels with some additives from polymeric wastes, which are environmental pollutants, using the method of carbonization and activation by NaOH. The prepared samples had very excellent adsorption properties compared to the British and Russian commercial models.

EXPERIMENTAL

Materials

In this research, hazelnut peel residues (plant waste), polymethyl methacrylate (PMMA, polymer waste) NaOH with 99% purity (Fluka), HCl with 98% purity, iodine, starch, sodium thiosulfate with 95% purity (Fluka), potassium iodide with 99% purity, and MB dye with 97% purity (B.D.H.).

Instrumentation

A UV-9200 spectrophotometer (Biotechnology Engineering, UK) was used to make a calibration curve for MB dye at λ_{max} = 665 nm. The surface morphology of the materials was characterized using scanning electron microscopy (India). A Fourier transform infrared (FT-IR) absorption spectrophotometer) was from Bruker-Optics (German).

Preparation of Activated Carbon

Activated carbon was prepared by performing several steps as follows:

Preparation of the raw material: The raw material was taken from *C. avellana* peels in its natural, dry form, then ground and made into a fine powder to react with the carbonated material completely and to obtain good results.

Primary carbonization process: 10 g of the powdered material was mixed with various weight proportions of *C. avellana* peels:NaOH (1:0.5, 1:1, 1:1.5, 1:2, or 1:2.5). In a stainless steel crucible, the mixture was homogenized well by adding 5-10 ml of water, then heated to a temperature of 450 °C with continuous stirring for 3 hours until the release of gases stopped.

Final carbonization and activation process: After completing the initial carbonization of the *C. avellana* peels, the temperature was raised to (550 °C) for 2.5 hours to complete the process of carbonization, activation of prepared carbon samples, after which the models were left to cool to laboratory temperature.

Purification of activated carbon: The prepared activated carbon was washed with water repeatedly until samples that did not contain sodium hydroxide and metallic components were obtained. Then, it was washed with a 10% hydrochloric acid solution with thermal sublimation for an hour to remove ions and then washed many times with water until it ensured free from traces of acid. The resulting carbon samples were dried at 120 °C for 24 hours, crushed well, and kept in a dryer isolated from air and moisture.

Preparation of carbon from a mixture of *C. avellana* peels and PMMA: PMMA sheets were cut into small pieces and placed in a ceramic crucible covered with aluminum foil. Then, the lid was heated in an oven at 350 ºC for 3 hours, taken out, left to cool to the laboratory temperature, and crushed into a fine powder using a mortar. Certain amounts of carbonated *C. avellana* peels were taken as primary carbonation, and thermally crushed polymeric waste was added in ratios of 5, 10, 15, 20, and 25% and the steps above were repeated, using a fixed *C. avellana* peels:NaOH ratio of 1:2 as the best one to prepare activated carbon from *C. avellana* peels.

Measurements for determining the effectiveness

To determine the effectiveness of the activated carbon that was prepared, several measurements were performed on it, as shown below:

1. Measurement of the iodine number of activated carbon [25]: It is one of the well-known and common methods for giving information about the internal surface area of carbon that is activated. It is expressed as the number of milligrams of iodine, adsorbed from the solution (1 g) from carbon. It includes the following:

- 1 g of carbon was placed in a 250 mL conical flask.
- 100 mL of a 5% HCl solution was transferred using a pipette to the conical flask.
- The conical flask was heated until it boiled for 0.5 h, then left to cool at the temperature of the laboratory.
- 100 ml of 0.1N iodine solution was placed in the conical flask using a pipette.
- The conical flask was shaken on an electric shaking device for a period of half a minute, and the contents of the conical flask were then filtered. Approximately 20-25 mL of the filtrate was discarded at the beginning of the filtering process, then the remainder was collected in a clean conical flask.
- 50 mL of the filtrate obtained from the previous step

KHALEE: SYNTHESIS AND CHARACTERIZATION…

Chem. Ind. Chem. Eng. Q. 32 (1) 15-24 (2026)

was placed in a 250 mL conical flask and flushed with a standard 0.1N sodium thiosulphate solution until the color of the solution became pale yellow. Then, 1 mL of the starch indicator was added and the clarification was completed until the blue color of the starch indicator no longer appeared. The volume of thiosulfate used was calculated, and the iodine number (*IN*) was also computed through this equation:

$$IN = WIO/WAC \cdot CF \qquad (1)$$

where *WIO* is the weight of iodine adsorbed in milligrams, *WAC* is the weight of activated carbon prepared, and *CF* is the correcting factor.

2. Measurement of the adsorption capacity of prepared carbon samples to MB dye: The external surface area of the activated carbon was measured by taking 0.1g of dry activated carbon and placing it in a 250 mL conical flask. A certain amount (20 ppm) of MB dye was added, then the flask was placed in an electric shaking device for 24 h until became colorless, also another amount of the dye solution was added, thus increasing the unadsorbed dye. After that, the solution was centrifuged, and the absorbance of the clear solution was measured at λ_{max} = 665 nm The standard curve was prepared by taking different concentrations of the dye solution, ranging from 5 to 25 ppm with an increase of 5 ppm, and measuring the absorbance of the solution at the same wavelength mentioned above, then the relationship between concentration and absorbency was drawn [26].

3. Calculation of the humidity percentage: This method involved exposing the activated carbon to the laboratory temperature for 24 h, then drying it at 140 °C for 2 h. After cooling and weighing it accurately, the humidity percentage was calculated [27].

4. Ash content measurement: The ash content was measured by placing 1 g of the prepared carbon in a ceramic crucible in an oven at 1000 °C for an hour, leaving it to cool, and weighing it. The ash content was then calculated for each sample [28].

5. Density measurement of activated carbon: A certain weight of activated carbon was placed in a 5 mL volumetric flask, carefully compacted until the carbon occupied the entire volume of the bottle, and weighed using an accurate balance. Density was calculated by Eq. (2) [29]:

$$Density \ g/cm^3 = Mass/Volume \qquad (2)$$

6. Calculation of the yield of activated carbon: The yield was calculated from the weights of the raw, carbonated, and activated materials using Eq. (3) [30]:

$$yield = w_c/w_o \times 100 \qquad (3)$$

where w_c is the final dry product weight (g) and w_o is the dry raw weight (g).

RESULTS AND DISCUSSION

Activated carbon is considered porous. Its chemical structure suffers from a crystalline defect, leading to the appearance of pores that are energetically or effectively unstable. It is produced from raw materials with a high carbon content, such as bituminous materials and wood rich in lignin, using thermal carbonization processes that remove hydrogen and leave it rich in carbon. The resulting carbon is then activated thermally in an atmosphere of argon, nitrogen, or steam at high temperatures.

Due to the advantages that activated carbon possesses, it has been used in various fields, such as removing dyes, treating pollution, and reducing its damage. In addition to the availability of primary raw materials, researchers were encouraged to prepare them in a variety of ways. It was produced from plant sources, especially those in which lignin is abundant, i.e. nut shells, hardwoods, etc. In this research, one of the types of nut shells, i.e., *C. avellana* peels, which is unique in its extreme hardness and high lignin content was used for preparing carbon by mixing them dry with sodium hydroxide to remove hydrogen in the form of water and dispose of it thermally. That is, the carbonization process in this case is a fusion melting process followed by a process of loss of water and other gases, resulting in a black mass that is washed and activated with mineral acids.

Sodium hydroxide is considered an influential factor in the activation process, as it works to develop the fine porous structure in producing activated carbon by chemical treatment. In addition, hydroxide ions necrotize the structure of the raw material and thus lead to the development of the porous structure of the produced carbon. Table 1 shows the specifications of the activated carbon samples that were prepared.

It shows that chemical activation using an increased percentage of NaOH leads to increased adsorption of iodine from its solution to the extent of a 1:2 ratio, after which the adsorption value of iodine begins to decrease. Namely, an increase in OH leads to the destruction of part of the pores and a hiatus formed on the surface of the prepared carbon using a ratio of 1:2.5 due to the role of sodium hydroxide in expanding the internal pores. Therefore, the iodine number value increases regularly with the increase of the base added to the original sample.

An increase in the concentration of MB dye adsorbed using the positive portion of sodium hydroxide was also observed, which increased the capacity of the pores and organized them. Comparing it with the commercial models designed by B.D.H. and Russ showed that the amount of iodine absorbed by the prepared activated carbon was much better than both commercial samples. The humidity content values ranged between 7.5% and 9.8%, showing the extent to which the prepared samples could be used in the water vapor adsorption process. Namely, it was found that some prepared carbon samples could absorb water vapor. The ash content was within the permissible limits

Table 1. Specifications of prepared activated carbon from *C. avellana* peels by modified carbonation and chemical treatment.

AC	*C. avellana*:NaOH ratio	IN (mg/g)	MB (mg/g)	Humidity (%)	Ash (%)	Density (g/cm^3)	Yield (%)
AC_0	1:0	412.390	23.721	9.152	3.117	0.401	20.021
AC_1	1:0.5	670.300	64.534	9.835	3.100	0.380	18.572
AC_2	1:1	689.502	70.951	10.029	3.010	0.367	17.514
AC_3	1:1.5	757.280	76.860	11.108	2.958	0.291	16.230
AC_4	1:2	894.521	98.425	12.061	2.100	0.287	14.973
AC_5	1:2.5	789.672	78.002	7.528	3.975	0.293	9.021
CBDH	-----	908.000	90.000	0.800	3.200	0.345	-----
CRuss	-----	61.000	34.800	0.620	1.500	0.325	-----

AC_0 = activated carbon prepared from *C. avellana* peels without any additives.
CBDH [31] = British commercial granular activated carbon.
CRuss [31] = Russian commercial granular activated carbon.
MB = Adsorption capacity of MB.

due to the thermal sublimation process with HCl, which removed the bulk of the metal components. As for the density values, their values were low, being good evidence that the prepared activated carbon had high porosity and thus a high ability to adsorb small molecules. The yield decreased with the increase of the NaOH percentage added to the carbon due to an increase in the percentage of loss in the carbon content of the original material. From Table 1, it is clear that the best sample is AC_4 because of its high effectiveness for adsorbing iodine and methylene dye and its low density. Therefore, activated carbon, which is free of carcinogenic nitrogen and sulfate compounds, can be used in the medical field to absorb gases from the stomach and intestines.

To improve the specifications of the carbon prepared from *C. avellana* peels, the original material was treated by PMMA using a fixed ratio of the base [1:2]. Table 2 shows the specifications of the activated carbon samples prepared from a mixture of *C. avellana* peels with the polymer. The use of polymer as an additive to *C. avellana* peels improved the adsorption properties of activated carbon in terms of iodine value, which increased and reached 1015.02 mg/g. The adsorption capacity of MB dye also increased and reached 148 mg/g. The best model was AC_{10}, which gave the highest value of iodine value that exceeded those of the activated carbon prepared from hazelnut peels alone and a commercial activated carbon. In addition, the values of density and humidity were acceptable. Therefore, it was concluded that the addition process was a positive step in improving the specifications and productivity of activated carbon.

Thermogravimetric analysis of the activated carbon prepared from *C. avellana* was performed as shown in Figure 1, whereas Figures 2-5 illustrate various relationships.
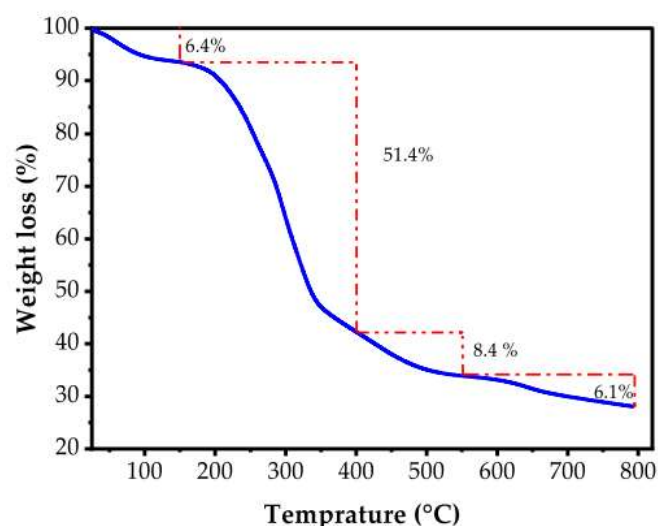
Figure 1. Thermogravimetric analysis of C. avellana peels.

Table 2. Specifications of activated carbon prepared from a mixture of (*C. avellana* peels with PMMA) using [1:2] [raw material: NaOH].

AC	Polymer (%)	IN (mg/g)	MB (mg/g)	Humidity (%)	Ash (%)	Density (g/cm^3)	Yield (%)
AC_6	5	904.217	105.000	12.000	1.975	0.270	15.751
AC_7	10	953.000	117.028	11.831	1.961	0.261	17.090
AC_8	15	997.215	125.000	11.957	1.952	0.246	20.807
AC_9	20	1000.700	137.115	12.280	1.871	0.184	23.465
AC_{10}	25	1015.021	148.000	13.500	1.330	0.103	30.970
CBDH	-----	908.000	90.000	0.800	3.200	0.345	-----
CRuss	-----	61.500	34.800	0.620	1.500	0.325	-----

AC_0 = activated carbon prepared from *C. avellana* peels without any additives.

CBDH [31] = British commercial granular activated carbon.

CRuss [31] = Russian commercial granular activated carbon.

MB = Adsorption capacity of MB.

Activated carbon characterization

SEM: This technique was implemented to evaluate the prepared activated carbon samples. Figure 6 shows the changes in the shape of the samples in terms of size and pore formation. It was noted that the process of adding the PMMA polymer led to the production of different types of pores and cavities on the surface.

FT-IR: The FT-IR spectra of the raw material before carbonization and the material after carbonization and activation are shown in Figure 7 and 8, respectively. The FT-IR spectrum of the raw material before carbonization shows many bands indicated in Table 3, which shows the frequency of each band and the type of bond before carbonization. On the other hand, in the case of the material after carbonization and activation, some of the bundles disappeared and new ones appeared in its FT-IR spectrum, as shown in Table 4.
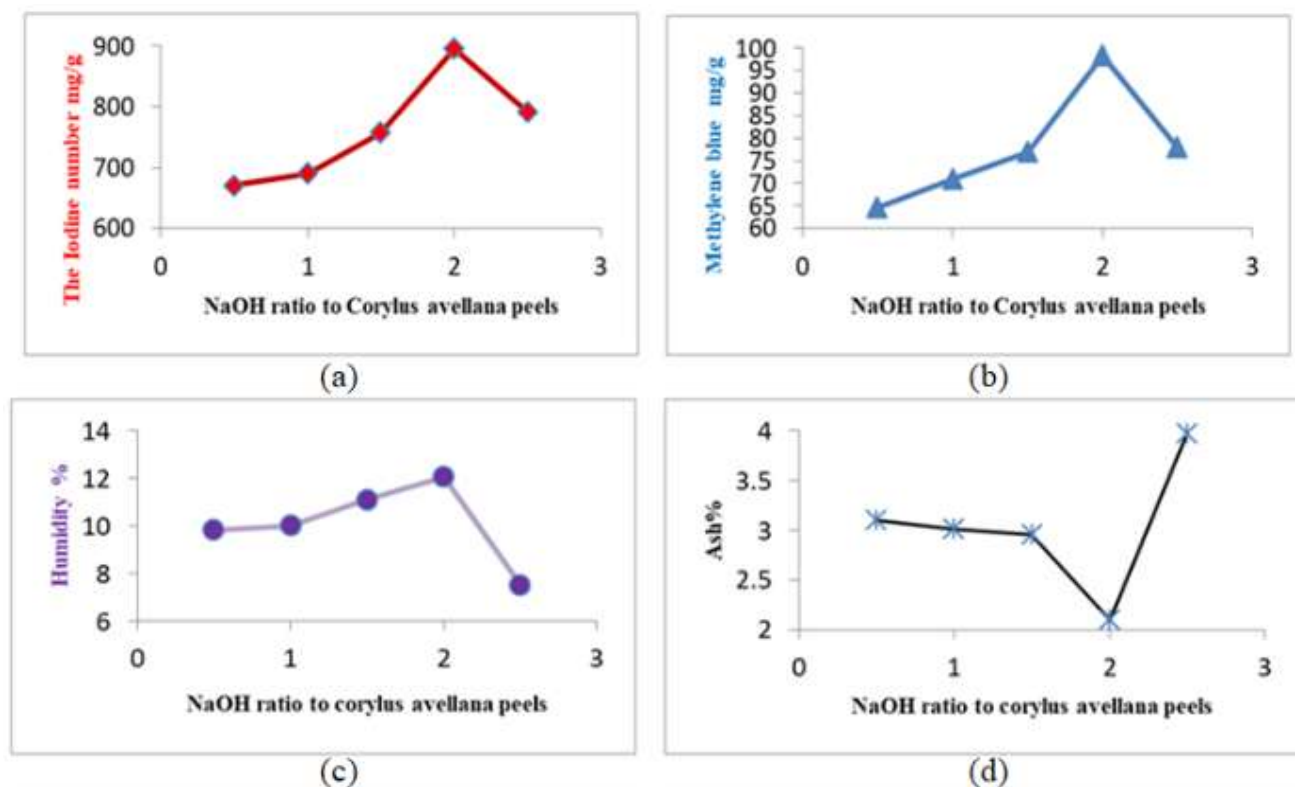
Figure 2. Relationship of the added NaOH ratio and (a) IN, (b) MB, (c) humidity content, and (d) ash content in activated carbon.
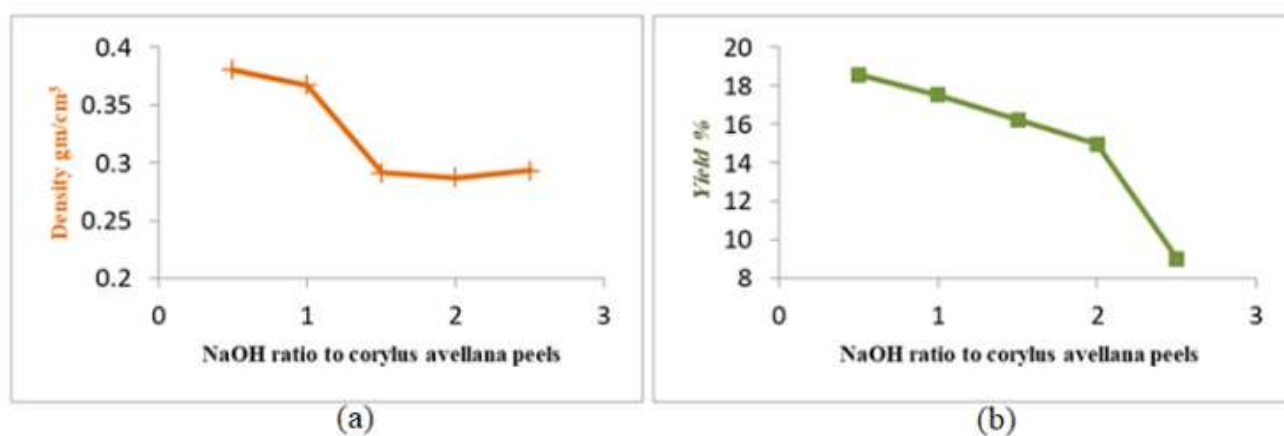
Figure 3. Relationship of the added NaOH ratio and (a) Density and (b) yield in activated carbon.

Table 3. FT-IR spectrum bands for the raw material before carbonization.

Type of bond	Frequency(cm^{-1})
Stretch (O -H)	3308
Stretch (C -H) Aliphatic	2852, 2921
(C= O)Ketone	1731
(C= N)	1605
Stretch (C- C)	1512
Bending (CH$_3$)	1370
Stretch (C -O)	1139
Stretch (C -N)	1021

Table 4. FT-IR spectrum bands of the material after carbonization and activation.

Type of bond	Frequency(cm^{-1})
Stretch (O -H)	3265
Stretch (C- C)	1574
Stretch (N= N)	1416
Stretch (C -N)	1074
Stretch (C -H)	873
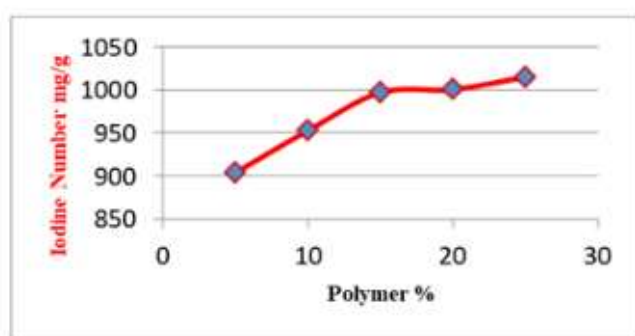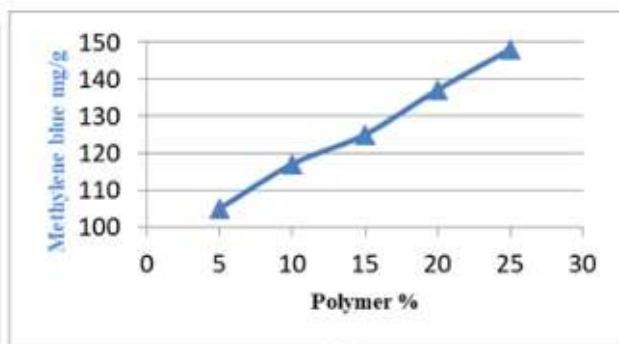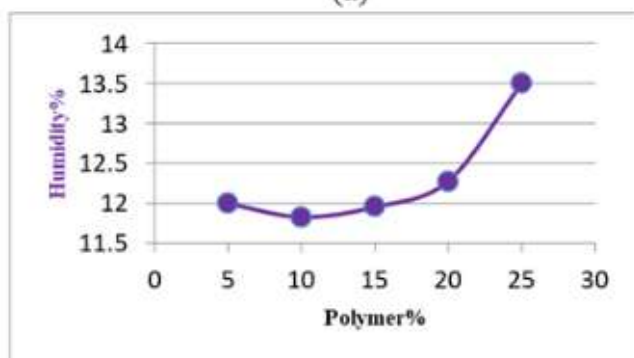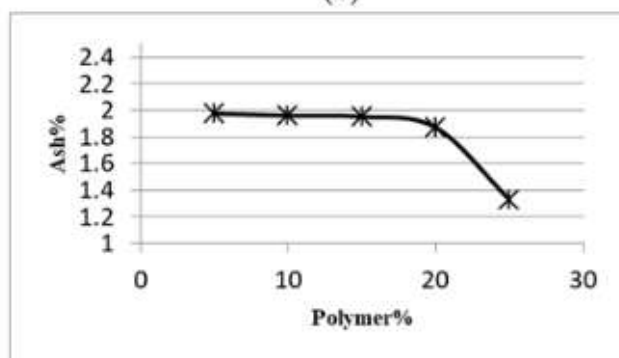
Figure 4. The ratio between the organic glass polymer and (a) IN, (b) MB, (c) humidity content, and (d) ash content, of activated carbon.
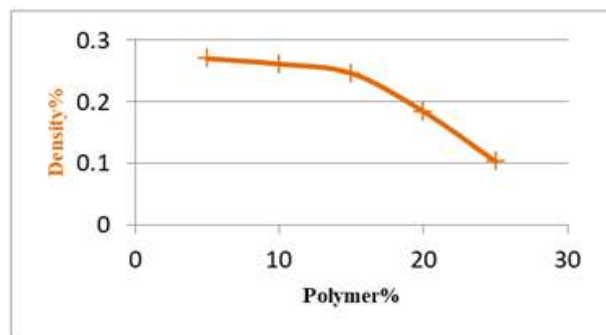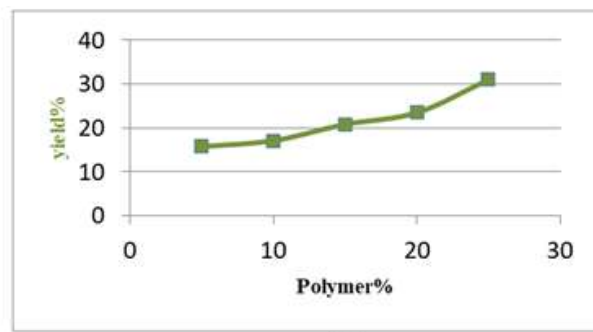
Figure 5. The ratio between the organic glass polymer and (a) Density and (b) yield of activated carbon.
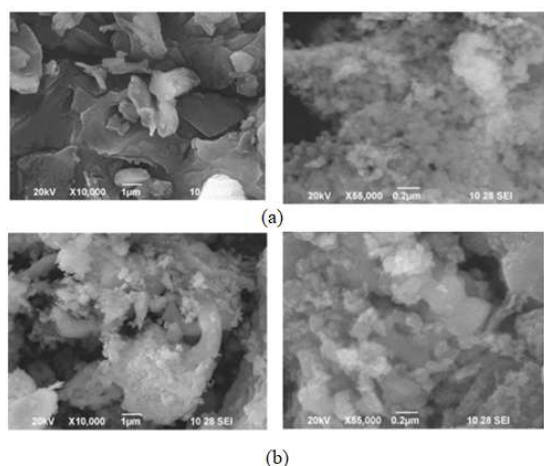
Figure 6. SEM images of activated carbons prepared from (a) C. avellan peels and (b) C. avellana peels and PMMA.
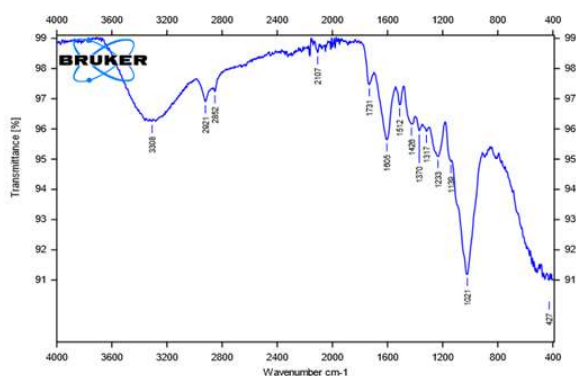
Figure 7. The FT-IR spectrum of the raw material before carbonization.
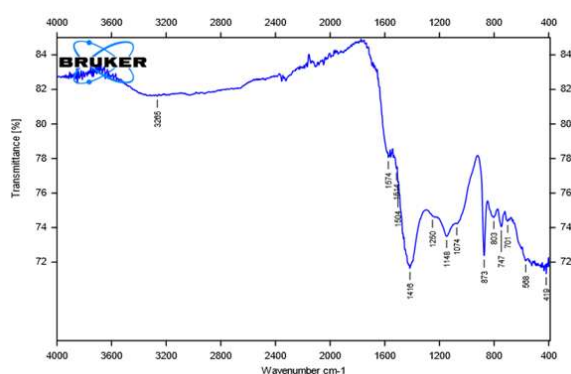
Figure 8. The FT-IR spectrum of the material after carbonization and activation.

CONCLUSION

As a result of the present research, *C. avellan* peels and polymer waste are excellent raw materials for preparing activated carbon. The activated carbon yield when using polymer waste increased by 25% compared to the use of *C. avellana* peels due to an increase in carbon mass. All the prepared activated carbon samples showed high adsorption capacity for MB dye, high iodine value, and high yield, while the density, humidity, and ash values were within the permissible limits, thus exceeding the specifications of commercial activated carbon. *C. avellana* peels charcoal is a promising raw material for producing activated carbon for various industrial purposes.

Future research recommendations include preparing activated carbon from hazelnut peels using different carbonization and activation agents and selecting other adsorbent materials that are available and inexpensive, by utilizing agricultural residues that pollute the environment.

REFERENCES

[1] R.C. Bansal, M. Goyal, CRC Press, 1st Edition, Boca Raton, Florida, USA (2005), p. 67-78. https://doi.org/10.1201/9781420028812.

[2] T. Thangadurai, C.T. Tye, Period. Polytech., Chem. Eng. 65 (2021) 350-360. https://doi.org/10.3311/PPch.16885.

[3] N.M. Haimour, S. Emeish, Waste Manage. 26 (2006) 651-660. https://doi.org/10.1016/j.wasman.2005.08.004.

[4] J.H. Bartha-Vari, L.C. Bencze, E. Bell, L. Poppe, G. Katona, F. Irimie, C. Paizs, M.I. Tosa, Period Polytech., Chem. Eng. 61 (2017) 59-66. https://pp.bme.hu/ch/article/download/10417/7262/24853.

[5] O. Ioannidou, A. Zabaniotou, Renew. Sustain. Energy Rev. 11 (2007) 1966-2005. https://doi.org/10.1016/j.rser.2006.03.013.

[6] C. Mereno-Castilla, F. Carrasco-Marin, M.V. Lopez-Ramon, M.A. Alvarez-Merino, Carbon 39 (2001) 1415-1420. https://doi.org/10.1016/S0008-6223(00)00268-2.

[7] N. Spahis, A. Addoun, H. Mahmoudi, N. Ghaffour, Desalination 222 (2008) 519-527. https://doi.org/10.1016/j.desal.2007.02.065.

[8] G. Duman, Y. Onal, C. Okutucu, S. Onenc, J. Yanick, ACS Public. (2009) 2197-2204. https://doi.org/10.1021/ef800510m.

[9] A. Kumar, H.M. Jena, Res. Phys. 6 (2016) 651-658. https://doi.org/10.1016/j.rinp.2016.09.012.

[10] N.A. Jamion, I.N. Hashim, J. Fund. Appl. Sci. 9 (2017) 102-114. https://doi.org/10.4314/jfas.v9i6s.9.

[11] R.S. Ramalingam, C.R.A.J. Chelliah, S. Baskaran, A.S. Dorairaj, R. Issacl, R. Swaminathan, Amer. J. Chem. Mater. Sci. 6 (2018) 1-6. https://www.researchgate.net/publication/326673130.

[12] V. Viena, Elvitriana, M. Nizar, J. Phys: Conf. Ser. 1232 (2019) 012005. https://doi.org/10.1088/1742-6596/1232/1/012005.

[13] E.M. Mistar, T. Alfatah, M.D. Supardan, J. Mater. Res. Technol. 9 (2020) 6278-6286. https://doi.org/10.1016/j.jmrt.2020.03.041.

[14] A.M.R. Abudaia, Master's Thesis, University of Karabuk (2021).

http://acikerisim.karabuk.edu.tr:8080/xmlui/handle/123456789/1479.

[15] D. Ramutshatsha-Makhwedzha, A. Mavhungu, M.L. Moropeng, R. Mbaya, Heliyon (2022) 09930. https://doi.org/10.1016/j.heliyon.2022.e09930.

[16] M.N. Islam, A. Khatton, J. Sharker, H.A. Sikder, A.M.S. Chowhury, Saudi J. Eng. Technol. 7 (2022) 112-117. https://doi./10.36348/sjet.2022.v07i02.008.

[17] M.B. Gomaa, M.A. Shetawy, R.R. El Bassoumy, M.M. Geasa, Al-Azhar J. Agric. Eng. 2 (2022) 10-16. https://doi.org./10.21608/azeng.2022.240417.

[18] B. Sarici, S. Karatas, E. Altintig, Desalin. Water Treat. 254 (2022) 287-301. https://doi.org/10.5004/dwt.2022.28353.

[19] E. Altintig, B. Sarici, S. Karatas, Envir. Sci. Pollu. Res. 30 (2023) 13671-13687. https://doi.org/10.1007/s11356-022-23004-w.

[20] M.A. Abo Hay Allah, H.A. Alshamsi, Res. Square (2023) 1-12. https://doi.org/10.21203/rs.3.rs-2508076/v1.

[21] M. Olam, Bitlis Eren University Journal of Science 12 (2023) 207-214. https://doi.org/10.17798/bitlisfen.1223614.

[22] M. Olam, Mater. Sci. 30 (2024) 560-567.

[23] M. Olam, Separ. Sci. Technol. 59 (2024) 737-747. https://doi.org/10.1080/01496395.2024.2349177

[24] S.I. Khaleel, A.A.H. AL-Khazraji, E.A.S. AL-Hyali, Journal of the Turkish Chemical Society, Section A: Chemistry 11 (2024) 1407-1416. https://doi.org/10.18596/jotcsa.1416075.

[25] P.K. Jha, V.K. Jha, Mong. J. Chem. 21 (2020) 1249. https://doi.org/10.5564/mjc.v21i47.1249.

[26] R.H. Gumus, I. Okpeku, Adv. Chem. Eng. Sci. 5 (2015) 51-61. https://doi.org./10.4236/aces.2015.51006.

[27] A. Zulkania, F. Ghina Hanum, A.S. Rezki, MATEC Web Conf. 154 (2018) 01029. https://doi.org/10.1051/matecconf/201815401029.

[28] P.D. Pillai, JETIR 5 (2018) 470-472. https://www.jetir.org/papers/JETIR1810274.pdf.

[29] ASTMD2854-70 Standard Test Method for Apparent Density of Activated Carbon.

[30] D. Adinata, W.M.A. Daud, M.K. Aroua, Bioresour. Technol. 98 (2007) 145-149. https://doi.org/10.1088/1742-6596/1349/1/012103.

[31] F.F. Saleem, Ph.D. Thesis, University of Mosul, (2010).

SEMAA IBRAHEEM
KHALEEL

Department of Petroleum
and Refining Engineering, College
of Petroleum and Mining
Engineering, University of Mosul,
Mosul, Iraq

SINTEZA I KARAKTERIZACIJA AKTIVNOG UGLJA DOBIJENOG OD LJUSKI LEŠNIKA HEMIJSKOM AKTIVACIJOM

Aktivni ugalj je u ovom istraživanju pripremljen od ljuski lešnika (Corilus avellana) sa nekim aditivima, kao što je polimerni otpad (polimetil metakrilat, PMMA). Samlevenoj sirovini su dodavane određene količine natrijum-hidroksida, tako da je odnos ljuska:NaOH bio u opsegu od 1:0,5 do 1:2,5. Ljuske su, takođe, tretirane polimernim otpadnim materijalima (5-25%) pri osnovnom odnosu ljuska:NaOH 1:2 na 550 °C. Zatim su procenjena svojstva pripremljenih uzoraka u pogledu adsorpcije metilenske boje, jodnog broja, gustine, vlažnosti i prinosa i upoređeni sa britanskim i ruskim komercijalnim modelima. Za karakterizaciju pripremljenih aktiviranih uzoraka korišćene su SEM i FT-IR tehnike. Rezultati su pokazali da se uzorci aktivnog uglja pripremljeni od ljuske lešnika karakterišu visokim jodnim brojem (894.521 mg/g), kapacitetom adsorpcije metilenskog plavog (98,425 mg/g) i prinosom (14.973%). Što se tiče uzoraka pripremljenih od ljuske lešnika sa PMMA, primećeno je povećanje vrednosti jodnog broja (1015.021 mg/g), kapaciteta adsorpcije metilenskog plavog (148 mg/g) i prinosa. Ovo ukazuje da je proces dodavanja bio pozitivan korak u poboljšanju svojstava i prinos aktivnog uglja. Što se tiče gustine, pepela i vlažnosti, ova svojstva su bila u granicama dozvoljenih za sve pripremljene uzorke aktivnog uglja i umnogome premašila svojstva komercijalnih uzoraka ugljenika.

Ključne reči: karbonacija, polimerni otpad, polimetil-metakrilat, metilensko plavo, fizička svojstva.

NAUČNI RAD

PINAR ŞENGÜN

ÇETİN KADAKAL

Food Engineering Department, Faculty of Engineering, University of Pamukkale, Turkey.

EFFECT OF HOT AIR AND HOT AIR-ASSISTED MICROWAVE DRYING ON DRYING KINETICS AND QUALITY OF RED AND WHITE PITAYA SLICES

Highlights

- D_{eff} value increased in both fruit types due to the increase in temperature and microwave power.
- The HAD method fitted to the parabolic model, HA-MWD to the page model.
- The increase in RR decreased SR in both fruits.
- The highest number of pores in the SEM monitoring of pitaya slices was observed in HA-MWD.
- The HA-MWD method is more advantageous in terms of energy consumption compared to the HAD.

Abstract

In this study, mathematical modeling, drying kinetics, rehydration ratio (RR), shrinkage ratio (SR), color change (ΔE), total phenolic content (TPC), antioxidant activity (AA), and microstructural examination of red and white pitaya fruits dried by hot air drying (HAD) and hot air assisted microwave drying (HA-MWD) methods were conducted. In the HAD and HA-MWD methods, the effective diffusion coefficient (D$_{eff}$) increased as the drying time shortened. While the Page model provides the best fit to HA-MWD curves, HAD curves are also appropriately defined by the Parabolic Model. The RR value was found to be higher in the HA-MWD method. TPC values of fresh red and white pitaya fruits were calculated as 389.7±0.8 and 310.1±0.4 mg GAE/100 g dry matter (DM), respectively. The highest TPC value in HAD was determined as 251.4±0.4 mg GAE/100 g DM at 70 °C. In the HA-MWD method, TPC and AA decreased due to an increase in microwave power. SEM monitoring showed that crack and pore sizes increased with the temperature increase in HAD for both fruit types. The increase in microwave power caused more damage to the structure in the HA-MWD method.

Keywords: Pitaya, drying, effective diffusion, mathematical modeling, microstructure.

INTRODUCTION

Pitaya or dragon fruit (*Hylocereus* spp.) is considered the fruit of species in the cactus family and is widely grown in tropical or subtropical regions around the world [1]. Pitaya is generally classified as white flesh/red shell, red flesh/red shell, and white flesh/yellow shell pitaya according to its flesh and shell appearance [2]. However, there are three main varieties grown commercially [3].

Dragon fruit generally has a taste resembling a mixture of pear and kiwi. The white-fleshed dragon fruit tastes like a cross between an unripe kiwi and a pear. The red-fleshed dragon fruit tastes like a mixture of pear, kiwi, and melon. The taste of the yellow-skinned, white-fleshed dragon fruit is more aromatic and sweeter than the other two species [4]. Pitaya fruit generally consists of 36-37% shell part, 47-49% flesh part (pulp), and 14% seeds [5].

Pitaya fruit, especially its pulp layer, contains vitamins, minerals, and nutritional components (group B vitamins, vitamins E and C, sodium, potassium, calcium, phosphorus, iron, fat, protein, carbohydrate, flavonoid, crude fiber, betacyanins, phenolics, essential fatty acids, carotenoids, and polyphenols) that are quite high. It exhibits relatively high antioxidant activity compared to other subtropical fruits [6].

Pitaya fruit has a short shelf life due to its rapid ripening, which limits storage time during transportation and marketing. Different preservation methods can be used to extend the shelf life of fresh pitaya fruit. Drying, an

alternative process to food preservation, aims to reduce water activity, provide microbiological stability, extend shelf life, and prevent undesirable physical and chemical changes [7]. When drying foods, the method that will cause the least change in the structure should be preferred. HAD, one of these methods, is the most widely used method in the industry for the preservation and processing of fruits and vegetables. In the HAD method, food can be exposed to high temperatures for a long time to reach the final moisture content. For this reason, undesirable changes occur in the chemical, physical, and sensory properties of the food [8]. In recent research, the microwave-assisted hot air drying method has been developed to prevent these negative situations in the product and to obtain the desired higher quality products [9].

Quantitative understanding of the drying process is of great practical and economic importance in many areas such as process design, quality control, and energy saving. This understanding can be used in the industry to develop more effective and efficient drying processes. Especially in the drying of foods, correct management of the drying process ensures the preservation of product quality, prevention of microbial spoilage, and extension of the shelf life of the products. Additionally, optimizing energy consumption contributes to reducing environmental impacts by reducing operating costs [10]. Kinetic models are used to design a process that can carry out the drying process safely and keep the quality at the highest level. These models help ensure optimum conditions at every stage of the process by accurately predicting drying time, temperature profile, and moisture content. Quantitative analysis and kinetic modeling of the drying process significantly enhance process efficiency in industrial applications while also playing a crucial role in achieving energy savings and sustainability goals. The advantage of thin-layer drying models, in which foods are dried in a thin layer, is that the equations in this model require little data and are easy to use [11]. Thin-layer drying equations are equations that include the change of dimensionless moisture content against time [12].

There are a limited number of studies in the literature comparing HA-MWD with HAD in terms of drying properties, mathematical modeling, rehydration, and shrinkage properties of pitaya slices. In addition, the number of studies reporting the change in total phenolic substance and antioxidant activity content as a result of drying is very few. In this context, this study aims to determine the drying, rehydration, and shrinkage properties of pitaya slices dried by HA-MWD and HAD methods as well as to compare their microstructural investigations.

MATERIALS AND METHODS

Material

Red pitaya (RP) and white pitaya (WP) (*Hylocereus polyrhizus* and *Hylocereus undatus*) fruits were obtained from the Erdemli district in Mersin, Turkey. Erdemli is located at 10 m above sea level with coordinates 36° 36' 17" north latitude and 34° 18' 30" east longitude. Pitaya fruits were sliced in 0.5 ± 0.1 cm thickness after peeling.

Drying Procedure

Hot air drying (HAD)

RP and WP fruits were sliced to a thickness of 0.5 ± 0.1 cm and weighed 250 g, placed on metal drying trays. Pitaya fruits were dried in a hot air drying oven to 14% moisture content (Arçelik, KMF 833 W, Turkey). The drying procedure was carried out at an air velocity of 1 m·s^{-1} at temperatures of 50, 60, and 70 °C. All drying processes were carried out in triplicate.

Hot air-assisted microwave drying (HA-MWD)

In the HA-MWD method, three temperatures (50, 60, and 70 °C) and two different microwave powers (100 W and 200 W) were determined. The drying process was carried out in six different parameters: 50 °C + 100 W, 50 °C + 200 W, 60 °C + 100 W, 60 °C + 200 W, 70 °C + 100 W and 70 °C + 200 W. RP and WP fruits, sliced to a thickness of 0.5±0.1 cm, were placed in a polypropylene drying tray at 250 g each and dried in a hot air assisted microwave (Arçelik, KMF 833 W, Turkey).

Drying Characteristics

Moisture content (M$_t$)

Eq. (1) was used to calculate the moisture content of RP and WP fruits during the drying process.

$$M_t = \frac{m - DM}{DM} \qquad (1)$$

where M_t is the moisture content at any time, m is the weight of the sample (g), and DM is the amount of dry matter (g).

Moisture ratio (MR)

Eq. (2) was used to calculate the MR [13]. The M_t obtained by Eq. (1), was used to calculate the MR.

$$MR = \frac{M_t - M_e}{M_i - M_e} \qquad (2)$$

At any time t, M_t and M_i (initial moisture content) are very small compared to M_e (equilibrium moisture) content. Therefore, M_i is ignored. The M_t is expressed in Eq. (1).

Effective moisture diffusivity (D$_{eff}$)

Fick's diffusion equation, Eq. (3), is used to describe the drying process of agricultural products in the decreasing period of drying rate [14]:

$$\frac{\partial M}{\partial t} = D_{eff} \nabla^2 M \qquad (3)$$

This equation is simplified by Crank [14] for sliced products assuming that the moisture transfer occurs only by diffusion with a constant diffusion coefficient, with no shrinkage in the product, for a long drying time at a constant temperature. This model is valid for slab-shaped materials and assumes that moisture diffusion occurs over a flat surface:

$$MR = \frac{8}{\pi^2} \sum_{n=1}^{\infty} \frac{1}{(2n+1)^2} \exp\left(-(2n+1)\pi^2 \frac{D_{eff} t}{4L^2}\right) \qquad (4)$$

D_{eff} was calculated by Eq. (4). In this formula, L is half the slice thickness of the sample before drying, and t is the drying time. For the long drying time, Eq. (4) is simplified in a straight line. Here, the value of n is accepted to be 1, and Eq. (5) is written as follows [15]:

$$\ln(MR) = \ln\left(\frac{8}{\pi^2}\right) - \left(\frac{\pi^2}{4L^2} \, D_{eff} t\right) \qquad (5)$$

The natural logarithm of the moisture content values is taken, and the graph of the drying time gives a linear curve; and the D_{eff} (Eq. 6) is calculated from the slope of this line [15]:

$$Slope = -\frac{\pi^2}{4L^2} \, D_{eff} \qquad (6)$$

Mathematical modeling of drying curves

Correlation between the estimated and experimental data of pitaya slices dried with different drying methods, is explained by the coefficient of determination (R^2), chi-square (χ^2), Root Mean Square Error (RMSE), Akaike Information Criteria (AIC) values. RMSE is a parameter that measures the deviation between the predicted and experimental data and determines the accuracy of the model. The RMSE value is calculated by taking the square root of the average of the squares of the differences between the values predicted by the model and the real values. A lower RMSE value indicates that the model performs better and its predictions are closer to the actual data. AIC is used to select the model that best fits the data set by establishing a balance between the accuracy and complexity of the model. To determine the model that best estimates the experimental data, the model with the lowest χ^2, RMSE and AIC values and the highest R^2 value should be selected. RMSE (Eq. 7), chi-square (χ^2) (Eq. 8) and R^2 values (Eq. 9) and AIC (Eq. 10) were calculated as follows [13]. The thin-layer drying models used in this study are given in Table 1. Calculations were made with the help of the MATLAB (R2022a, version 9.12) program using the trust-region algorithm and the non-linear curve fitting toolbox.

$$RMSE = \left[\frac{1}{N}\sum_{i=0}^{N}(MR_{pre,i} - MR_{exp,i})^2\right]^{\frac{1}{2}} \qquad (7)$$

$$\chi^2 = \frac{\sum_{i=0}^{N}(MR_{pre,i} - MR_{exp,i})^2}{N-n} \qquad (8)$$

$$R^2 = \frac{\sum(MR_{pre} - MR_{exp})^2}{\sum(MR_{pre,av} - MR_{exp})^2} \qquad (9)$$

$$AIC = -2\ln(L) + 2p \qquad (10)$$

where L is maximum likelihood value of the model, p is number of parameters in the model.

Determination of RR and SR

Rehydration analysis was performed according to the procedure recommended by Tepe and Tepe [13]. For this purpose, RP and WP fruits weighing 5 g were placed in a glass container. 400 ml of distilled water was placed on them and taken into a water bath at 40 °C. Temperature control was performed at regular intervals throughout the analysis. Rehydration analysis was completed after 24 hours, and pitaya slices were weighed. The rehydration rate was calculated by Eq. (11):

$$RR\% = \frac{W_r}{W_0} \qquad (11)$$

where W_r is weight after rehydration (g), W_0 is the weight before rehydration (g).

SR values of dried red and white pitaya slices were expressed with bulk shrinkage. Liquid displacement technique was used to determine the bulk shrinkage [13]. In this method, hexane was used to measure the volume change. SR was calculated with the help of Eq (12).

Table 1. Some mathematical models used in modeling the drying process [16].

Model name	Model
Page	$MR = \exp(-kt^n)$
Henderson and Pabis	$MR = a\exp(-kt)$
Wang and Singh	$MR = 1 + at + bt^2$
Parabolic	$MR = a + bt + ct^2$
Logarithmic	$MR = a\exp(-kt) + c$
Lewis	$MR = \exp(-kt)$

$$SR\% = 100 - \frac{v_i - v_f}{v_i} \cdot 100 \qquad (12)$$

where v_i: is the volume of fresh pitaya slice (cm^3), v_f: is the volume of dried pitaya slice (cm^3).

Determination of color

Hunter Lab Color Miniscan XE (Model No: 45/0-L, USA) was used for the color analysis of fresh and dried RP and WP fruits. First, pitaya slices were placed on a white surface and a transparent glass was placed over them. Then, color values were measured with the device away from light. Eq. (13) was used to calculate the total color change (ΔE):

$$\Delta E = \sqrt{\left(L_0^* - L^*\right)^2 + \left(a_0^* - a^*\right)^2 + \left(b_0^* - b^*\right)^2} \qquad (13)$$

where L_0^* and L^* are lightness values before and after drying drying (0 = black, 100 = white).
where a_0^* and a^* are redness values before and after drying (a+ =red, a- =green).
where b_0^* and b^* are yellowness values before and after drying drying (b+ =yellow, b- =blue).

Determination of TPC

Analysis of TPC was performed following the procedure recommended by Singleton and Rossi [17]. Methanol-water mixture was used as solvent in TPC extraction due to the polar structure of phenolic compounds. For this purpose, 1 g of pitaya fruit was taken and 25 mL of methanol-water solution (90:10) was added. Then, the samples became homogeneous with a

homogenizer. Homogeneous samples were centrifuged at 9000 rpm at 4 °C. Centrifuged samples were filtered with a coarse filter. Next, 300 µL of the resulting filtrate was taken and mixed with 1500 µL of a solution (1:10 ratio of Folin-Ciocalteu reagent to ultrapure water) and kept in the dark for 5 minutes. Subsequently, 1200 µL of 7.5% $NaHCO_3$ solution was added and left at room temperature for 2 hours. After the incubation period, the absorbance values of the solutions were measured at 760 nm using a spectrophotometer (PG Instruments T80 UV/VIS, England). To calculate the results, the absorbance of gallic acid standard solutions prepared at concentrations of 25, 50, 62.5 and 100 ppm was measured. Measurement results were given in gallic acid equivalent (GAE 100 g^{-1} DM).

Determination of AA

Determination of AA was performed according to the DPPH (2,2-diphenyl-1-picrylhydrazyl) method [18]. For sample extraction, 25 mL of methanol: water (90:10) mixture was added to 1 g of pitaya fruits and homogenized in a homogenizer. It was centrifuged for phase separation. Centrifuged samples were filtered through filter paper to separate the clear phase. Next, 150 µL of the filtered samples was taken and 2850 µL DPPH was added. The mixture was incubated for 1 hour in a dark environment. After 1 hour, the absorbance of the samples was measured at 515 nm using a spectrophotometer. A trolox standard prepared at different concentrations was used to determine the values corresponding to the absorbances. Measurement results were given in mmol trolox equivalent (TE 100 g^{-1} DM).

Microstructural analysis (SEM)

The slice structure of pitaya fruits dried using different drying methods was observed using a scanning electron microscope (Zeiss-Supra 40VP 35 FESEM, Germany). Dried pitaya slices were coated with gold to provide a reflective surface for the electron beam during SEM monitoring. Photographs of the samples were taken at 15 kV voltage and 250x magnification [19].

Statistical analysis

Statistical analysis was performed using SPSS software (ver. 26, SPSS Inc., Chicago, IL, USA). One-way ANOVA and Tukey tests were applied to compare the mean values. Mean values were compared at a significance level of $p < 0.05$.

RESULTS AND DISCUSSION

Drying of pitaya fruit

MR graphics of drying of RP and WP fruits by HAD and HA-MWD methods are shown in Fig. 1, and images of dried pitaya slices are shown in Fig. S1. Drying times and Deff (m2 s-1) values are given in Table 2. When comparing the drying times of RP and WP fruits dried using HAD at 50 °C, 60 °C, and 70 °C, WP fruit dried faster. The reason for this is thought to be due to the high number of seeds in the WP fruit. Çetin et al. [20] reported that white dragon fruit dried in a shorter time than red dragon fruit. In the HA-MWD

method, the drying time was considerably shorter than the HAD method. RP fruit dried in 840 minutes at 50 °C, while at 50 °C + 100 W and 50 °C + 200 W, drying times were 315 and 60 minutes, respectively. For both fruit types, drying time was shortened due to the increase in drying temperature and microwave power. Raj and Dash [8] reported that white-fleshed pitaya fruit dried in 510 minutes at 60 °C. Nordin et al. [21] reported that red pitaya dried in 27 hours in hot air drying at 55 °C and in 6 hours in hot air assisted microwave drying. Deff increased due to temperature increase in both fruits in HAD. Deff values of white pitaya fruit were higher. In HA-MWD, as microwave power increased, Deff increased. The highest Deff was observed for WP at 70 °C + 200 W. Ayala Aponte et al. [22] reported an increase in Deff as drying time decreased. As the permeability of the cell wall increases at high temperatures, the diffusion of water molecules increases, resulting in an increase in Deff [23]. In one study, white pitaya fruits sliced 3 and 5 mm thick were dried at 60, 70 and 80 °C.As a result of the study, the highest Deff was measured in fruits dried at 80 °C with a slice thickness of 5 mm with 9.21x10^{-10} (m^2 s^{-1}) [24].

Mathematical modeling of pitaya fruits

Statistical parameters (χ^2, RMSE, AIC, R^2) of the thin layer modeling used in this study are given in Tables S3-S6 (Supplementary material). As a result of drying RP fruits with HAD, the drying curves were explained with the parabolic model, which had the highest R^2 and lowest χ^2, RMSE, and AIC. The AIC value was considered as an additional parameter to select the best model. The experimental values and those predicted by the model showed a strong correspondence, as confirmed by the AIC. Recently, AIC has been used to more accurately select the best mathematical model representing the drying curves in different agricultural products [25].

Similar results were observed for WP fruit dried using HAD. The model that best explains the drying curves was chosen as a parabolic model. The parabolic model assumes that the rate of water loss is high at the beginning of the drying process and decreases as time progresses. This modeling can be used to predict the change in moisture content of food over the drying period. Drying curves of HA-MWD as a result of drying at different temperatures and microwave powers were described by the page model. The result was the same for RP and WP fruits. The highest R^2 and lowest χ², RMSE, and AIC values were detected in the page model. Whereas the Page model is based on the understanding that the rate of water loss decreases with time and is dependent on humidity, the parabolic model assumes that the rate of water loss decreases with time and is independent of moisture [13]. Ayala-Aponte et al. [22] applied Newton, Handerson-Pabis, Peleg, and Weibull mathematical models to the data obtained from pitaya fruits dried at 50, 60, and 70 °C. The study found that the Peleg model (R^2 = 0.990) and Weibull model (R^2 = 0.996) best fit the experimental data. Drying of white pitaya fruit at 200, 400, and 600 W and 60 °C was reported to fit the Weibull kinetic model [8]. In a study of Hylocereus undatus shells drying at 50, 60, and 70 °C, it

was determined that the drying kinetics fit the page model [26]. The drying kinetics of white pitaya fruits dried with a heat pump at different slice thicknesses and temperatures were best described by the Avhad and Marchetti model [27]. Newton, Page, Lewis, Henderson, logarithmic, and Midilli models were applied to the data obtained from drying king oyster mushrooms with four different methods. As a result of the study, it was seen that Midilli and Page models were more suitable for simulating the drying process [28]. In a different study, it was reported that the lotus root dried with different methods was fit to the modified page model (R2> 0.99) [29]. The reason for the difference in kinetic models may be due to the difference in fruit type, structure of the food matrix, moisture content of the product and drying conditions.

Table 2. Drying time, effective moisture diffusivity, and rehydration ratio of dried pitaya fruits.

Drying Method	Drying time (min)		D_{eff}(m^{2}s^{-1})		RR % (40 °C)		SR %	
	RP	WP	RP	WP	RP	WP	RP	WP
50 °C	1480	840	1.18x10^{-10}	2.03x10^{-10}	2.71±0.014[e]	2.48±0.014[e]	85.21±0.18[a]	84.98±0.32[a]
60 °C	750	570	2.36x10^{-10}	3.04x10^{-10}	2.97±0.028[c]	2.70±0.024[b]	83.87±0.17[b]	81.78±0.24[c]
70 °C	540	315	3.38x10^{-10}	5.75x10^{-10}	3.20±0.007[b]	2.73±0.012[ab]	82.34±0.32[c]	80,34±0.14[d]
50 °C + 100W	435	315	3.72 x10^{-10}	5.41 x10^{-10}	3.20±0.014[b]	2.57±0.010[cd]	81.79±0.14[c]	83,61±0.24
50 °C + 200W	75	60	2.43 x10^{-9}	2.87 x10^{-9}	2.65±0.022[e]	2.50±0.010[de]	86.13±0.39[a]	84,48±0.31[ab]
60 °C + 100W	415	270	4.23 x10^{-10}	6.42 x10^{-10}	3.13±0.035[b]	2.65±0.034[bc]	81.11±0.41[c]	82.12±0.16[c]
60 °C + 200W	70	50	2.52 x10^{-9}	3.28 x10^{-9}	2.86±0.020[d]	2.56±0.036[de]	82.01±0.15[c]	83.55±0.18[b]
70 °C + 100W	345	195	4.90 x10^{-10}	8.79 x10^{-10}	3.35±0.010[a]	2.80±0.022[a]	80.09±0.18[d]	79.13±0.21[e]
70 °C + 200W	67	47	2.60 x10^{-9}	3.60 x10^{-9}	2.89±0.016[d]	2.71±0.018[b]	81.92±0.14[c]	81.44±0.34[c]
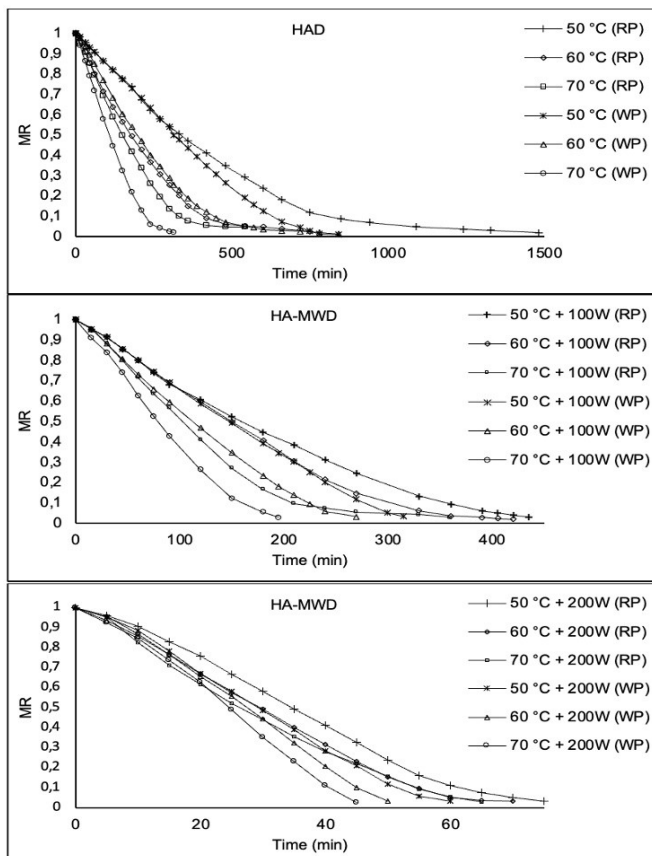
Figure 1. MR changes of red and white pitaya fruits dried in HAD and MA-MWD

RR and SR of dried pitaya fruits

The rehydration rate of a dried food is often used as an index of quality. It shows the physical injuries and chemical changes caused by the removal of water from the cellular structure during the drying process [30]. RR and SR of dried RP and WP fruits are shown in Table 1. In the HAD method, RR increased in both fruit types due to the increase in temperature. The increase of RR decreased the shrinkage of pitaya slices. Doymaz [31] explains the low RR at low temperature due to lower diffusion of water across the surface and cellular structure damage during the rehydration process. The RR of dried RP fruit was higher than that of WP fruit (p<0.05). This is because the flesh of the RP fruit was more than the WP fruit. Therefore, it attached more water to its structure. Accordingly, shrinkage was observed less in RP fruits. At the same drying temperature, increasing microwave power decreased RR. The highest RR was determined as 3.35±0.010 and 2.80±0.022 in RP and WP fruits at 70 °C + 100W drying, respectively (p<0.05). The lowest SR was detected in the 70 °C + 100W drying method (p<0.05). Since the pore structure of the products dried in microwave drying is greater, it allows more water to be absorbed, so the rehydration rate is higher [32]. In a study by Raj and Dash [8], hot air and intermittent microwave methods were used to dry pitaya fruits. As a result of the study, it was found that the lowest RR was 1.667 in hot air drying, and the highest rehydration rate was found in the intermittent microwave drying method at 600 W. In a study in which pitaya fruits were dried by hot air and freeze-dried, the RR of freeze-dried fruit chips was found to be higher. They reported that the reason for this was the homogeneous cell structure that served as capillary pathways [33]. Similarly, it has been reported that the RR of apple slices dried in microwave is higher than that of apple slices dried in hot air [34].

Color of dried pitaya fruits

L^*, a^* and b^* values of fresh and dried RP and WP slices are shown in Table 3. L^* value increases in both fruit

types depending on the temperature increase in HAD. The L^* value is an important quality parameter that expresses the lightness and darkness of the color. In RP fruit, an increase in a^* value, which expresses the redness of the color, was observed due to the increase in temperature in HAD. The highest a^* value was at 70 °C (p<0.05). It was observed that the color values were less preserved in the long-term drying method at low temperature. Therefore, the highest ΔE values was calculated for both fruit types at 50 °C in HAD (p<0.05). For RP fruit, L^* and a value decreased due to the increase in power at the same drying temperature in HA-MWD. The highest ΔE changes occurred during drying at 50 °C + 200W (p<0.05). Results were similar for WP fruit. The increase in microwave power resulted in increased ΔE values. Asthiani *et al.* [35] reported that the ΔE values of peach slices dried by hot air and hybrid hot air-microwave method increased due to the increase in microwave power. Raj and Dash [17] reported that the color change of *Hylocereus undatus* fruit dried by intermittent microwave drying was in the range of 18.643-24.847. It was reported that the L^*, a^* and b^* values of white dragon fruit dried by hot airdrying method at 60 °C were 16.28 ± 1.25, 7.91±00 and 6.08 ± 0.97, respectively [36]. Horuz and Maskan [30] reported that the color change caused by the microwave drying method was greater than the hot air drying method. This indicates that the color is better preserved at low microwave power in HA-MWD in both fruit types. The color of dried fruit is affected by the degradation of some pigments, non-enzymatic browning, and oxidation of phenolic compounds, which contribute to changes in color hue and intensity.

TPC of dried pitaya fruits

TPC values of fresh and dried pitaya fruits were shown in Table 4. TPC value of RP fruit was higher than WP fruit. TPC values of fresh RP and WP fruits were calculated as 389.71±0.80 and 310.11±0.42 mg GAE 100 g^{-1} DM, respectively (p<0.05). Angonese *et al.* [37] found the TPC value of fresh white and red dragon fruit to be 75.6 ± 14.4 and 107.4 ± 10.8 mg GAE/100g DM, respectively. In both fruit types, there was an increase in TPC values due to the increase in temperature during HAD (p<0.05). It is reported that this is due to the shortening of the drying time. Most phenolic compounds are highly sensitive to heat and easily oxidized. The decrease in total phenolic substance content with drying is explained by irreversible oxidation and thermal degradation of phenolic components due to long-term temperature exposure. The highest TPC value in HAD was determined as 251.35±0.35 mg GAE 100 g^{-1} DM at 70 °C (p<0.05). A decrease in the TPC was observed in RP fruits dried by the HA-MWD method, depending on the increase in microwave power at the same temperature. The highest TPC value was calculated as 250.95±0.71 mg GAE 100 g^{-1} DM at 70 °C + 100W (p<0.05). Raj and Dash [8] reported that microwave power decreased the TPC of pitaya fruit. Şahin *et al.* [38] explained that the decrease in TPC with higher power levels in microwave drying may be due to the temperature increase due to internal heating and the degradation of polyphenols.

AA of dried pitaya fruits

AA values of fresh RP and WP fruits were found to be 82.89±0.33 and 54.21±0.74, respectively (p<0.05). The AA value of RP fruit was higher than that of WP fruit (Table 4). Al-Mekhlafi *et al.* [39], in a study on seven different pitaya samples, found that the antioxidant activities of red-fleshed fruits were higher than white-fleshed fruits. In a study, the antioxidant activities of fresh white and red pitaya fruits were found to be 17.56 and 22.65 µg GA/g, respectively. It was stated that the antioxidant properties of red dragon fruit are twice the amount due to betacyanin pigment compared to white pitaya fruit [7]. In HAD carried out at 50, 60 and 70 °C, it was observed that AA increased as the drying temperature increased. Liatrakoon *et al.* [40] reported that when they applied heat treatment to white-fleshed and red-fleshed dragon fruit purees between 50 and 90 °C for 0-60 minutes, the antioxidant activity of both fruit types increased due to the increase in temperature. A shorter drying time increased the AA value. In HA-MWD, AA decreased as microwave power increased at the same temperature (p<0.05). Increasing microwave power increased the internal temperature of the product; therefore, more loss was observed. In HA-MWD, the highest AA was observed at 60 °C + 100W in both fruit types (p<0.05). AA values were better preserved in RP fruit than in WP fruit. Similarly, Lee *et al.* [41] found that the AA value of red dragon fruit dried by spray drying was higher than that of white fruits.

Microstructural analysis of dried pitaya fruits

SEM monitoring of RP and WP fruits dried by HAD and HA-MWD methods is shown in Fig. S2. When the SEM monitoring of RP fruits dried by HA drying method was examined, the formation of pores and cracks increased due to the increase in temperature. In SEM monitoring of WP fruits dried at 50, 60, and 70 °C, crack and pore sizes increased due to the temperature increase. These structural changes increased the porosity of the fruit slices and contributed to the increase in RR. The highest RR in the HAD method was determined at 70 °C in both fruit types. This increase in RR prevents excessive collapse of cellular structures and reduces the SR value. The drying process applied at high temperatures causes the water to evaporate quickly. This may cause various deformations and breaks on the fruit surface in SEM monitoring. Cracks and pores formed during drying increase the permeability of the fruit tissue and directly affect the movement and distribution of moisture. Bassey *et al.* [7] report that drying the pitaya fruit at high temperatures will cause the formation of microchannels and pores that will help remove moisture. When microstructural analysis of RP fruits dried by HA-MWD were examined; At the same temperature, more porous growth and crack formation were observed due to the increase in microwave power. It is thought that the reason for the formation of the porous structure is due to the high volumetric heating. Determination in the pore structure was observed more due to the increase in temperature and microwave power due to drying of RP fruit with the HA-MWD method. The largest pore structures and cracks occurred in the 70 °C + 200W drying method.

Table 3. Color of dried pitaya fruits.

Drying Method	RP				WP			
	L*	a*	b*	ΔE	L*	a*	b*	ΔE
Fresh	19.72±0.89[de]	38.19±0.63[a]	-8.10±0.78[d]	0.00	58.96±0.25[a]	-0.79±0.02[be]	4.12±0.66[cd]	0.00
50 °C	18.90±0.51[e]	8.96±0.73[de]	-1.29±0.23[bc]	30.02±0.18[a]	31.44±1.56[f]	-0.61±0.06[bd]	5.89±0.12[bc]	27.61±0.12[c]
60 °C	23.74±0.33[ab]	17.80±0.38[b]	-1.84±0.26[c]	20.72±0.24[c]	38.97±0.88[d]	0.28±0.18[a]	4.34±0.68[cd]	19.99±0.21[e]
70 °C	25.53±0.35[a]	20.01±0.87[b]	-1.72±0.35[c]	20.06±0.32[c]	51.17±0.74[b]	-1.17±0.15[de]	7.58±0.24[ab]	8.74±0.14[g]
50 °C + 100W	22.47±0.21[bc]	8.41±0.33[df]	-1.62±0.52[bc]	30.11±0.17[a]	40.23±0.86[d]	-1.43±0.09[e]	5.95±0.21[bc]	18.94±0.18[ef]
50 °C + 200W	16.00±1.07[f]	6.10±0.62[f]	-1.95±0.15[c]	32.88±0.14[a]	20.64±0.78[h]	-0.10 ±0.10[bc]	1.98±0.53[e]	38.39±0.32[a]
60 °C + 100W	21.33±0.15[cd]	12.31±0.22[c]	-1.66±0.15[bc]	26.71±0.20[b]	44.59±1.35[c]	-1.05±0.9[ce]	5.53±0.20[bc]	14.55±0.26[f]
60 °C + 200W	19.72±0.52[de]	6.93±0.52[ef]	-1.67±0.16[bc]	31.91±0.22[a]	24.36±0.85[g]	-0.05±0.10[ab]	2.19±0.28[de]	34.66±0.25[b]
70 °C + 100W	21.21±0.42[ce]	13.05±0.71[c]	0.60±0.41[a]	26.64±0.28[b]	45.72±0.31[c]	-1.39±0.09[e]	9.45±0.18[a]	14.43±0.24[f]
70 °C + 200W	10.47±0.10[g]	10.79±0.61[cd]	-0.24±0.40[ab]	29.96±0.24[a]	35.68±0.73[e]	-0.55±0.06[bc]	2.41±0.19[de]	23.38±0.12[c]

*Different letters in the same column indicate significant differences with a confidence of 95%.

Table 4. Total phenolic matter and antioxidant activity of dried pitaya fruits.

Drying Method	TPC (mg GAE/100 g DM)		AA (mmol TE/100 g DM)	
	RP	WP	RP	WP
Fresh	389.71±0.80[a]	310.11±0.42[a]	82.89±0.33[a]	54.21±0.74[a]
50 °C	197.17±0.73[h]	162.97±0.88[i]	38.075±0.52[g]	34.82±0.45[de]
60 °C	227.62±0.62[e]	174.45±0.40[h]	47.42±0.45[de]	43.11±0.32[bc]
70 °C	251.35±0.35[b]	197,3±0.34[e]	49.35±0.61[d]	46.70±0.98[b]
50 °C + 100W	240.35±1.06[c]	207.12±0.34[d]	52.32±0.72[c]	36.52±0.23[de]
50 °C + 200W	201.6±0.53[g]	192.90±0.72[f]	41.62±0.50[f]	34.82±0.75[de]
60 °C + 100W	211.25±0.99[f]	228.22±0.40[b]	60.22±0.70[b]	39.18±0.28[cd]
60 °C + 200W	205.07±0.57[g]	213.52±1.06[c]	53.22±0.32[c]	29.07±0.66[f]
70 °C + 100W	250.95±0.71[b]	209.85±0.92[d]	54.25±0.42[c]	34.35±0.32[e]
70 °C + 200W	232.35±0.98[d]	187.52±0.28[g]	46.22±0.66[e]	26.57±0.55[f]

*Different letters in the same column indicate significant differences with a confidence of 95%.

The RR value similarly decreased with the increase in microwave power at the same temperature. Increasing temperature and microwave power caused further expansion of the internal structure. The results are similar for WP fruit. At the same temperature, more collapse and shrinkage were observed in the structure with increasing microwave power. Therefore, the lowest SR rates were calculated in the methods using 200 W microwave power. It has been revealed that increasing microwave power disrupts the cellular structure of the samples. It has been reported that this may be due to the high diffusion rate caused by temperature and microwave power [42]. Therefore, the optimum selection of temperature and microwave power in drying processes is critical to maintain the rehydration capacity and shrinkage rate of the product. Raj *et al.* [8] stated that as a result of drying, white-fleshed dragon fruit with the microwave vacuum drying (200 W, 400 W, 600 W) method, the pore diameter increased due to the increase in microwave power. In a study, when the SEM images of tomatoes dried with HAD, MW and HA-MWD methods were examined, it was revealed that the highest deformation occurred in tomatoes dried with MW and HA-MWD methods [43]. When the HAD method is compared with the HA-MWD method, it is seen that structural defects are more common in the HA-MWD method. Microwave energy causes water molecules to move rapidly, accelerating evaporation. However, while the inner surface of the fruit heats up faster, evaporation may occur slower on the outer surface. In this case, it may cause more cracks and pores in the fruit structure. Apart from this, high microwave powers and long-term processing may cause overheating and deterioration of the fruit structure.

CONCLUSIONS

In this study, drying properties, mathematical modelling, rehydration ability, TPC and AA values and tissue damage caused by the drying process were examined as a result of drying RP and WP fruits with HAD and HA-MWD. As a result of the research, the HAD and HA-MWD methods applied were effective in drying pitaya slices. As a result, although the high temperatures applied provided a short drying time, they caused structural defects. The HA-MWD method is a more efficient method in terms of energy consumption since it is completed in a shorter time than HAD. Although the HAD method can be widely used with low energy costs, it is disadvantageous in terms of energy efficiency due to long drying times. The HA-MWD method minimizes nutritional value loss by preserving the bioavailable components of the fruit. The HA-MWD method stands out as a faster and more efficient method. However, some promising drying methods need to be evaluated. Therefore, in future studies, it may be recommended to dry pitaya slices using with different pre-treatments and different drying methods. In this way, the most suitable conditions and methods can be optimized by observing textural properties and nutrient loss.

ACKNOWLEDGMENT

NOMENCLATURE

AA - Antioxidant activity
DPPH - 2,2-diphenyl-1-picrylhydrazyl
Deff - Effective moisture diffusivity
DM - Dry matter
GAE - Gallic acid equivalent
HAD - Hot air drying
HA-MWD - Hot air-assisted microwave drying
MR - Moisture ratio
RMSE - Root mean square error
RP - Red pitaya
RR - Rehydration ratio
SR - Shrinkage ratio
TE - Trolox equivalent
TPC - Total phenolic content
WP - White pitaya

Latin Symbols
L: Half the slice thickness of the sample
M_e: Equilibrium moisture
M_i: Initial moisture content
M_t: Moisture content
R^2: Coefficient of determination

Greek Symbols
χ^2: Chi-square.

REFERENCES

[1] Y. Jiang, W. Yang, J. Taiwan Soc. Hort. Sci. 61(2) (2015) 69-77. https://www.cabidigitallibrary.org/doi/full/10.5555/20153443495.

[2] 2. N. Sengkhamparn, N. Chanshotikul, C. Assawajitpukdee, T. Khamjae, Int. Food Res. J. 20(4) (2013) 1595-1600. http://ifrj.upm.edu.my/20%20(04)%202013/12%20IFRJ%2020%20(04)%202013%20Nopaporn%20(484).pdf.

[3] 3. E. Barcelon, L. Carreon, J. Guillermo, E. Jacob, S. Jocson, J.G. Panopio, S. Rosalinas, Aust. J. Basic Appl. Sci. 9(2) (2015) 18-21. https://www.ajbasweb.com/old/ajbas/2015/February/18-21.pdf.

[4] 4. U. Metin, A. Gezici, Osmaniye Korkut Ata Univ. Fen Bilimleri Enst. Derg. 4(2) (2021) 149-157. https://doi.org/10.47495/okufbed.894470.

[5] 5. W. Liaotrakoon, N. De Clercq, V. Van Hoed, D. Van de Walle, B. Lewille, K. Dewettinck, Food Bioprocess Technol. 6 (2013) 416-430. https://doi.org/10.1007/s11947-011-0722-4.

[6] 6. H. Jiang, W. Zhang, X. Li, C. Shu, W. Jiang, J. Cao, Trends Food Sci. Technol. 116 (2021) 199-217. https://doi.org/10.1016/j.tifs.2021.06.040.

[7] 7. E.J. Bassey, J.H. Cheng, D.W. Sun, Food Chem. 375 (2022) 131886. https://doi.org/10.1016/j.foodchem.2021.131886.

[8] 8. G.V.S. Raj, K.K. Dash, Food Sci. Biotechnol. 31(5) (2022) 549-560. https://doi.org/10.1007/s10068-022-01057-4.

[9] 9. C. Talens, S. Alvarez-Sabatel, Y. Rios, R. Rodriguez, Innov. Food Sci. Emerg. Technol. 44 (2017) 83-88. https://doi.org/10.1016/j.ifset.2017.07.011.

[10] 10. J.R.D.J. Junqueira, J.L.G. Corrêa, D.B. Ernesto, J. Food Process. Preserv. 41(6) (2017) e13250. https://doi.org/10.1111/jfpp.13250

[11] 11. W.A.M. McMinn, J. Food Eng. 72 (2006) 113-123. https://doi.org/10.1016/J.JFOODENG.2004.11.025.

[12] 12. N. Kutlu, A. İşci, Ö.Ş. Demirkol, Gıda 40(1) (2015) 39-46. https://doi.org/10.15237/gida.GD14031.

[13] F.B. Tepe, T.K. Tepe, A. Ekinci, Assoc. Chem. Eng. 28(2) (2022) 151-159. https://doi.org/10.2298/CICEQ210126026T.

[14] J. Crank, The mathematics of diffusion, Clarendon Press, Oxford, (1975). https://www-eng.lbl.gov/˜shuman/NEXT/MATERIALS&COMPONENTS/Xe_damage/Crank-The-Mathematics-of-Diffusion.pdf.

[15] E. Demiray, A. Seker, Y. Tulek, Heat Mass. Transf. 53(5) (2017) 1817-1827. https://doi.org/10.1007/s00231-016-1943-x.

[16] T.K. Tepe, Biomass Convers. Biorefin. 14 (2024) 13513-13531. https://doi.org/10.1007/s13399-024-05562-w.

[17] V.L. Singleton, J.A. Rossi, Am. J. Enol. Vitic. 16 (1965) 144-158. http://doi.org/10.5344/ajev.1965.16.3.144.

[18] K. Thaipong, U. Boonprakob, K. Crosby, L. CisnerosZevallos, D.H. Byrne, J. Food Compos. Anal. 19(6-7) (2006) 669-675. https://doi.org/10.1016/j.jfca.2006.01.003.

[19] Y. Tian, Y. Zhao, J. Huang, H. Zeng, Food Chem. 197 (2016) 714-722. https://doi.org/10.1016/j.foodchem.2015.11.029.

[20] N. Çetin, S. Günaydın, K. Karaman, C. Sağlam, Curr. Trends Nat. Sci. 11(21) (2022) 79-87. https://doi.org/10.47068/ctns.2022.v11i21.008.

[21] N.F.M Nordin, I. Puspasari, S.M. Tasirin, W.R.W. Daud, Y. Gariépy, M.Z.M. Talib, Iran. J. Energy Environ. 5(3) (2014) 313-322. https://doi.org/10.5829/idosi.ijee.2014.05.03.11.

[22] A. Ayala-Aponte, L. Serna-Cock, J. Libreros-Triana, C. Prieto, K. Di Scala, DYNA 81 (2014) 145-151 http://doi.org/10.15446/dyna.v81n188.41321.

[23] M.M. Heydari, T. Najib, O. Baik, K. Tu, V. Meda, Curr. Res. Food Sci. 5 (2021) 73-83. https://doi.org/10.1016/j.crfs.2021.12.008.

[24] M. Sarobol, P. Sarobol, S. Teeta, W. Pharanat, J. Phys.: Conf. Ser. 1144(1) (2018) 012062. https://doi.org/10.1088/1742-6596/1144/1/012062.

[25] I.M.R. Ataides, D.E.C. De Oliveria, W.N.F. Junior, O. Resende, W.D. Quequeto, V.P. Romani, Food Sci. Technol. 43 (2023) 1-8. https://doi.org/10.5327/fst.26323.

[26] F.S.D. Santos, R.M. de Figueirêdo, A.J.D.M. Queiroz, D.D.C. Santos, Rev. Bras. Eng. Agric. Ambiental 21 (2017) 872-877. https://doi.org/10.1590/1807-1929/agriambi.v21n12p872-877.

[27] Z. Zhang, L. Han, T. Jin, Open Phys. 20(1) (2022) 1162-1175. https://doi.org/10.1515/phys-2022-0206.

[28] D. Wang, Y. Wang, R. Pandiselvam, D. Su, H. Xu, Food Bioproc. Tech. (2024) 1-19. https://doi.org/10.1007/s11947-024-03402-3.

[29] Y. Yu, Y. Chen, Y. Wang, X. Sun, Y. Guo, D. Su, H. Xu, Innov. Food Sci. Emerg. Technol. 97 (2024) 103824. https://doi.org/10.1016/j.ifset.2024.103824

[30] E. Horuz, M. Maskan, J. Food Sci. Technol. 52 (2015) 285-293. https://doi.org/10.1007/s13197-013-1032-9.

[31] İ. Doymaz, Chem. Eng. Commun. 203(5) (2016) 599-608. https://doi.org/10.1080/00986445.2015.1056299.

[32] Q. Wang, S. Li, X. Han, Y. Ni, D. Zhao, J. Hao, Food Sci. Technol. 107 (2019) 236-242. https://doi.org/10.1016/j.lwt.2019.03.020.

[33] J.Y. Yi, J. Lyu, J.F. Bi, L.Y. Zhou, M. Zhou, J. Food Process Preserv. 41(6) (2017) e13300. https://doi.org/10.1111/jfpp.13300.

[34] N. Aghilinategh, S. Rafiee, A. Gholikhani, S. Hosseinpur, M. Omid, S.S. Mohtasebi, N. Maleki, Food Sci. Nutr. 3(6) (2015) 519-526. https://doi.org/10.1002/fsn3.241.

[35] S.H. Miraei Ashtiani, B. Sturm, A. Nasirahmadi, Heat Mass Transfer 54 (2018) 915-927. https://doi.org/10.1007/s00231-017-2187-0.

[36] H. Dadhaneeya, R.K. Kesavan, B.S. Inbaraj, M. Sharma, S. Kamma, P.K. Nayak, K. Sridhar, Foods 12(7) (2023) 1387. https://doi.org/10.3390/foods12071387.

[37] M. Angonese, G.E. Motta, N.S. de Farias, L. Molognoni, H. Daguer, P. Brugnerotto, A.C.O. Costa, C.M.O. Müller, Food Sci. Technol. 149 (2021) 111924. https://doi.org/10.1016/j.lwt.2021.111924.

[38] S. Sahin, E. Elhussein, M. Bilgin, J.M. Lorenzo, F.J. Barba, J. Food Process Preserv. 42(5) (2018) e13604. https://doi.org/10.1111/jfpp.13604.

[39] N.A. Al-Mekhlafi, A. Mediani, N.H. Ismail, F. Abas, T. Dymerski, M. Lubinska-Szczygeł, S. Vearasilp, S. Gorinstein, Microchem. J. 160 (2021) 105687. https://doi.org/10.1016/j.microc.2020.105687.

[40] W. Liaotrakoon, Doctoral Thesis, Ghent University (2013). https://biblio.ugent.be/publication/4093845.

[41] K.H. Lee, T.Y. Wu, L.F. Siow, Int J Food Sci. Technol. 48(11) (2013) 2391-2399. https://doi.org/10.1111/ijfs.12230.

[42] M. Ganesapillai, I. Regupathi, T. Murugesan, Chem. Prod. Process Model. 6(1) (2011). https://doi.org/10.2202/1934-2659.1479.

[43] N. Izli, E. Isik, Int. J. Food Prop. 18(2) (2015) 241-249. https://doi.org/10.1080/10942912.2013.829492.

PINAR ŞENGÜN

ÇETIN KADAKAL

Food Engineering Department,
Faculty of Engineering, University of
Pamukkale, Denizli, Turkey.

UTICAJ SUŠENJA VRUĆIM VAZDUHOM I MIKROTALASNIM SUŠENJEM POMOĆU VRUĆEG VAZDUHA NA KINETIKU SUŠENJA I KVALITET KRIŠKI CRVENE I BELE PITAJE

U ovoj studiji sprovedeno je matematičko modelovanje i kinetika sušenja plodova crvene i bele pitaje vrućim vazduhom (HAD) i sušenja mikrotalasima uz pomoć vrućeg vazduha (HA-MWD). Istraženi su, takođe, odnos rehidratacije (RR), odnos skupljanja (SR), promena boje (ΔE), ukupni sadržaj fenola (TPC), antioksidativna aktivnost (AA) i mikrostrukture. Kod obe metode, efektivni koeficijent difuzije (D_{eff}) se povećava sa skraćivanjem vremena sušenja. Dok Pejdžov model najbolje odgovara HA-MWD krivama, HAD krive su definisane modelom parabole. Utvrđeno je da je vrednost RR veća kod HA-MWD metode. Vrednosti TPC svežih plodova crvene i bele pitaje su kao 389,7±0,8 i 310,1±0,4 mg GAE/100 g suve materije (DM), redom. Najviša vrednost TPC plodova sušenih HAD metodom iznosila je 251,4±0,4 mg GAE/100 g DM na 70 °C. Kod plodova sušenih HA-MWD metodom, TPC i AA su se smanjili zbog povećanja snage mikrotalasa. SEM je pokazalo da se veličina pukotina i pora povećava sa povećanjem temperature kod obe vrste voća sušenih HAD metodom. Povećanje snage mikrotalasa je izazvalo veće oštećenje strukture kod HA-MWD metode.

Ključne reči: Pitaja, sušenje, efektivna difuzija, matematičko modeliranje, mikrostruktura.

SATHIYA SELVARAJ[1]

DURAIRAJ SANKARAN[2]

ILANGKUMARAN MANI[3]

[1]Department of Chemistry, Selvam College of Technology, Namakkal, Tamil Nadu, India.

[2]Department of Electrical & Electronics Engineering, Annapoorna Engineering College, Salem, Tamil Nadu, India

[3]Department of Mechanical Engineering, Knowledge Institute of Technology, Salem, Tamil Nadu, India

SCIENTIFIC PAPER

UDC 67/68:581.6:544.526.5

DYE DEGRADATION USING PIPERAZINE-ENCAPSULATED BIOSYNTHESIZED IRON NANOPARTICLES

Highlights

- Biosynthesized Fe nanoparticles were used to degrade aniline yellow dye.
- Piperazine encapsulation increased the degradation efficiency of Fe nanoparticles.
- Performance of piperazine-encapsulated Fe nanoparticles was better under photocatalytic conditions.

Abstract

This study investigated the breakdown of aniline yellow dye using biosynthesized iron nanoparticles that used an extract from Eryngium billardieri. Piperazine encapsulation in a chlorinated environment increased degradation efficiency, reaching up to 92% in the dark and 96% under photocatalytic conditions. Ultraviolet-visible spectroscopy (331.24 nm, 243.19 nm), Fourier Transform Infrared Spectroscopy (Fe-O at 539 cm⁻¹, C-N at 1231 cm⁻¹), X-ray Diffraction analysis (peaks at 26.31° to 76.84°, indicating FCC structure), and Energy Dispersive Spectroscopy (Fe and Cl presence) were used to characterize the nanoparticles. The N-functionalities produced from piperazine and Fe^{2+} (712 eV) were validated by X-ray Photoelectron Spectroscopy. Spherical, evenly distributed particles (10-30 nm) with core-shell morphology were seen by Field Emission Scanning Electron Microscopy and High Resolution Transmission Electron Microscopy. After encapsulation, Photoluminescence analysis showed less electron-hole recombination. Mesoporosity (type IV isotherms) was revealed by Brunauer-Emmett-Teller analysis, and the piperazine coating reduced surface area. Superparamagnetic behaviour with a blocking temperature close to 35K was found via magnetic measurements. High stability, catalytic efficiency, and potential for environmental remediation were all displayed by the encapsulated iron nanoparticles.

Keywords: Dye degradation, Eryngium billardieri, iron nanoparticles, photocatalysis, piperazine.

INTRODUCTION

The textile industry is one of the largest sectors in the global economy, but it is also one of the most polluting, thanks to the widespread use of synthetic dyes. These dyes, with their complex aromatic structures, are highly resistant to degradation and pose significant environmental and health risks if released untreated into natural water bodies. The improper disposal of textile wastewater has resulted in severe contamination of aquatic ecosystems, threatening both marine life and human health [1]. The toxicity of textile waste, particularly when dumped in the environment without proper treatment, has been well documented. According to studies, chemicals in textile effluents, including dyes, are toxic, carcinogenic, and mutagenic, posing serious health risks to humans and animals [2]. Furthermore, the presence of these dyes in water bodies causes reduced light penetration, disrupting photosynthesis and affecting aquatic ecosystems [3]. The impact of textile waste on aquatic systems is significant. The dyes can form a layer on the surface of water bodies, preventing sunlight from penetrating and sustaining aquatic life. This disruption may cause a decrease in the oxygen

levels in the water, resulting in the death of fish and other marine organisms [4]. Furthermore, the accumulation of dyes in sediments can cause long-term ecological damage, affecting biodiversity in the affected areas [5]. Traditional methods for degrading textile dyes, such as physical and chemical treatments, are limited in terms of efficiency, cost, and environmental impact. Biological methods, while environmentally friendly, frequently lack the required speed and efficacy [6]. Recent advances in nanotechnology have opened up new possibilities for the degradation of these persistent pollutants. Biosynthesized nanoparticles, in particular, have shown great promise due to their unique properties and environmentally friendly synthesis processes [7]. Advanced oxidation processes, such as photocatalysis, Fenton reactions, and ozonation, have emerged as efficient dye degradation methods. These techniques depend on the production of reactive oxygen species to break down complex dye molecules into simpler, less harmful compounds [8]. The combination of nano-technology and advanced oxidation processes has further improved degradation efficiency, providing a synergistic approach to pollutant removal [9]. Nanoparticles, with their high surface area-to-volume ratio and unique electronic properties, have been extensively studied for their catalytic abilities in dye degradation. Biosynthesized nanoparticles, in particular, are gaining attention for their green synthesis methods, which avoid the use of hazardous chemicals [10]. These nanoparticles can efficiently catalyze the breakdown of dye molecules, making them a promising tool in waste-water treatment [11]. Nanoparticles can be synthesized using a variety of methods, including physical, chemical, and biological routes. Biological synthesis, also known as biosynthesis, is the environmentally friendly process of producing nanoparticles using microorganisms, plants, or other biological materials. This method not only reduces the use of toxic chemicals but also improves the biocompatibility and functionality of nanoparticles [12]. Different synthesis methods can be optimized to improve nanoparticles' performance in degrading textile dyes [13]. Coating and immobilization techniques can significantly improve the efficacy of nanoparticles for dye degradation. Coating nanoparticles with specific materials can enhance their stability, dispersibility, and reusability, making them more effective in catalytic processes [14]. Immobilization on solid supports can prevent nanoparticle aggregation, facilitate their recovery and reuse, and thus reduce the operational costs and environmental impact of the treatment process [15]. The degradation of textile dyes using biosynthesized nanoparticles is a promising and long-term solution to the environmental problems caused by textile wastewater.

Green nanotechnology has seen significant growth in recent years because of its eco-friendly methodology and potential uses in environmental restoration. A new method for boosting photocatalytic, antibacterial, and antioxidant properties is the creation of metal and metal oxide nanoparticles utilising plant extracts in conjunction with doping techniques. Highlighting the potential of phytochemical routes in boosting catalytic behavior, Kumar *et al.* [16] examined the photocatalytic and antioxidant performance of Co/Ni-doped haematite nanoparticles synthesized using chemical and green approaches. The importance of medicinal plants in nanoparticle synthesis was further supported by Sharma *et al.* [17], who used *Vitex negundo* leaf extract to create Ni and Nd-doped ZnO nanoparticles and reported notable photocatalytic and antibacterial activities.

Using polymer and phytochemical mediation, Kumar *et al.* [18] showed how to synthesize Cu/Zn-doped haematite nanoparticles in an environmentally benign manner while demonstrating exceptional photocatalytic effectiveness and biological compatibility. Using *Murraya koenigii* extract, Verma *et al.* [19] created (Fe, Al)-doped ZnO nanoparticles using a microwave-assisted green technique, achieving significant photocatalytic destruction of contaminants as well as noteworthy antibacterial and antioxidant properties. Similar multifunctional activity was observed by Devi *et al.* [20] in Zn and Gd-doped manganese oxide nanoparticles made with *Pinus roxburghii*, highlighting their potential for antifungal and antibacterial uses. The effectiveness of Co/Zn-doped α-Fe$_2$O$_3$ nanoparticles in water filtration was further highlighted by Kumar *et al.*, demonstrating their superior efficiency and biological safety [21].

Thakur *et al.* [22] investigated the production of chromium and yttrium-doped cobalt oxide nanoparticles with improved multifunctional performance using a green technique. Similarly, Rana *et al.* [23] studied zinc oxide and yttrium-doped zinc oxide nanoparticles, emphasizing their potential for photocatalytic degradation and biological applications. Iron oxide nanoparticles have also attracted substantial interest, with Kumar *et al.* [24] evaluating their origins, advances, and future possibilities in catalysis and environmental remediation. Furthermore, Kumar *et al.* [25] emphasized the importance of nano-bioaugmentation in textile dye cleanup, providing a long-term strategy to health and environmental management.

Thakur and Thakur [26] synthesised Co-Ni-doped TiO$_2$ nanocatalysts having a spherical anatase phase, which efficiently degraded textile colors and scavenged them. Kumar *et al.* [27] used *Azadirachta indica* leaf extract to study the stability, reusability, and efficacy of trimetallic doped haematite (α-Fe$_2$O$_3$) nanoparticles for photocatalytic dye removal. Kumar *et al.* [28] investigated Ni-Zn-doped haematite nanoparticles synthesized from Polyvinyl-pyrrolidone and *Azadirachta indica* leaf extract, which showed improved photocatalytic and radical scavenging characteristics. Thakur and Kumar [29] investigated the effect of shape and size on Co/Ni/Zn triple-doped α-Fe$_2$O$_3$ nanoparticles, exhibiting enhanced photocatalytic and antioxidant properties.

Aquatic ecosystems and human health are seriously threatened by the rising concentrations of synthetic dyes in wastewater, especially from the textile and pharmaceutical sectors. There is a pressing need for more sustainable and effective remediation technologies because conventional treatment procedures frequently fail to remove these persistent contaminants. By combining plant-mediated synthesis and nanomaterial doping to improve photocatalytic and antibacterial capabilities, recent developments in green nanotechnology provide encouraging answers.

Nevertheless, there are still issues with scalability, environmental compatibility, and attaining high efficiency in both light and dark environments.

Green-synthesised doped metal oxide nanoparticles for environmental applications have been the subject of numerous investigations. Verma *et al.* showed improved antioxidant and antibacterial qualities in (Cu, Ce) dual-doped ZnO nanoparticles made utilising *Colocasia esculenta* in a microwave-assisted green method [30]. Similarly, Co/Ni/Zn triple-doped α-Fe₂O₃ nanoparticles' size and shape greatly affected their photocatalytic and radical scavenging capabilities, according to Thakur and Kumar [31], highlighting the significance of carefully planned nanostructure design. The efficiency of green ZnO nanoparticles in breaking down methyl orange dye was highlighted by Thakur *et al.* [32]; however, they also acknowledged that degradation rates varied depending on the environment.

The creation of linked doped TiO₂ nanoparticles, which have demonstrated exceptional photocatalytic, adsorption, and scavenging properties, is another invention [33]. Furthermore, demonstrating the transdisciplinary potential of phytonanotechnology, Balkrishna *et al.* [34] highlighted the use of medicinal plant extracts such as *Catharanthus roseus* and *Ocimum tenuiflorum* in the synthesis of bio-compatible silver nanoparticles for disease management.

By investigating the synthesis, characterization, and application of these nanoparticles, this study hopes to contribute to the development of efficient and environmentally friendly wastewater treatment technologies. The combination of nanotechnology and advanced degradation methods demonstrates the potential for significant advances in environmental remediation.

This research stands out for employing *E. billardieri* extract in the green synthesis of iron nanoparticles, followed by encapsulation with piperazine to enhance their structural and functional properties. The combined approach would significantly boost nanoparticle stability, dispersion, and catalytic activity. By improving both photocatalytic and magnetic properties, this method enables more efficient degradation of aniline yellow dye under both dark and light-driven conditions. The innovative piperazine coating is intended to effectively minimize particle agglomeration, promote uniform size distribution, and enhance superparamagnetic behavior.

Despite many research investigations on green-synthesized nanoparticles utilising plant extracts, little attention has been paid to the use of *E. billardieri* for the biosynthesis of iron nanoparticles, particularly when combined with piperazine encapsulation. While previous research has investigated various doped and plant-mediated nanomaterials for photocatalytic and biomedical applications, there is still a significant gap in developing multifunctional iron-based nanomaterials that combine enhanced photocatalytic efficiency, magnetic responsiveness, and environmental stability using eco-friendly methods. Furthermore, few studies have examined their efficacy in degrading persistent industrial colors such as aniline yellow in both dark and light situations. This study fills a gap by introducing a novel, dual-functional approach–

biosynthesizing iron nanoparticles using *E. billardieri* extract and encapsulating them with piperazine.

MATERIALS AND METHODS

In this investigation, Iron nanoparticles were synthesized utilizing a green method that used *E. billardieri* plant extract as a reducing and stabilizing agent. To improve stability and minimize agglomeration, the synthesized iron nanoparticles were encapsulated in piperazine. This dual-functional synthesis approach is intended to improve the nanoparticles' dispersibility. The resultant piperazine-encapsulated iron nanoparticles were characterized and tested for photocatalytic effectiveness in degrading organic dyes under both dark and photocatalytic environments.

Chemicals and extract preparation

The chemicals used in this study included ferrous sulphate heptahydrate, sodium borohydroxide, sodium hydroxide, 3-chloropropyl-trimethoxysilane, aniline yellow dye, hydrochloric acid, piperazine, and deionised water. Hydrochloric acid was used to clean and dry beakers, funnels, and other chemical processing equipment before use. The *E. billardieri* bioextract was freshly prepared by collecting the plant material and thoroughly washing it with distilled water to remove dirt and impurities. Information regarding the grade, purity, and company for each chemical used has been added in Table 1.

The plant material was cleaned and air-dried at room temperature until completely moisture-free. After drying, the plant material was finely ground into powder with a mechanical grinder. This powder was combined with a suitable solvent, usually ethanol or methanol, and continuously stirred for 24 hours to extract the bioactive compounds. The mixture was then filtered to remove any solid residues, yielding a fresh bioextract ready for use in experiments [35].

Fe nanoparticles synthesis and pipierazine encapsulation

The filtered *E. billardieri* extract was centrifuged for 20 minutes before passing through a Millipore filter. A 0.01M solution of ferrous sulfate heptahydrate was prepared, and the *E. billardieri* extract was combined with this solution in a 4:1 ratio using a magnetic stirrer at room temperature. The bio-synthesized iron nanoparticles were washed three times with deionized water and ethanol before drying in a flask oven at 80 degrees Celsius. For chemically synthesized iron nanoparticles, 1.3336 g of ferrous sulphate heptahydrate was mixed with 2.208 g of sodium borohydride in 160 ml of deionised water and stirred until completely dissolved. The pH was maintained at 6, the solution was cooled to near-freezing, and the mixture was vigorously stirred at 1500 rpm. The synthesis took place at room temperature. The iron nanoparticles were then separated by centrifugation at 6000 rpm for 15 minutes using neodymium magnets, followed by filtering and drying in a vacuum for 10 hours. To prevent contamination, the

Table 1. Details of chemicals used in the experiments.

Chemical Name	Grade	Purity (%)	Supplier/Company
Ferrous Sulphate Heptahydrate ($FeSO_4 \cdot 7H_2O$)	Analytical	99	Merck, India
Sodium Borohydride ($NaBH_4$)	Analytical	98	Sigma-Aldrich, India
Sodium Hydroxide (NaOH)	Analytical	98	Agsar Chemicals, India
Dichloromethane (CH_2Cl_2)	Laboratory	99	Agsar Chemicals, India
3-Chloropropyl-trimethoxysilane (CPTS)	Laboratory	97	Sigma-Aldrich, USA
Potassium bromide (KBr)	Laboratory	98	Agsar Chemicals, India
Hydrochloric Acid (HCl)	Analytical	37 (Conc.)	Merck, India
Aniline Yellow Dye	Laboratory	98	SD Fine Chem, India
Piperazine	Laboratory	99	Sigma-Aldrich, USA
Deionised Water	Laboratory	-	In-house Preparation
E. billardieri bioextract	-	-	Freshly Prepared (In-house)

iron nanoparticles synthesized by *E. billardieri* were stored at ambient temperatures [36]. Mass per mass (%) was used to calculate the iron nanoparticle production yield. In the biosynthetic method, 0.4 g of nanoparticles was generated from 100 mL of *E. billardieri* extract, yielding a 0.4% yield. However, 0.6 g of nanoparticles were produced by chemical synthesis employing 1.3336 g of ferrous sulfate heptahydrate, which corresponds to a higher yield of 0.45%. The solution's chilling to near-freezing temperatures slows the reduction process, resulting in smaller, more homogeneous nanoparticles. The magnetic churning guarantees homogeneity while preventing agglomeration. After production, the nanoparticles are rinsed with deionized water and ethanol to remove unreacted salts and byproducts. The drying stage at 80°C eliminates any remaining solvent, leaving the nanoparticles clean and suitable for further functionalization or application. The nanoparticle formation mechanism is indicated as follows. Iron nanoparticles were synthesized using a reduction process in which Fe^{2+} ions are transformed into Fe^0 using sodium borohydride ($NaBH_4$) in an aqueous solution. Sodium borohydride initiates the reduction process by contributing electrons to Fe^{2+} ions [37]. The overall reaction is as follows:

$$Fe^{2+} + NaBH_4 \rightarrow Fe^0 + Na^+ + BH_3 \qquad (1)$$
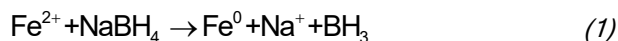
This process produces zero-valent iron (Fe^0), which clusters into nanoparticles. The reduction happens in mild conditions, often at room temperature and pH 6, as determined by the system's buffering capability. Sodium borohydride dissociates in water, producing hydroxide ions (OH^-) that preserve pH and prevent iron nanoparticles from oxidizing excessively [38]. Furthermore, stirring and cooling throughout the reaction facilitate the homogenous creation of iron nanoparticles, which are subsequently separated using centrifugation, filtration, and drying. This approach ensures a regulated synthesis of iron nanoparticles.

To achieve piperazine encapsulation, the iron nanoparticles were chloro-functionalized [39]. First, 1.5 g of synthesized iron nanoparticles were mixed with 35 mL of toluene. Then, 0.75 mL of 3-chloropropyltrimethoxysilane was added, and the solution was gradually heated to 100°C. The resulting chloro-functionalized iron nanoparticles were separated with neodymium magnets and washed with diethyl ether. They were then vacuum-dried. 0.05 g of piperazine was then added to 0.9 g of chloro-functionalized iron nanoparticles in 15 mL of toluene. This mixture was stirred at a low rpm for 6 hours. The resulting piperazine-immobilized iron nanoparticles were washed with diethyl ether, then dichloromethane (CH_2Cl_2), and then dried under vacuum. To assure repeatability, the iron nanoparticles were synthesized in triplicate. Each copy was treated under similar conditions, and the resulting nanomaterials were examined for consistency in size, shape, and other parameters, proving their reproducibility throughout several synthesis runs.

Characterization studies

The properties of the prepared *E. billardieri* bioextract, piperazine, *E. billardieri*-synthesized iron nanoparticles, and piperazine-encapsulated iron nanoparticles were characteri-zed using Ultraviolet-visible spectroscopy (UV-Vis) and Fourier Transform Infrared (FTIR) spectroscopic analysis. The samples were analyzed with the Systronics Double Beam-Make UV-Vis spectrophotometer. Each sample was properly diluted in a suitable solvent to ensure it fell within the measurable absorbance range. To correct the baseline, the spectrophotometer was calibrated with a blank solution containing the same solvent as the sample preparation solution. The samples were placed in a quartz cuvette, and their absorbance was measured from 200 to 800 nm. The UV-Vis spectra revealed information about the samples' electronic transitions, confirming the presence of specific functional groups and the formation of nanoparticles. FTIR was carried out with the Agilent Cary

630-Make FTIR Spectrometer. Solid samples were prepared by combining with potassium bromide (KBr) and pressing into a pellet, whereas liquid samples were placed on the Attenuated Total Reflectance (ATR) accessory. To ensure accurate measurements, the FTIR spectrometer was calibrated with a background scan that contained no samples. Samples were scanned in the mid-infrared range (4000-400 cm⁻¹) to obtain their Infrared Ray (IR) spectra. The resulting spectra revealed information about the functional groups present in the samples by identifying distinct absorption bands. The crystalline structure of the prepared *E. billardieri* extract, piperazine, *E. billardieri*-synthesized iron nanoparticles, and piperazine-encapsulated iron nanoparticles was determined using X-ray diffraction (XRD) testing. The XRD analysis was carried out on the Panalytical X'Pert PRO XRD equipment. To ensure uniformity during testing, the samples were finely ground and evenly distributed on a sample holder. The XRD equipment was calibrated with a standard reference material to ensure accurate measurements. The analysis used a Cu target X-ray source and covered a 2θ range of 10 degrees to 90 degrees with a step count of 0.002 degrees. The samples were exposed to X-rays, and their diffraction patterns were recorded. The diffraction data were used to identify the crystalline phases in the samples and estimate the crystallite size and lattice parameters. This analysis provided detailed information on the crystalline nature of iron nanoparticles and confirmed the successful encapsulation with piperazine. To characterize the surface morphology and chemical composition of *E. billardieri*-synthesized iron nanoparticles and piperazine-encapsulated iron nanoparticles, Field Emission Scanning Electron microscopy (FE-SEM) and X-ray Photoelectron Spectroscopy (XPS) were performed. The FE-SEM analysis was carried out on the JEOL JSM-7600F machine. To improve conductivity, the samples were sputter-coated with a thin layer of gold prior to FE-SEM analysis. The coated samples were then placed in the FE-SEM chamber, where they were imaged under high vacuum at various magnifications to determine surface morphology and particle size. The images revealed detailed information about the shape, size, and distribution of the nanoparticles. The X-ray photoelectron spectroscopy (XPS) analysis was carried out on the Thermo Scientific K-Alpha XPS system. The samples were loaded into the XPS chamber and exposed to monochromatic Al Kα X-rays. The emitted photoelectrons were detected and analyzed to determine the elemental composition and chemical states of the elements found in the samples. XPS spectra were collected over a range of binding energies to determine the presence and oxidation states of elements in both the iron nanoparticles and the encapsulated nanoparticles. The prepared *E. billardieri*-synthesized iron nanoparticles and piperazine-encapsulated iron nanoparticles were subjected to extensive magnetization studies, including Zero-Field Cooled (ZFC) and Field-Cooled (FC) measurements, as well as hysteresis loop analyses at different temperatures. The Lakeshore 7407 Vibrating Sample Magnetometer (VSM) was used to conduct magnetization studies. The samples were cooled to 100 K, 200 K, and 300 K without

an applied magnetic field (ZFC) before being subjected to a magnetic field while cooling (FC). Magnetization was measured as the temperature increased to determine the thermal dependence of magnetic properties. Hysteresis loops were created by changing the magnetic field and measuring the resulting magnetization at temperatures of 100, 200, and 300 K. This analysis provided information about the iron nanoparticle's magnetic behavior and coercivity. Alternating current magnetic (AC) susceptibility tests were carried out using a 4294A Precision Impedance Analyzer. The samples were subjected to alternating magnetic fields with frequencies of 1533 Hz, 5344 Hz, and 9266 Hz. The complex impedance response was measured to determine the frequency dependence of magnetic susceptibility. Integrating these techniques resulted in a thorough understanding of the nanoparticles' magnetic properties and electronic structure.

A scanning electron microscope (SEM) (Make-JEOL JSM-7600F) was used to perform energy-dispersive X-ray spectroscopy (EDS). The synthesized iron nanoparticles and piperazine-iron nanoparticles were analyzed by subjecting them to an electron beam, which stimulated the sample and released X-rays, allowing elemental composition to be determined using observed energy peaks. Photoluminescence (PL) spectroscopy was performed using a spectrofluorometer (Make-Nesara Instruments) and a xenon lamp. The nanoparticles were disseminated in deionized water, with the excitation wavelength set to 350 nm. Emission spectra were acquired between 350 and 600 nm to investigate electron-hole recombination and the enhancement in photocatalytic activity after piperazine encapsulation.

The Micromeritics ASAP 2020 analyzer was used to determine the Brunauer-Emmett-Teller (BET) surface area. Dried iron nanoparticles were vacuum degassed at 150°C for 4 hours. Nitrogen adsorption and desorption isotherms were measured at 77 K. The surface area, pore volume, and pore size distribution were calculated using the BET method.

Batch degradation studies

Water-infused aniline yellow dye was used as a textile industry effluent. This dye was degraded with *E. billardieri*-synthesized iron nanoparticles and piperazine-encapsulated iron nanoparticles in both dark and in the presence of photocatalytic environments. The dye degradation efficiency was calculated using different aniline yellow dye concentrations, nanoparticle quantity, solution pH, ionic strength, and reaction duration. The equation used to calculate the dye degradation efficiency was as follows:

$$\text{Degradation effeciency } \% = \frac{C_o - C}{C_o} \qquad (2)$$

where C_o and C represent the initial concentration and the change in concentration over time, respectively. The absorbance variations were measured with a UV-Vis spectrophotometer. The pH of iron nanoparticles in aniline yellow solution was adjusted by adding sodium hydroxide and hydrochloric acid. To determine ionic strength, aniline

yellow solution was mixed with sodium chloride and iron nanoparticles. The concentration of sodium chloride was increased from 0.05M to 0.1M, resulting in varying dye degradation efficiencies. UV-Vis spectrometry was used to measure the concentration of residual aniline yellow dye after degradation. Iron nanoparticles were isolated and removed from the solution using neodymium magnets.

RESULTS AND DISCUSSIONS

UV-Vis Analysis

UV-Vis spectra of *E. billardieri* extract, piperazine, *E. billardieri* bio-synthesized iron nanoparticles, and piperazine-encapsulated iron nanoparticles are shown in Figure 1.

Figure 1. Ultraviolet-visible spectroscopic analysis of E. billardieri extract, piperazine, E. billardieri bio-synthesized iron nanoparticles, and piperazine encapsulated-E. billardieri-biosynthesized iron nanoparticles.

The UV-Vis spectrum of *E. billardieri* extract, with an absorbance of 331.24 nm, indicates the presence of flavonoids, which are known for their antioxidant and therapeutic properties. This absorbance wavelength corresponds to the electronic transitions characteristic of these compounds, thereby confirming their presence [40]. Piperazine's UV-Vis spectrum shows an absorbance peak at 263.14 nm, indicating the presence of π-π transitions in conjugated systems. This wavelength is characteristic of aromatic amine structures and indicates piperazine's chemical structure. Such absorption characteristics are consistent with studies conducted by Prabavathi *et al.* [41]. The UV-Vis spectrum of *E. billardieri* bio-synthesized iron nanoparticles reveals absorbance peaks at 229.32 nm and 319.83 nm, indicating surface plasmon resonance and electronic transitions. The peak at 229.32 nm corresponds to the surface plasmon resonance effect, whereas the 319.83 nm peak indicates the presence of organic compounds from the plant extract that cover the nanoparticles. This behavior is consistent with findings in recent literature [42], which discuss similar spectral features in green-synthesized nanoparticles. The UV-Vis spectrum of Piperazine-encapsulated *E. billardieri* bio-

synthesized iron nanoparticles reveals an absorbance peak at 243.19 nm. This peak is likely caused by electronic transitions within the encapsulating piperazine, indicating successful encapsulation and potential modification of the nanoparticle surface properties. [43].

FTIR Analysis

FTIR spectra of *E. billardieri* extract, piperazine, *E. billardieri* bio-synthesized iron nanoparticles, and piperazine-encapsulated iron nanoparticles are shown in Figure 2.
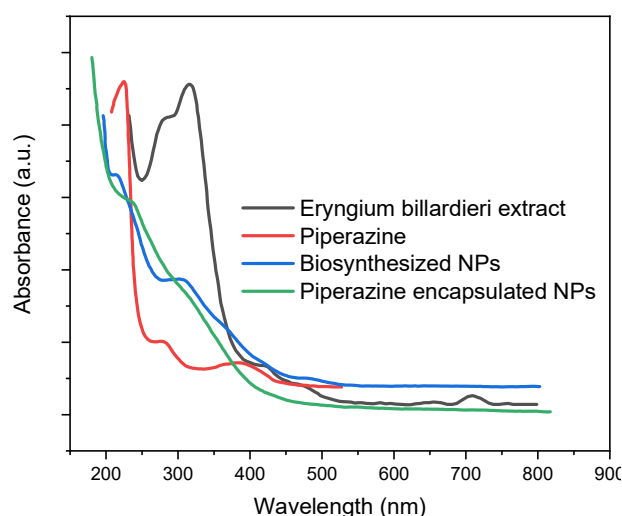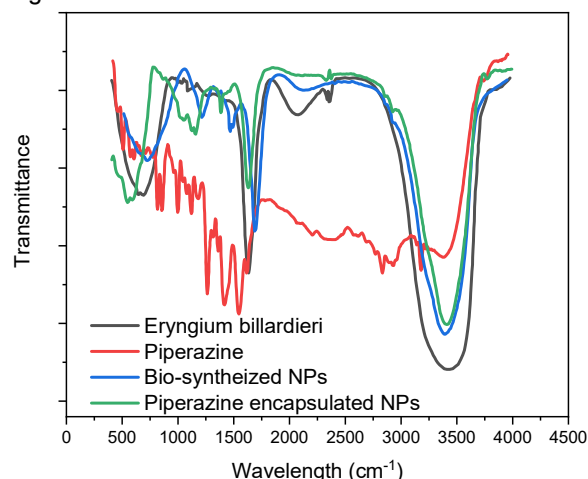

Figure 2. FTIR analysis of E. billardieri extract, piperazine, E. billardieri-biosynthesized iron nanoparticles, and piperazine encapsulated-E. billardieri-biosynthesized iron nanoparticles.

The FTIR spectrum of *E. billardieri* extract shows changes near 585 cm^{-1}, indicating C-X bending vibrations, caused by halogenated compounds. Peaks at 1886 cm^{-1} indicate C=O stretching, which is typical for carbonyl groups. Variations near 2125 cm^{-1} and 2432 cm^{-1} were caused by C≡N stretching vibrations. The broad variations around 3486 cm^{-1} indicate O-H stretching, which confirms the presence of hydroxyl groups [44]. The FTIR spectrum of piperazine exhibits interesting features: variations at 514 cm^{-1} and 572 cm^{-1} suggest C-N bending vibrations; peaks at 825 cm^{-1} and 981 cm^{-1} are characteristic of N-H bending and C-N stretching; 1110 cm^{-1} and 1245 cm^{-1} indicate C-N stretching vibrations; the band at 1406 cm^{-1} reflects N-H bending; 1546 cm^{-1} corresponds to C=C stretching; 2334 cm^{-1} indicates potential C≡N stretching; and broad bands at 2831 cm^{-1}, 3178 cm^{-1}, and 3411 cm^{-1} indicate N-H and C-H stretching [45]. The FTIR spectrum of *E. billardieri* bio-synthesized iron nanoparticles reveals distinct features. Variations at 773 cm^{-1} indicate Fe-O stretching, which is characteristic of iron oxide nanoparticles. Peaks at 1316 cm^{-1} and 1439 cm^{-1} indicate C-H bending and C-N stretching, respectively, likely due to organic capping agents. The peak at 1727 cm^{-1} indicates C=O stretching, while the broadband at 3483 cm^{-1} represents O-H stretching, indicating hydroxyl groups [46]. The FTIR spectrum of Piperazine-encapsulated iron nanoparticles reveals characteristic peaks. At 539 cm^{-1}, indicating Fe-O vibrations; 1106 cm^{-1} and 1231 cm^{-1}, suggesting C-N stretching and N-H bending from the piperazine structure; 1483 cm^{-1}, corresponding to C-H bending; 1769 cm^{-1}, indicating C=O stretching, possibly due to surface

modifications; and a broad band at 3469 cm^{-1}, signifying O-H stretching [47].

X-RD Analysis

XRD spectra of *E. billardieri* bio-synthesized iron nanoparticles and piperazine-encapsulated iron nanoparticles are shown in Figure 3 (a) & (b), respectively.
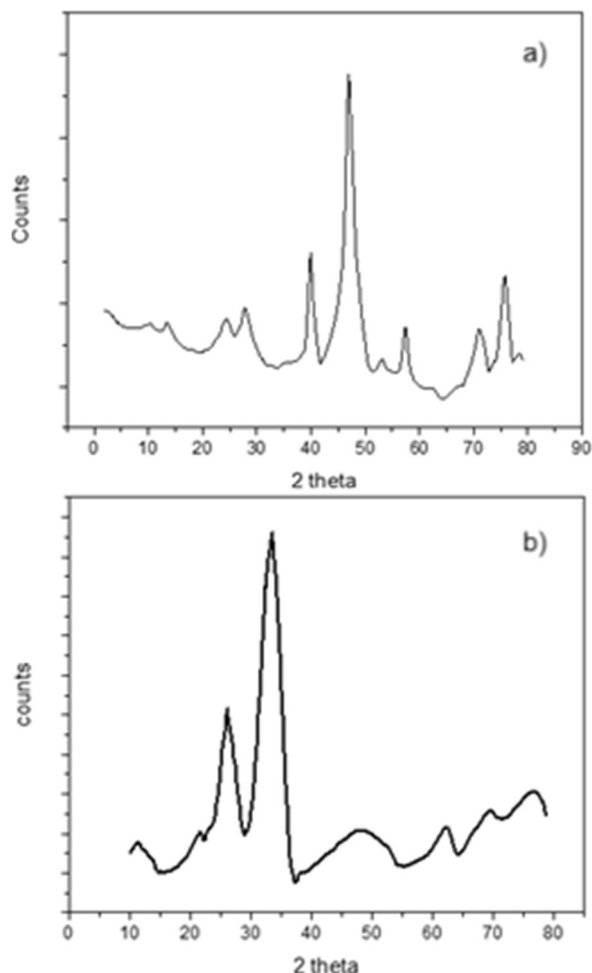

Figure 3. X-ray Diffraction analysis of (a) E. billardieri-biosynthesized iron nanoparticles, and (b) piperazine encapsulated-E. billardieri-biosynthesized iron nanoparticles.

The XRD spectrum of *E. billardieri* bio-synthesized iron nanoparticles reveals peaks at 26.31, 28.29, 39.69, 46.84, 57.41, 71.14, and 76.84 degrees, indicating the nanoparticle's crystalline nature. These peaks correspond to the (110), (200), (211), (220), (310), (222), and (321) planes of face-centered cubic iron, which confirm the formation of iron nanoparticles. [48]. The XRD spectrum of *E. billardieri* bio-synthesized iron nanoparticles shows peaks at 26.31, 28.29, 39.69, 46.84, 57.41, 71.14, and 76.84 degrees, indicating a crystalline structure. These peaks correspond to the (110), (200), (211), (220), (310), (222), and (321) planes of face-centered cubic iron, indicating the formation of iron nanoparticles [49].

The oxidation state of iron in nanoparticles influenced their magnetic properties. Iron oxide nanoparticles, such as Fe_2O_3 (hematite) and Fe_3O_4 (magnetite), exhibited different magnetic behaviors due to their electron configurations [50]. Fe_3O_4, containing both Fe^{2+} and Fe^{3+},

displayed strong magnetism, while Fe_2O_3, primarily composed of Fe^{3+}, showed weak magnetism [51]. Since the iron nanoparticles were synthesized at room temperature, partial oxidation likely occurred, resulting in reduced magnetic strength [52]. XRD analysis was done to confirm whether Fe_3O_4 or Fe_2O_3 was formed by identifying characteristic peaks. The absence of Fe_3O_4 peaks suggests limited magnetism due to the dominance of Fe^{3+} species [53].

Field electron-scanning electron microscopy (FE-SEM)

FE-SEM images of *E. billardieri* bio-synthesized iron nanoparticles and piperazine-encapsulated iron nanoparticles are shown in Figure 4 (a) and (b), respectively.
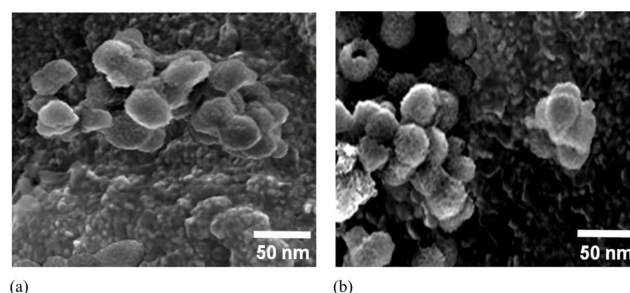

(a)   (b)

Figure 4. FE-SEM images of (a) E. billardieri biosynthesized iron nanoparticles, and (b) piperazine encapsulated-E. billardieri-biosynthesized iron nanoparticles

Figure 4 (a) depicts a FE-SEM image of *E. billardieri* bio-synthesized iron nanoparticles that are spherical and uniformly distributed, with an average size of 20-30 nm. The surface nanostructures have a smooth morphology, indicating effective bio-reduction and stabilization by plant extracts. These findings are consistent with a recent study conducted by Maghsoudy *et al.* [54]. Figure 4(b) shows an FE-SEM image of Piperazine-enca, which showed similar morphology in bio-synthesized iron nanoparticles, confirming the efficacy of using plant extracts for nanoparticle synthesis. Figure 4(b) shows an FE-SEM image of piperazine-encapsulated iron nanoparticles that are well-defined and spherical, with an average size of 20-25 nm. Piperazine molecules are adsorbed onto the surface of iron nanoparticles, forming a protective layer. This process prevented agglomeration, resulting in smooth and uniform surface nanostructures, which improved stability and dispersibility [55].

XPS analysis

The X-ray photoelectron spectroscopy (XPS) analysis indicated a lot of details regarding the surface chemistry, elemental composition, and electronic structure of the piperazine-encapsulated *E. billardieri*-biosynthesized iron nanoparticles. As shown in Figure 5(a), the survey scan confirms the presence of important elements such as carbon (C), oxygen (O), iron (Fe), and nitrogen (N), which together confirm the successful synthesis and piperazine encapsulation. These elemental signals indicate that the encapsulation not only coated the nanoparticle surfaces but also influenced their chemical environment and potential reactivity.

Figure 5(b) shows a high-resolution C1s spectrum with two distinct peaks at 284 eV and 288 eV, corresponding to C-C and C-O bonds, respectively. These peaks represent the incorporation of organic carbon and oxygen-based functional groups produced from piperazine into the nanoparticle surface. Such organic moieties promote colloidal stability and reduce agglomeration, resulting in better nanoparticle dispersion in aqueous systems. These surface alterations also help to reduce surface imperfections, which are common sites of electron-hole recombination. Figure 5(c) reveals a strong signal at 402 eV, indicating CNH $(NH_2)_2^+$ and C-N bonds. These nitrogen-containing groups clearly demonstrate piperazine's effective surface incorporation. Importantly, nitrogen doping or surface functionalization has been shown to reduce charge recombination by modifying the electronic band structure and introducing favorable energy states that enhance charge separation. Thus, the inclusion of nitrogen from piperazine boosted photocatalytic performance by increasing electron lifetimes and promoting more effective redox processes [57].

In Figure 5(d), the O1s spectrum shows a peak at 530 eV, which is consistent with lattice oxygen or oxygen bound in iron oxides/hydroxides. This reveals the presence of Fe-O bonds, which confirms iron oxidation and phase formation. These oxygen environments are essential for photocatalysis because they participate directly in redox reactions with adsorbed species and aid in charge transfer mechanisms. The iron-oxygen interaction also stabilizes the nanoparticle structure, which is required for long-term catalytic activity. The Fe2p spectrum (Figure 5e) shows a peak at 712 eV, representing Fe^{2+} in the Fe2p$_{3/2}$ area. This validates the divalent oxidation state of iron in nanoparticles. The presence of Fe^{2+}, rather than a mixture of Fe^{2+} and Fe^{3+}, is crucial because Fe^{2+} ions are more reactive in Fenton-like processes, which play a key role in dye degradation during photocatalytic conditions. The oxidation state affects the electron transfer kinetics and the ease with which electrons are collected or released during photochemical processes.

Magnetic properties

Piperazine-encapsulated bio-synthesized iron nanoparticles' magnetic properties were evaluated in both zero field-cooled (ZFC) and field-cooled (FC) modes. In ZFC mode, the magnetic moment of Piperazine-encapsulated bio-synthesized iron nanoparticles varies from 30 K to 300 K, as shown in Figure 6. As the temperature drops from 300 K to 30 K, the curve broadens below 80 K, with a blocking temperature of around 35 K. This broadening indicates that the nanoparticles have transitioned from a superparamagnetic to a blocked state, in which the magnetic moments can no longer freely align due to insufficient thermal energy to overcome the anisotropy energy barriers. Magnetization occurs below 180 Oe as the temperature rises from 30 K to 300 K, indicating that nanoparticles can respond to external magnetic fields at lower temperatures [60]. In FC mode, under the same magnetic field, the magnetization of the Piperazine-encapsulated bio-synthesized iron nanoparti-

cles was measured from 300 K to 30 K, as shown in Figure 6 (b). Cusp formation at 15 K and curve inversion indicate a super-paramagnetic nature. This behavior indicates that at lower temperatures, thermal energy is insufficient to randomize the magnetic moments, resulting in a more ordered state. The super-paramagnetic nature of these nanoparticles is critical for biomedical and data storage applications because it enables high magnetic responsiveness without permanent magnetization. The observed magnetic behavior is due to the encapsulation of iron nanoparticles with Piperazine, which stabilizes them and prevents agglomeration, allowing for more precise magnetic interactions. The transition from super-paramagnetic to blocked states, as well as the distinct magnetic responses in ZFC and FC modes, is characteristic of fine iron nanoparticles. Encapsulated nanoparticles exhibit high magnetic susceptibility and low coercivity, making them ideal for a variety of technological applications [61].
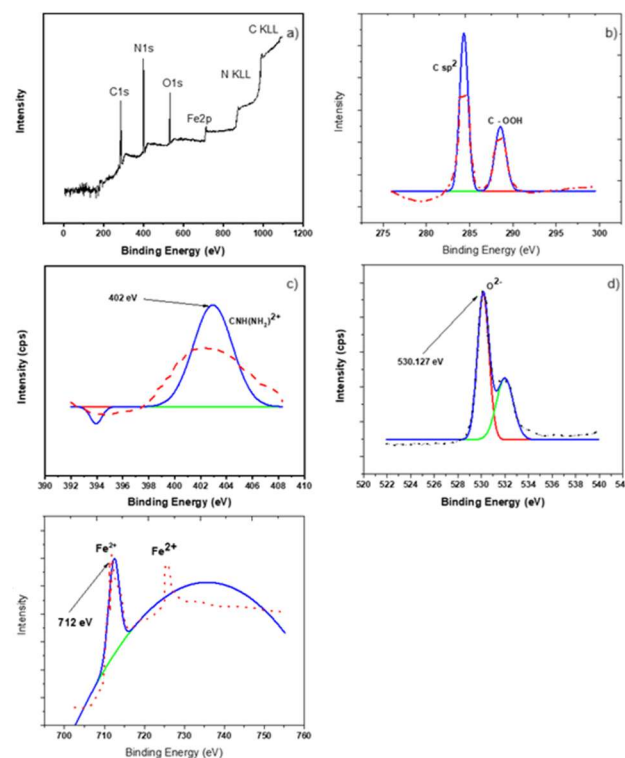
Figure 5. X-ray photoelectron spectrum of piperazine encapsulated - E. billardieri biosynthesized iron nanoparticles (a) survey scan, (b) XPS spectra of C$_{1s}$, (c) XPS spectra of N, (d) XPS spectra of O$_{1s}$, and (e) XPS spectra of Fe2p.

Figure 6 (c) shows hysteresis loops recorded at various temperatures to confirm superparamagnetic behavior in piperazine-encapsulated bio-synthesized iron nanoparticles. The hysteresis loops at 100 K, 200 K, and 300 K show negligible coercivity and remanence, indicating that the nanoparticles do not retain magnetization after being removed from the external magnetic field. This behavior is characteristic of superparamagnetism, in which thermal fluctuations are enough to randomly reorient the magnetic moments of individual nanoparticles, preventing permanent magnetization. At 100 K, the loop becomes slightly more pronounced, indicating some blocking

behavior caused by reduced thermal energy, which is insufficient to fully randomize magnetic moments. As the temperature rises to 200 K and 300 K, the loops narrow and become more linear, indicating that the nanoparticles exhibit superparamagnetic behavior at higher temperatures. This temperature dependence is consistent with the properties of superparamagnetic nanoparticles, where higher temperatures promote thermal agitation, resulting in lower coercivity and remanence [62].

Figure 6. Magnetization studies on piperazine encapsulated-E. billardieri-biosynthesized iron nanoparticles under (a) Zero field-cooled mode, (b) field-cooled mode, (c) hysteresis loops, and (d) AC susceptibility variations.
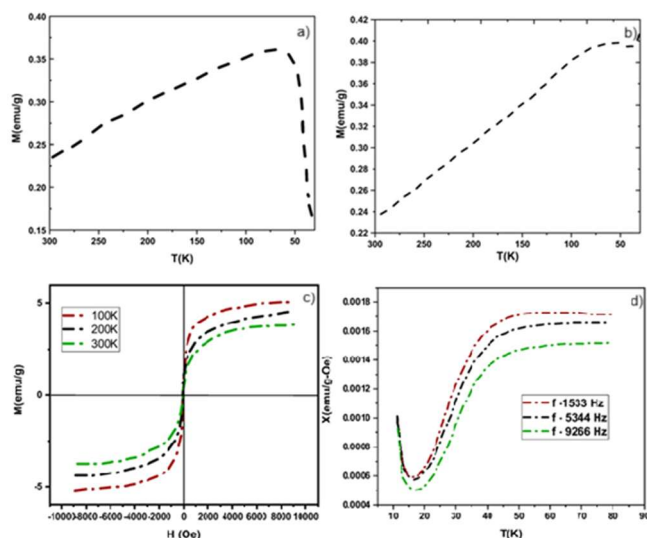
The encapsulation of iron nanoparticles with piperazine improves their stability and prevents agglomeration, resulting in uniform size distribution and consistent magnetic properties. The observed superparamagnetic behavior is consistent with iron nanoparticles that are well-dispersed and small in size and are highly responsive to external magnetic fields without retaining residual magnetization [63]. The spin behavior of the prepared nanoparticles was studied by measuring their AC susceptibility under an applied magnetic field of 1 Oe at three different frequencies: 1533 Hz, 5344 Hz, and 9266 Hz, from 10 K to 80 K, as shown in Fig. 6 (d). The AC susceptibility variations show maxima near the blocking temperature for all three frequencies, indicating a transition from superparamagnetic to blocked state. This behavior is consistent with superparamagnetic nanoparticles, in which magnetic moments are free to align with the field above the blocking temperature but freeze below it because thermal energy is insufficient to overcome anisotropy energy barriers [64]. At all frequencies (1533 Hz, 5344 Hz, and 9266 Hz), the AC susceptibility peaks at the blocking temperature, reflecting the frequency dependence of spin relaxation dynamics. Higher frequencies correspond to faster probing of the magnetic relaxation processes, resulting in shifts in the susceptibility peaks. The similarity in the curve patterns across different frequencies and their resemblance to field-cooled mode magnetic moment variations suggest that the nanoparticles exhibit consistent spin dynamics and magnetic behavior [65].

EDS Studies

EDS spectra of *E. billardieri* biosynthesized iron nanoparticles and piperazine-encapsulated iron nanoparticles are shown in Figure 7 (a) and (b), respectively.

Figure 7(a) depicts the EDS spectrum of *E. billardieri*-synthesized iron nanoparticles, which verifies the presence of elemental iron as the primary component, as well as minor oxygen peaks indicating surface oxidation [66]. Figure 7(b) exhibits the EDS spectrum of piperazine-encapsulated iron nanoparticles, which shows iron peaks alongside excess chlorine. These correspond to piperazine and chloro-functionalization, which demonstrate excellent encapsulation and surface modification, hence enhancing nanoparticle stability and catalytic activity.

Figure 7. EDX-ray spectra of (a) E. billardieri-biosynthesized iron nanoparticles, and (b) piperazine-encapsulated E. billardieri-biosynthesized iron nanoparticles.

Photoluminescence (PL) spectroscopy

The Photoluminescence (PL) spectra of *E. billardieri* biosynthesized iron nanoparticles and piperazine-encapsulated iron nanoparticles are shown in Figure 8 (a) and (b), respectively.

Figure 8. Photoluminescence spectra of (a) E. billardieri-biosynthesized iron nanoparticles, (b) Piperazine encapsulated-E. billardieri bio-synthesized iron nanoparticles.

Figure 8 shows the photoluminescence (PL) spectra, which provide information about the electron-hole recombination kinetics of the synthesized iron nanoparticles. The unaltered iron nanoparticles synthesized with *E. billardieri* extract have modest emission intensity, indicating a higher rate of electron-hole recombination, which affects photocatalytic effectiveness. In contrast, piperazine-encapsulated iron nanoparticles have substantially reduced PL intensity, indicating a strong inhibition of electron-hole recombination. This suggests improved charge carrier separation, which is critical for effective photocatalysis. The lower

43

recombination corresponds directly to the enhanced photocatalytic degradation efficiency seen in the enclosed system. Piperazine most likely functions as a surface passivating and stabilizing agent, preventing fast electron-hole annihilation. Such behavior is consistent with creating materials with higher photoreactivity and stability [67].

BET analysis

The variations in volume adsorbed with relative pressure for *E. billardieri*-biosynthesized iron nanoparticles and piperazine-encapsulated iron nanoparticles are shown in Figure 9 (a) and (b), respectively. Similarly, the fluctuations in pore radius for *E. billardieri*-biosynthesized iron nanoparticles and piperazine-encapsulated iron nanoparticles are shown in Figure 9 (c) and (d).

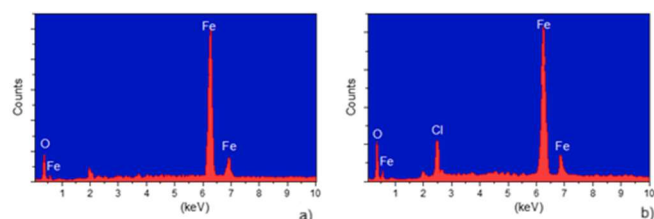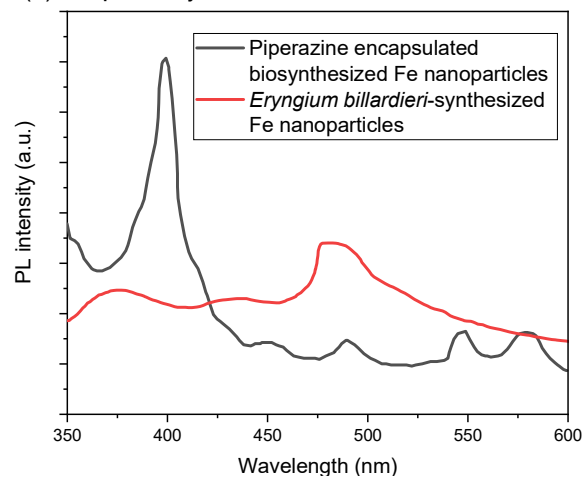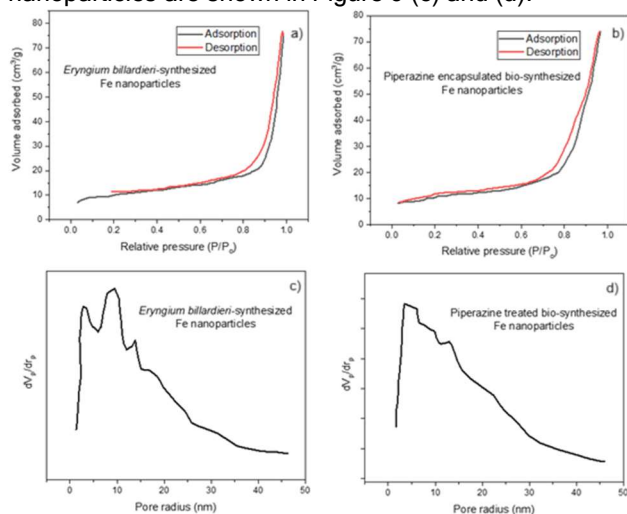Figure 9. BET study indicating adsorption-desorption of (a) *E. billardieri*-biosynthesized iron nanoparticles, b) piperazine encapsulated-*E. billardieri*-biosynthesized iron nanoparticles, (c) pore radius variations of *E. billardieri*-biosynthesized iron nanoparticles, d) pore radius variations of Piperazine encapsulated-*E. billardieri*-biosynthesized iron nanoparticles.

The BET study of *E. billardieri*-synthesized iron nanoparticles (Figure 9(a) and 9(c)) shows a type IV isotherm with a hysteresis loop, indicating mesoporous properties. The adsorption-desorption curve indicates capillary condensation within pores, with pore sizes largely in the mesoporous region (2-50 nm). Figure 9 (c) displays a peak in the pore size distribution, which supports the mesoporous nature. The isotherm remains type IV after piperazine encapsulation (Figure 9(b) and 9(d)), however, there is a modest drop in adsorption capacity, indicating partial pore blockage or surface alteration [68]. The shift in the pore size distribution curve (Figure 9 (d)) indicates a reduction in average pore diameter, most likely due to piperazine occupying certain pore spaces. Overall, piperazine encapsulation reduced pore volume and surface area, improving nanoparticle stability while retaining mesoporous characteristics [69] appropriate for catalytic applications.

High-resolution transmission electron microscopy (HRTEM) studies

The HRTEM images of *E. billardieri* biosynthesized iron nanoparticles and piperazine-encapsulated iron nanoparticles are shown in Figure 10 (a) and (b), respectively. The HRTEM study of *E. billardieri*-synthesized iron nanoparticles (Figure 10(a)) showed uniformly distributed nanoparticles with a spherical morphology and an average size of 10 to 30 nm. The lattice fringes reveal a crystalline structure, verifying the creation of zero-valent iron (Fe^0) nanoparticles [70]. The absence of agglomeration indicates that the bioactive components in the plant extract serve as stabilizers, preventing particle coalescence. Figure 10(b) indicates an HRTEM image of piperazine-encapsulated *E. billardieri*-synthesized iron nanoparticles with a core-shell structure and a thin homogeneous organic layer surrounding the metallic core. This encapsulating layer is due to piperazine functionalization, which improves nanoparticle stability, inhibits oxidation, and minimizes aggregation [71]. The core-shell architecture demonstrates successful surface modification, which improves dispersibility and catalytic effectiveness, making piperazine-coated nanoparticles more efficient in dye degradation.

(a) (b)
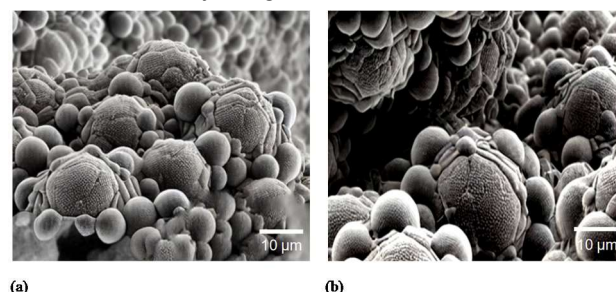
Figure 10 High-Resolution Transmission Electron Microscopy images of (a) E. billardieri bio-synthesized iron nanoparticles and (b) Piperazine encapsulated-E. billardieri bio-synthesized iron nanoparticles.

Batch experiments

Degradation of aniline yellow dye using biosynthesized iron nanoparticles and Piperazine encapsulated *E. billardieri* biosynthesized iron nanoparticles was done. Five sets of batch experiments were conducted such as varying iron nanoparticle quantity, initial dye concentration, reaction duration, ionic strength, and solution pH. The five sets of degradation experiments were conducted in the sun and dark. While varying one parameter, others were maintained as constant. UV-Vis spectrum analysis of the *E. billardieri* biosynthesized iron nanoparticles and piperazine-encapsulated iron nanoparticles on the aniline yellow dye is shown in Figure 11.

The UV-Vis spectroscopy results indicated different absorbance patterns for the two nanoparticle systems during dye degradation. The green line, which represents piperazine-encapsulated iron nanoparticles, showed a faster fall in the distinctive absorbance peak of aniline yellow dye, indicating higher degradation efficiency. This enhanced performance is ascribed to piperazine's involvement in stabilizing iron nanoparticles, minimizing aggregation [72], and facilitating electron transport in the chlorinated environment, resulting in faster dye degradation. The yellow line, representing *E. billardieri*-synthesized iron nanoparticles without piperazine, demonstrated a slower decline in dye absorbance, indicating lower catalytic

efficacy due to probable nanoparticle aggregation and reduced surface area for dye interaction [73].

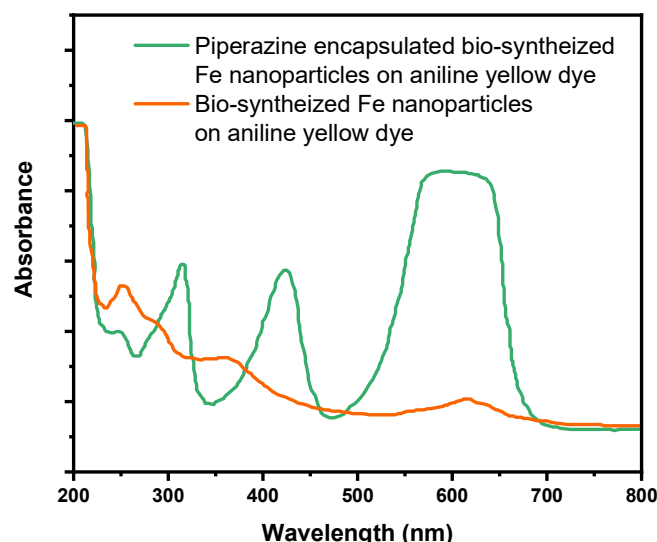*Figure 11. Ultraviolet-visible spectroscopic analysis for degradation studies on dye solution using E. billardieri-biosynthesized iron nanoparticles and piperazine encapsulated-E. billardieri-biosynthesized iron nanoparticles.*

Varying the quantity of iron nanoparticles

The amount of iron nanoparticles used in the dye degradation studies ranged between 1000 mg and 2500 mg (Figure 12 (a)). Other parameters were kept constant, including the initial dye concentration of 225 mg/l, the reaction duration of 250 minutes, the ionic strength of 0.09 M, and the solution pH of 9. The dye degradation efficiency varied according to the amount of iron nanoparticles used. The efficiency of Piperazine-encapsulated iron nanoparticles in a dark environment increased from 71% at 1000 mg/l to 92% at 2500 mg/l. Under photocatalytic conditions, the same nanoparticles demonstrated an increase in efficiency from 75% to 96%. In comparison, untreated biosynthesized iron nanoparticles showed lower degradation efficiencies, beginning at 51% in the dark and 55% under photocatalytic conditions at 1000 mg/l and increasing to 79% and 81%, respectively, at 2500 mg/l. The larger surface area provided for catalytic reactions can explain the increase in dye degradation efficiency with higher concentrations of iron nanoparticles. Iron nanoparticles accelerate the degradation process by catalyzing redox reactions that break down dye molecules into simpler products. Piperazine encapsulation enhances the stability and dispersibility of iron nanoparticles, resulting in improved interaction with dye molecules and higher degradation efficiencies. This encapsulation also improves the nanoparticle's ability to use light energy in photocatalytic environments, as light excites electrons in the iron nanoparticles, resulting in electron-hole pairs that participate in redox reactions [74].

Varying initial concentrations of aniline yellow dye

Dye degradation experiments were carried out by varying the initial dye concentration from 150 mg/l to 300 mg/l (Figure 12 (b)) while holding other parameters

constant: iron nanoparticle quantity at 1750 mg/l, reaction duration at 250 min, ionic strength at 0.09 M, and solution pH at 9. The dye degradation efficiency varied significantly with the initial dye concentration. The efficiency of Piperazine-encapsulated iron nanoparticles in a dark environment increased from 61% at 150 mg/l to 91% at 300 mg/l. Under photocatalytic conditions, the same nanoparticles demonstrated an increase in efficiency from 68% to 95%. In comparison, untreated biosynthesized iron nanoparticles demonstrated lower degradation efficiencies, beginning at 49% in the dark and 54% under photocatalytic conditions at 150 mg/l and increasing to 71% and 79%, respectively, at 300 mg/l. The observed increase in dye degradation efficiency with higher initial dye concentrations can be attributed to the availability of more dye molecules to interact with the iron nanoparticles. These nanoparticles act as catalysts, accelerating the degradation process by redox reactions that break down dye molecules into less complex and less harmful products [75].
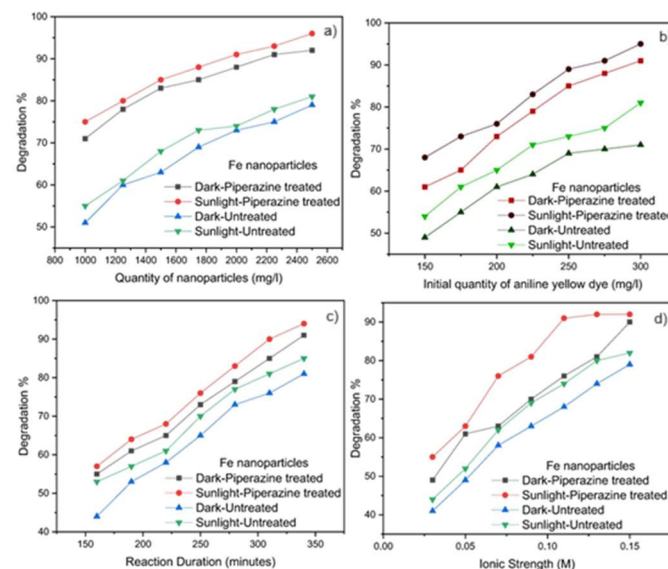
Figure 12. Dye degradation using synthesized nanoparticles on (a) varying the quantity of nanoparticles, (b) varying the initial concentration of aniline yellow dye, (c) varying the reaction duration, and (d) varying the ionic strength of the solution.

Varying the reaction duration

The reaction duration was varied from 160 to 340 minutes to study dye degradation (Figure 12 (c)). Other parameters, such as the quantity of iron nanoparticles (1750 mg/l), the initial dye concentration (225 mg/l), the ionic strength (0.09 M), and the solution pH (9), were held constant. Longer reaction times resulted in increased dye degradation efficiency. The efficiency of Piperazine-encapsulated iron nanoparticles in a dark environment increased from 55% at 160 minutes to 91% at 340 minutes. Under photocatalytic conditions, the efficiency rose from 57% to 94%. In comparison, untreated biosynthesized iron nanoparticles demonstrated lower degradation efficiencies, beginning at 44% in the dark and 53% under photocatalytic conditions at 160 min and increasing to 81% and 85%,

respectively, at 340 min. The observed trend can be explained by the fact that longer reaction times allow the iron nanoparticles to interact with dye molecules, resulting in more complete degradation. The iron nanoparticles accelerate the degradation process by catalyzing redox reactions, which break down dye molecules into simpler and less harmful products [76].

Varying ionic strength of the solution

Dye degradation experiments were carried out by varying the ionic strength from 0.03 M to 0.15 M (Figure 12 (d)) while holding other parameters constant: iron nanoparticle quantity at 1750 mg/l, initial dye concentration at 225 mg/l, reaction duration at 250 minutes, and solution pH at 9. The dye degradation efficiency increased significantly with increasing ionic strength. Piperazine-encapsulated iron nanoparticles in a dark environment increased efficiency from 49% at 0.03 M to 90% at 0.15 M. Under photocatalytic conditions, the efficiency rose from 55% to 92%. In comparison, untreated biosynthesized iron nanoparticles demonstrated lower degradation efficiencies, beginning at 41% in the dark and 44% under photocatalytic conditions at 0.03 M and increasing to 79% and 82%, respectively, at 0.15 M. Higher ionic strength leads to increased electrostatic interactions between dye molecules and nanoparticles, which increases dye degradation efficiency. Higher ionic strength reduces the repulsive forces between negatively charged dye molecules and iron nanoparticles, allowing for closer interaction and more efficient catalytic degradation [77].

Varying the pH of the solution

Dye degradation experiments were carried out by varying the pH of the solution from 3 to 14 while keeping the other parameters constant: iron nanoparticle quantity at 1750 mg/l, initial dye concentration at 225 mg/l, reaction duration at 250 minutes, and ionic strength at 0.09 M. The efficiency of dye degradation varied significantly with pH level. The efficiency of Piperazine-encapsulated iron nanoparticles in a dark environment decreased from 87% at pH 3 to 55% at pH 14. Under photo-catalytic conditions, the efficiency varied from 91% at pH 3 to 61% at pH 14. Similarly, untreated biosynthesized iron nanoparticles demonstrated lower degradation efficiencies, beginning at 81% in the dark and 84% at pH 3, then decreasing to 43% and 53%, respectively, at pH 14. The observed trend is explained by pH's effect on the surface charge and stability of iron nanoparticles, as well as the dye molecules' ionization state. At lower pH levels, the iron nanoparticles are more positively charged, which improves their interaction with negatively charged dye molecules and results in higher degradation efficiencies. As the pH rises, the nanoparticle's surface charge becomes less positive or even negative, reducing its interaction with dye molecules and decreasing degradation efficiency [78]. The present investigation has been compared with the previous literature, and the comparative study is shown in Table 2.

The primary importance of this work is its innovative application of *E. billardieri* extract for the environmentally friendly production of iron nanoparticles, which is comparatively untapped in contrast to materials like TiO₂ and ZnO that are extensively researched. Although doped TiO₂ [26.79] or MnO nanoparticles [80] have shown excellent photocatalytic or antimicrobial performance in earlier studies, this work presents an environmentally friendly, plant-based method to synthesize iron nanoparticles with a similar potential for dye degradation.

This research broadens the material base by investigating iron nanoparticles produced via a sustainable technique, in contrast to earlier publications that mainly concentrate on TiO₂-based materials. The piperazine-encapsulated iron nanoparticles, created via a green technique, show promise for biomedical applications such as targeted medication delivery and environmental remediation. The physicochemical characteristics of the piperazine-encapsulated iron nanoparticles made with *E. billardieri* extract, including improved stability, magnetic responsiveness, and high photocatalytic effectiveness, make them appropriate for a variety of biological uses. Their capacity to operate efficiently in chlorinated settings points to a great deal of promise for targeted drug administration, especially in cancer treatment, where controlled release and site-specific activity are essential. Magnetic-guided delivery systems or magnetic hyperthermia can benefit from the reported magnetic characteristics.

Furthermore, their effectiveness as antioxidants and antimicrobials is demonstrated by their large surface area and the production of reactive oxygen species when exposed to light.

Because of the low toxicity and biocompatibility guaranteed by green production, the nanoparticles are safer for use in biological interactions. The design of next-generation nanomedicine tools based on environmentally benign and scalable fabrication techniques is advanced by these findings, which pave the way for the development of multifunctional nanomaterials that can simultaneously diagnose and treat conditions (theranostics), control infections, and deliver drugs. To improve their stability and selectivity for use in biomedical and environmental applications, future studies could concentrate on surface functionalization of the piperazine-encapsulated iron nanoparticles using biocompatible polymers or ligands. Investigating the impact of adding hybrid nanocomposites or doping with extra metal ions may enhance photocatalytic effectiveness and magnetic behavior even more. Nanoparticle size and shape can be optimized for improved performance by sophisticated reaction control techniques, such as adjusting the synthesis temperature, pH, and precursor ratios. To assess their practical applicability, long-term stability studies in physiological and environmental settings are necessary. Furthermore, evaluating these nanoparticles' cytotoxicity and biocompatibility in *in vivo* models may confirm their safety for use in therapeutic settings.

Table 2. Comparison of the present study with other literature.

Study	Nanomaterial	Synthesis Method	Photocatalytic Activity	Key Findings
Present Study	Iron nanoparticles	Green synthesis using *E. billardieri* extract	Photocatalytic degradation of dyes (to be tested)	Bio-synthesized iron nanoparticles showed promising results for photocatalysis, though further optimization is needed for efficiency.
Thakur *et al.* [79]	Anatase and rutile TiO_2 nanoparticles	Chemical and environmentally friendly methods	Enhanced photocatalytic activity, antibacterial, and antioxidant properties	TiO_2 nanoparticles displayed improved performance with doping methods, particularly in photocatalysis and wastewater treatment.
Devi *et al.* [80]	Zn and Gd-doped MnO nanoparticles	Green synthesis using *Pinus roxburghii* extract	Antifungal, antibacterial, and antioxidant activities	Zn and Gd-doped MnO nanoparticles showed excellent antimicrobial properties, indicating potential for environmental applications.
Thakur & Thakur [26]	Co-Ni-doped TiO_2 nanoparticles	Green and chemical methods	Photodegradation of methyl orange and methylene blue	Co-Ni-doped TiO_2 nanoparticles demonstrated 100% degradation of dyes under UV light, showcasing their efficiency in textile wastewater treatment.

CONCLUSIONS

This study demonstrates that piperazine-encapsulated, *E. billardieri*-mediated iron nanoparticles have substantial potential as efficient catalysts for the breakdown of aniline yellow color. Piperazine's involvement in enhancing reactivity and electron transfer efficiency is highlighted by the improvement in catalytic performance under both dark and photocatalytic conditions, particularly the 96% degradation attained under light exposure. The sensitivity of the degradation process to external conditions was proven by a systematic adjustment of operating parameters, confirming the necessity of precise control in real-world applications. Along with their superparamagnetic characteristics and spin dynamics, the particles' structural integrity, mesoporous nature, and nanoscale homogeneity all point to good dispersibility, recyclability, and applicability in magnetically recoverable systems. Crucially, the observed magnetic behavior adds another level of process tunability, particularly for systems that need external field-driven recovery or targeted control. Collectively, these observations lend credence to the application of such hybrid nanocatalysts in environmentally friendly, scalable wastewater treatment systems.

REFERENCES

[1]   C.R. Holkar, A.J. Jadhav, D.V. Pinjari, N.M. Mahamuni, A.B. Pandit, J. Environ. Manage. 182 (2016) 351-366. https://doi.org/10.1016/j.jenvman.2016.07.090.

[2]   S. Sudarshan, S. Harikrishnan, G. RathiBhuvaneswari, V. Alamelu, S. Aanand, A. Rajasekar, M. Govarthanan, J. Appl. Microbiol. 134 (2023) lxac064. https://doi.org/10.1093/jambio/lxac064.

[3]   A. Srivastava, R.M. Rani, D.S. Patle, S. Kumar, J. Chem. Technol. Biotechnol. 97 (2022) 26-41. https://scijournals.onlinelibrary.wiley.com/doi/epdf/10.1002/jctb.6891.

[4]   M. Behera, J. Nayak, S. Banerjee, S. Chakrabortty, S.K. Tripathy, J. Environ. Chem. Eng. 9 (2021) 105277. https://doi.org/10.1016/j.jece.2021.105277.

[5]   M.T. Islam, T. Islam, T. Islam, M.R. Repon, Text. Leather Rev. 5 (2022) 327-373. https://doi.org/10.31881/TLR.2022.27.

[6]   P. Moradihamedani, Polym. Bull. 79 (2022) 2603-2631. https://doi.org/10.1007/s00289-021-03603-2.

[7]   J. Chaudhary, G. Tailor, M. Yadav, C. Mehta, Biocatal. Agric. Biotechnol. 50 (2023) 102692. https://doi.org/10.1016/j.bcab.2023.102692.

[8]   H. Liu, C. Wang, G. Wang, Chem. - Asian J. 15 (2020) 3239-3253. https://doi.org/10.1002/asia.202000895.

[9]   K. Fedorov, K. Dinesh, X. Sun, R. D. C. Soltani, Z. Wang, S. Sonawane, G. Boczkaj, Chem. Eng. J. 432 (2022) 134191. https://doi.org/10.1016/j.cej.2021.134191.

[10]   N. Shreyash, S. Bajpai, M.A. Khan, Y. Vijay, S.K. Tiwary, M. Sonker, ACS Appl. Nano Mater. 4 (2021) 11428-11457. http://doi.org/10.1021/acsanm.1c02946.

[11]   A. Hosseingholian, S.D. Gohari, F. Feirahi, F. Moammeri, G. Mesbahian, Z.S. Moghaddam, Q. Ren, Mater. Today Sustain. 1 (2023) 100500. https://doi.org/10.1016/j.mtsust.2023.100500.

[12]   J.A. Aboyewa, N.R. Sibuyi, M. Meyer, O.O. Oguntibeju, Plants 10 (2021) 1929. https://doi.org/10.3390%2Fplants10091929.

[13]   S.A. Akintelu, A.S. Folorunso, F.A. Folorunso, A.K. Oyebamiji, Heliyon 6(7) (2020) e04508. https://doi.org/10.1016/j.heliyon.2020.e04508.

[14]   A.M. Alswieleh, ACS Appl. Polym. Mater. 5 (2023) 1334-1343. http://doi.org/10.1021/acsapm.2c01852.

[15]   P.A. Atmianlu, R. Badpa, V. Aghabalaei, M. Baghdadi, J. Environ. Chem. Eng. 9 (2021) 106514. http://doi.org/10.1016/j.jece.2021.106514.

[16]   P. Kumar, A. Kaushik, S. Kumar, N. Thakur, Phys. Sci. 99 (2024) 105960. https://doi.org/10.1088/1402-4896/ad7329.

[17]   S. Sharma, M. Devi, P. Kumar, N. Thakur, K. Kumar, K. Jeet, N. Thakur, Toxicol. Environ. Chem. 107 (2025) 178-206. https://doi.org/10.1080/02772248.2024.2448952.

[18]   P. Kumar, V. Arya, A. Kumar, N. Thakur, Int. J. Mater. Res. 116 (2025) 30-49. https://doi.org/10.1515/ijmr-2023-0343.

[19] N. Verma, D. Pathak, K. Kumar, K. Jeet, S. Nimesh, L. Loveleen, N. Thakur, Mater. Chem. Phys. 333 (2025) 130422. https://doi.org/10.1016/j.matchemphys.2024.130422.

[20] M. Devi, S. Sharma, P. Kumar, N. Thakur, G. Kumar, M.V. Sharma, N. Thakur, Colloids Surf. C Environ. Asp. 2 (2024) 100046. https://doi.org/10.1016/j.colsurfc.2024.100046.

[21] P. Kumar, S. Kumar, A. Tapwal, S. Nimesh, N. Thakur, Sustain. Chem. Environ. 8 (2024) 100160. https://doi.org/10.1016/j.rsce.2024.100160.

[22] S. Thakur, P. Kumar, N. Thakur, K. Kumar, K. Jeet, S. Kumar, N. Thakur, J. Indian Chem. Soc. 101199 (2024). https://doi.org/10.1016/j.jics.2024.101199.

[23] P. Kumar, N. Thakur, K. Kumar, S. Kumar, A. Dutt, V.K. Thakur, N. Thakur, Coord. Chem. Rev. 507 (2024) 215750. https://doi.org/10.1016/j.ccr.2024.215750.

[24] A. Rana, P. Kumar, N. Thakur, S. Kumar, K. Kumar, N. Thakur, Nano-Struct. Nano-Objects 38 (2024) 101188. https://doi.org/10.1016/j.nanoso.2024.101188.

[25] R. Kumar, S. Kaushal, N. Verma, P. Kumar, N. Thakur, A. Kumar, N. Thakur, J. Mol. Liq. 126254 (2024). https://doi.org/10.1016/j.molliq.2024.126254.

[26] N. Thakur, N. Thakur, J. Mater. Sci. Mater. Electron. 35 (2024) 134. https://doi.org/10.1007/s10854-023-11851-3.

[27] P. Kumar, D. Pathak, N. Thakur, Emerg. Mater. (2024) 1-17. https://doi.org/10.1007/s42247-024-00742-w.

[28] P. Kumar, A. Tapwal, S. Kumar, N. Thakur, Adv. Nat. Sci. Nanosci. Nanotechnol. 15 (2024) 025014. https://doi.org/10.1088/2043-6262/ad50bb.

[29] N. Thakur, P. Kumar, Int. J. Nanosci. 23 (2024) 2450010. https://doi.org/10.1142/S0219581X24500108.

[30] N. Verma, D. Pathak, N. Thakur, Next Mater. 5 (2024) 100271. https://doi.org/10.1016/j.nextmat.2024.100271.

[31] N. Thakur, P. Kumar, Int. J. Nanosci. 23 (2024) 2450010. https://doi.org/10.1142/S0219581X24500108.

[32] N. Thakur, N. Thakur, K. Kumar, V. Arya, A. Kumar, S. Kalia, Biomater. Polym. Horiz. 1 (2022) Article 330. https://www.ojs.bdtopten.com/33015.eaapublishing/index.php/bph/article/view/330.

[33] N. Thakur, N. Thakur, J. Dispersion Sci. Technol. (2024) 1-16. https://doi.org/10.1080/01932691.2024.2312841.

[34] A. Balkrishna, N. Thakur, B. Patial, S. Sharma, A. Kumar, V. Arya, R. Amarowicz, Processes 11 (2023) 1479. https://doi.org/10.3390/pr11051479.

[35] M.S. Daneshzadeh, H. Abbaspour, L. Amjad, A.M. Nafchi, J. Food Meas. Charact. 14 (2020) 708-715. https://doi.org/10.1007/s11694-019-00317-y.

[36] I.A. Radini, N. Hasan, M.A. Malik, Z. Khan, J. Photochem. Photobiol. B: Biol. 183 (2018) 154-163. https://doi.org/10.1016/j.jphotobiol.2018.04.014.

[37] S.H. Nguyen, N.T. Vu, H. Van Nguyen, B. Nguyen, T.T. Luong, Environ. Sci. Nano (2025). https://doi.org/10.1039/D4EN00843J.

[38] L. Xu, H.W. Liang, Y. Yang, S.H. Yu, Chem. Rev. 118 (2018) 3209-3250. https://doi.org/10.1021/acs.chemrev.7b00208.

[39] M. Chadha, A. Garg, A. Bhalla, S. Berry, Tetrahedron 150 (2023) 133741. https://doi.org/10.1016/j.tet.2023.133741.

[40] M. Kikowska, M. Dworacka, I. Kędziora, B. Thiem, Rev. Bras. Farmacogn. 26 (2016) 392-399. https://doi.org/10.1016/j.bjp.2016.01.008.

[41] S. SenGupta, N. Maiti, R. Chadha, S. Kapoor, Chem. Phys. 436 (2014) 55-62. https://doi.org/10.1016/j.chemphys.2014.03.011.

[42] D.S. Pattanayak, D. Pal, C. Thakur, S. Kumar, G.L. Devnani, Mater. Today: Proc. 44 (2021) 3150-3155. http://doi.org/10.1016/j.matpr.2021.02.821.

[43] H.N. Prasad, A.P. Ananda, S. Sumathi, K. Swathi, K.J. Rakesh, H.S. Jayanth, P. Mallu, J. Mol. Struct. 1268 (2022) 133683. https://doi.org/10.1016/j.molstruc.2022.133683.

[44] H. Feizi, N. Mollania, H. Mollania, F. Mollania, Research Square (2022) PPR581050. http://doi.org/10.21203/rs.3.rs-2338838/v1.

[45] K. Subashini, S. Periandy, J. Mol. Struct. 1134 (2017) 157-170. https://doi.org/10.1016/j.molstruc.2016.12.048.

[46] N. Sidkey. Al-Azhar, J. Pharm. Sci. 62(2) (2020) 164-179. http://doi.org/10.21608/ajps.2020.118382.

[47] K. Velsankar, G. Parvathy, S. Mohandoss, M. Krishna Kumar, S. Sudhahar, J. Nanostruct. Chem. 12 (2021) 625-640. https://doi.org/10.1007/s40097-021-00434-5.

[48] M. Kaur, D.S. Chopra, Glob. J. Nanomed. 4(4) (2018) 68-76. https://doi.org/10.19080/GJN.2018.04.555643.

[49] M. Mahdavi, F. Namvar, M.B. Ahmad, R. Mohamad, Molecules 18(5) (2013) 5954-5964. https://doi.org/10.3390/molecules18055954.

[50] R. Duglet, D. Sharma, V. Singh, D. Sharma, M. Singh, Solid State Commun. 396 (2025) 115761. https://doi.org/10.1016/j.ssc.2024.115761.

[51] A.R. Pradipta, A. Irunsah, Indones. J. Chem. Stud. 1 (2022) 8-12. https://doi.org/10.55749/ijcs.v1i1.7.

[52] T. Zhang, X. Jin, G. Owens, Z. Chen, J. Colloid Interface Sci. 594 (2021) 398-408. https://doi.org/10.1016/j.jcis.2021.03.065.

[53] R. Foroutan, R. Mohammadi, A. Ahmadi, G. Bikhabar, F. Babaei, B. Ramavandi, Chemosphere 286 (2022) 131632. https://doi.org/10.1016/j.chemosphere.2021.131632.

[54] N. Maghsoudy, P.A. Azar, M.S. Tehrani, S.W. Husain, K. Larijani, J. Nanostruct. Chem. 9 (2019) 203-216. http://doi.org/10.1007/s40097-019-0311-z.

[55] A. Ropp, R. F. André, S. Carenco, ChemPlusChem 88(11) (2023) e202300469. https://doi.org/10.1002/cplu.202300469.

[56]   N.H. Anh, D.V. Nguyen, T.A. Luu, P.D.M. Phan, H.P. Toan, P.P. Ly, H.T. Vuong, Sol. RRL 8 (2024) 2400034. http://dx.doi.org/10.1002/solr.202400034.

[57]   C.C. Ong, R. Jose, M.S.M. Saheed, Chem. Eng. J. 388 (2020) 124306. https://doi.org/10.1016/j.cej.2020.124306.

[58]   C.J. Weststrate, D. Sharma, D. Garcia Rodriguez, M.A. Gleeson, H.O. Fredriksson, J.W. Niemantsverdriet, Nat. Commun. 11 (2020) 750. https://doi.org/10.1038/s41467-020-14613-5.

[59]   P. Nagaraju, C. Srilakshmi, N. Pasha, N. Lingaiah, I. Suryanarayana, P.S. Prasad, Appl. Catal. A Gen. 334 (2008) 10-19. https://doi.org/10.1016/j.apcata.2007.04.024.

[60]   M. Chandran, D. Yuvaraj, L. Christudhas, K.V. Ramesh, Biotechnol. Indian J. 12(12) (2016) 112. https://www.tsijournals.com/articles/biosynthesis-of-iron-NANOPARTICLEs-using-the-brown-seaweed-dictyota-dicotoma.html.

[61]   E. Alphandéry, Int. J. Pharm. 586 (2020) 119472. https://doi.org/10.1016/j.ijpharm.2020.119472.

[62]   A. Miri, H. Najafzadeh, M. Darroudi, M.J. Miri, M.A.J. Kouhbanani, M. Sarani, ChemistryOpen 10(3), (2021), 327-333. https://doi.org/10.1002/open.202000186.

[63]   N. Kobylinska, D. Klymchuk, A. Shakhovsky, O. Khainakova, Y. Ratushnyak, V. Duplij, N. Matvieieva, RSC Adv. 11(43) (2021) 26974-26987. http://doi.org/10.1039/D1RA04080D.

[64]   T. Suneetha, S. Kundu, S.C. Kashyap, H.C. Gupta, T.K. Nath, J. Nanosci. Nanotechnol. 13(1) (2013) 270-278. https://doi.org/10.1166/jnn.2013.7092.

[65]   M. Kin, H. Kura, T. Ogawa. AIP Adv. 6(12) (2016) 125013. https://doi.org/10.1063/1.4972059.

[66]   T. Wang, X. Jin, Z. Chen, M. Megharaj, R. Naidu, Sci. Total Environ. 466 (2014) 210-213. https://doi.org/10.1016/j.scitotenv.2013.07.022.

[67]   A. Rufus, N. Sreeju, D. Philip, J. Phys. Chem. Solids 124 (2019) 221-234. https://doi.org/10.1016/j.jpcs.2018.09.026.

[68]   J. Xu, D. Bhattacharyya, Ind. Eng. Chem. Res. 46 (2007) 2348-2359. https://doi.org/10.1021/ie0611498.

[69]   L. Zhou, Y. He, S. Gou, Q. Zhang, L. Liu, L. Tang, M. Duan, Chem. Eng. J. 383 (2020) 123190. https://doi.org/10.1016/j.cej.2019.123190.

[70]   C. Rodríguez-Rasero, V. Montes-Jimenez, M.F. Alexandre-Franco, C. Fernández-González, J. Píriz-Tercero, E.M. Cuerda-Correa, Water 16 (2024) 1607. https://doi.org/10.3390/w16111607.

[71]   W. Zhou, J. Zhu, C. Cheng, J. Liu, H. Yang, C. Cong, T. Yu, Energy Environ. Sci. 4 (2011) 4954-4961. https://doi.org/10.1039/C1EE02168K.

[72]   Y. Mansourpanah, A. Rahimpour, M. Tabatabaei, L. Bennett, Desalination 419 (2017) 79-87. https://doi.org/10.1016/j.desal.2017.06.006.

[73]   Y. Wang, T. Xiao, S. Zuo, J. Wan, Z. Yan, B. Zhu, X. Zhang, J. Hazard. Mater. 446 (2023) 130698. https://doi.org/10.1016/j.jhazmat.2022.130698.

[74]   M.A. Ahmed, E.E. El-Katori, Z.H. Gharni, J. Alloys Compd. 553 (2013) 19-29. https://doi.org/10.1016/j.jallcom.2012.10.038.

[75]   M. Nemiwal, T.C. Zhang, D. Kumar, Sci. Total Environ. 767 (2021) 144896. http://doi.org/10.1016/j.scitotenv.2020.144896.

[76]   I. Anastopoulos, A. Hosseini-Bandegharaei, J. Fu, A.C. Mitropoulos, G.Z. Kyzas, J. Dispersion Sci. Technol. 39(6) (2018) 836-847. http://doi.org/10.1080/01932691.2017.1398661.

[77]   M. Arellano-Cortaza, E. Ramírez-Morales, U. Pal, G. Pérez-Hernández, L. Rojas-Blanco, Ceram. Int. 47(19) (2021) 27469-27478. http://doi.org/10.1016/j.ceramint.2021.06.170.

[78]   S.H. Ribut, C.A.C. Abdullah, M. Mustafa, M.Z.M. Yusoff, S.N.A. Azman. Mater. Res. Express 6(2) (2018) 025016. http://doi.org/10.1088/2053-1591/aaecbc.

[79]   M. Devi, S. Sharma, P. Kumar, N. Thakur, G. Kumar, M.V. Sharma, N. Thakur, Colloids Surf. C Environ. Asp. 2 (2024) 100046. https://doi.org/10.1016/j.colsuc.2024.100046.

[80]   N. Thakur, N. Thakur, A. Kumar, V.K. Thakur, S. Kalia, V. Arya, G.Z. Kyzas, Sci. Total Environ. 169815 (2024). https://doi.org/10.1016/j.scitotenv.2023.169815.

SATHIYA SELVARAJ[1]

DURAIRAJ SANKARAN[2]

ILANGKUMARAN MANI[3]

[1]Department of Chemistry, Selvam College of Technology, Namakkal, Tamil Nadu, India.

[2]Department of Electrical & Electronics Engineering, Annapoorna Engineering College, Salem, Tamil Nadu, India

[3]Department of Mechanical Engineering, Knowledge Institute of Technology, Salem, Tamil Nadu, India.

NAUČNI RAD

RAZGRADNJA BOJE KORIŠĆENJEM BIOSINTETIZOVANIH NANOČESTICA GVOŽĐA KAPSULIRANIH PIPERAZINOM

U ovom radu, istraživana je razgradnja anilinske žute boje korišćenjem nanočestica gvožđa koje su biosintetizovane ekstraktom Eryngium billardieri. Inkapsulacija piperazina u hloriranoj sredini povećala je efikasnost razgradnje, dostižući i do 92% u mraku i 96% pod fotokatalitičkim uslovima. Za karakterizaciju nanočestica korišćene su UV-VIS (331,24 nm, 243,19 nm), FTIR (Fe-O na 539 cm⁻¹, C-N na 1231 cm⁻¹), RDX (pikovi na 26,31° do 76,84°, što ukazuje na FCC strukturu) i EDS (prisustvo Fe i Cl). N-funkcionalnosti proizvedene iz piperazina i Fe²⁺ (712 eV) potvrđene su XPS-om. Sferne, ravnomerno raspoređene čestice (10-30 nm) sa morfologijom jezgra-ljuske primećene su pomoću FESEM i HRTEM. Nakon enkapsulacije, analiza fotoluminescencije pokazala je manju rekombinaciju elektrona i šupljina. BET analiza je pokazala mezoporoznost (izoterme tipa IV), a piperazin premaz je smanjio površinu. Superparamagnetno ponašanje sa temperaturom blokiranja blizu 35 K je utvrđeno magnetnim merenjima. Enkapsulirane nanočestice gvožđa su pokazale visoku stabilnost, katalitičku efikasnost i potencijal za sanaciju životne sredine.

Ključne reči: degradacija boje, Eryngium billardieri, nanočestice gvožđa, fotokataliza, piperazin.

MARWA MRABET

ADNEN MABROUKI

FAYÇEL AMMARI

Laboratory of Organic Synthesis, Faculty of Sciences Bizerte, University of Carthage, Bizerte, Tunisia.

INVOLVEMENT OF AMINOALKYLATED MERRIFIELD RESINS RETRACTED BY BIS(CHLORODIETHYL) ETHER IN METAL EXTRACTION

Highlights

- Merrifield resin is robust, resisting water and environmental degradation.
- MR-EDA and MR-TETA were synthesized by grafting EDA and TETA onto Merrifield resin.
- Crosslinking with bis(chlorodiethyl) ether produced MR-EDA-BCEE and MR-TETA-BCEE.
- Polymers extracted 50%-85% of Pb^{2+} and Li^+, with MR-TETA-BCEE performing best.
- Modified resins show promise for metal ion recovery and environmental depollution.

Abstract

Merrifield resin, a cross-linked polystyrene resin with chloromethyl functional groups, is an extremely resilient material resistant to water and environmental degradation. The objective was to develop novel substituted polymers with functional groups capable of chelating heavy metals for depollution applications. Cross-linked polymer networks, which are predominantly insoluble and adaptable to diverse chemical environments, are invaluable for pollution management. A key area of environmental significance is the selective retention of organic contaminants for purifying polluted water sources. This work focused on creating new chelating polymeric sorbents for metal extraction by grafting ethylenediamine (EDA) and triethylenetetramine (TETA) onto Merrifield resin, resulting in two polymers: MR-EDA and MR-TETA. These modified polymers were further reticulated with bis(chlorodiethyl) ether to produce two novel reticulated polymers, MR-TETA-BCEE and MR-EDA-BCEE. To characterize the polymers, differential thermal analysis (DTA) and infrared (IR) spectroscopy were employed. The resins were subsequently tested for their ability to extract lead (Pb^{2+}) and lithium (Li^+) ions from aqueous solutions using the solid-phase extraction (SPE) method. Conductivity and atomic absorption spectrometry (AAS) analyses showed high extraction efficiencies, ranging from 50% to 85% for both Pb^{2+} and Li^+ ions. These results demonstrated the potential of MR-EDA-BCEE and MR-TETA-BCEE as effective polymeric sorbents for environmental remediation and heavy metal removal from water.

Keywords: Merrifield resin, ethylenediamine (EDA), chlorodiethyl, metal extraction.

INTRODUCTION

The extraction of metals from water remains a critical area of research, driven by the need to address water pollution caused by toxic metals and their harmful effects on the environment and human health [1], as well as the necessity to recover and recycle certain metal ions that play vital roles in various applications [2]. For instance, lithium has garnered particular attention due to the increasing demand for energy storage materials, such as lithium batteries, and the gradual depletion of natural reserves of this element [3]. Among the various separation techniques, solid-phase extraction (SPE) has emerged in recent years as a preferred method, owing to its technical and economic feasibility [4]. The chemical modification of polymeric resins through the incorporation of functional groups and polar compounds enhances the efficiency of extraction by increasing the surface interaction between the sorbent and

aqueous samples [5]. Organic resins based on styrene-divinyl-benzene copolymers are especially valued for their mechanical stability, resistance to hydrolysis, pH variations, and relatively high-temperature conditions [6]. In this context, several studies have focused on functionalizing Merrifield resins (chloromethylated polystyrene). For example, Slimi *et al* [7] grafted piperazine-based chelating units onto the resin for extracting metals such as Fe^{3+}, Ni^{2+}, Cu^{2+}, Zn^{2+}, and Pb^{2+}. Similarly, Lukashova *et al* [8] substituted tetrahydroxy-thiacalixarenes and tetraphosphonates on Merrifield resin to selectively remove europium (Eu^{3+}) from aqueous solutions. Puig *et al* [9] functionalized Merrifield resin with 2,2-pyridylimidazole, enabling selective separation of nickel from other base metals in synthetic sulfate solutions. Furthermore, the immobilization of bioactive compounds, such as quercetin, on these resins has led to the development of adsorbents capable of recovering Pb^{2+} ions. Other modifications, such as the introduction of polyamines and phosphorus derivatives, have shown effectiveness in extracting metals like Cd, Cu, and Fe [10]. Recent studies have also highlighted the efficiency of a polychloromethylstyrene-based resin modified with heterofluorenone pendant groups and polymers like poly(6-acryloylamino-N-hydroxyhexanamide), which exhibited remarkable adsorption capacities for Cu^{2+} and Pb^{2+} ions under optimal pH conditions [11].

Duan *et al.* [12,13] reported that a poly(6-acryloylamino-N-hydroxyhexanamide) resin effectively adsorbed Cu^{2+} and Pb^{2+} ions. Duan *et al.* [12] reported that a poly(6-acryloylamino-N-hydroxyhexanamide) resin effectively adsorbed Cu^{2+} and Pb^{2+} ions. Ana-Laura *et al.* [13] synthesized three Merrifield-based chelating resins (MR-PDA, MR-DPA, MR-AMP) functionalized with bidentate amines. These resins effectively remove toxic metal ions (Ag^+, Cu^{2+}, Pb^{2+}, Fe^{3+}) from water and are selective, reusable, and pH-tolerant–making them a sustainable solution for water treatment. In this study, two polyamine-supported polymers were prepared from Merrifield resin, modified with ethylenediamine (EDA) and triethylene-tetramine (TETA), and subsequently crosslinked using bis(chlorodiethyl) ether. The complexing properties of these novel sorbents were then studied for the extraction of a heavy metal (lead) and an alkali metal (lithium)

EXPERIMENTAL

Materials

Merrifield resin (MR reticulated by 2% divinylbenzene, 200-400 mesh, 2.1 mmol Cl. g^{-1}, Fluka), EDA, TETA, bis(chlorodiethyl) ether (BCEE), and dimethylformamide (DMF) were purcha-sed from Sigma-Aldrich. Absolute ethanol, triethylamine (TEA), and diethyl ether were purchased from Prolabo. Lithium bromide (LiBr) and lead(II) nitrate ($Pb(NO_3)_2$) were purchased from Fluka.

Synthesis of Merrifield resin with EDA group (MR-EDA)

MR-EDA was synthesized following the procedure reported in the literature [14]. Commercially available

Merrifield resin (2 g) was suspended in 30 cm³ of dimethyl-formamide (DMF) and allowed to swell for 10 hours. EDA (8.4 mmol) was then added to the suspension. An excess of EDA was used to act as a base and accelerate the reaction. The reaction mixture was stirred at room temperature for 1.5 hours, followed by heating at 70-80 °C for 24 hours. Upon completion of the reaction, the resin was thoroughly washed multiple times with deionized water, followed by absolute ethanol, to remove unreacted reagents. The final product (MR-EDA) was dried under vacuum at 50 °C for 48 hours. The resulting material is depicted in Figure 1.

Synthesis of Merrifield resin with TETA group (MR-TETA)

The reaction involved 2 g of MR, 30 cm³ of DMF, and an excess of TETA (8.4 mmol). The reaction conditions of the product were similar to those of MR-EDA (Figure 1).

Synthesis of MR-EDA reticulated by bis(chlorodiethyl) ether (MR-EDA-BCEE)

MR-EDA-BCEE was synthesized according to the method described in the literature [15]. The starting material, MR-EDA (2 g), was dissolved in 30 cm³ of dimethylformamide (DMF), a polar aprotic solvent that facilitates efficient dissolution and ensures the homogeneous mixing of reactants. Bis(chlorodiethyl) ether (BCEE, 6 cm³) was then added to the solution. BCEE was used as a crosslinking agent to introduce additional functional groups, enhancing the resin's chemical properties for its intended application. The reaction mixture was stirred to ensure uniform distribution of BCEE throughout the solution and heated to 125 °C for 24 hours. The elevated temperature was necessary to activate the reaction and promote covalent bonding between MR-EDA and BCEE, ensuring effective crosslinking. Upon completion of the reaction, the resulting product was isolated by filtration to separate the modified polymer from the reaction mixture. The resin was thoroughly washed with distilled water to remove any residual reactants or by-products, ensuring the purity of the final Product. The modified polymer was initially dried at room temperature for 24 hours to remove surface moisture. It was subsequently washed with diethyl ether to remove non-polar impurities and rinsed again with distilled water to ensure all solvents and residual chemicals were eliminated. Finally, the obtained resin (Figure 1) was dried under controlled conditions. It was first oven-dried at 60 °C for 12 hours to remove residual solvents and stabilize the polymer. To achieve complete drying, the resin was subjected to vacuum drying at 70 °C for 48 hours, which removed any remaining moisture or volatile components, resulting in a stable and ready-to-use product.

Synthesis of MR-TETA reticulated by bis(chloroethyl) ether (MR-TETA-BCEE)

The reaction medium contained MR-TETA, DMF, BCEE, and TEA. The reaction conditions of the product were similar to those of MR-EDA-BCEE (Figure 1).

Extraction procedure of metal cations

The work consists of using the modified resins with amino and bis(chlorodiethyl) ether groups for the removal of metal ions (Pb^{2+} and Li^+) using the solid phase extraction method (SPE).

Metal ion extraction method

The kinetics of metal extraction in this experiment involves the interaction between the metal ions (Pb^{2+} and Li^+) and the polymer, where the rate of chelation depends on factors like polymer and metal ion concentration, temperature, pH, and the incubation time. During the incubation, the polymer binds to the metal ions, reducing
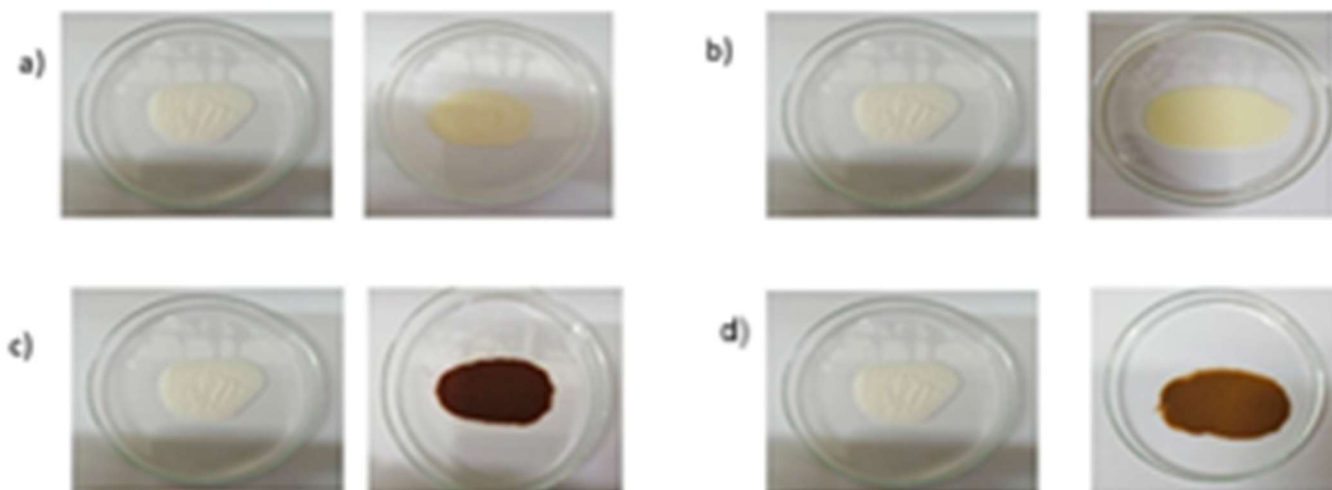
Figure 1 a) Aspect of M_0 and M_1, b) M_0 and M_2, c) M_0 and M_3, and d) M_0 and M_4.
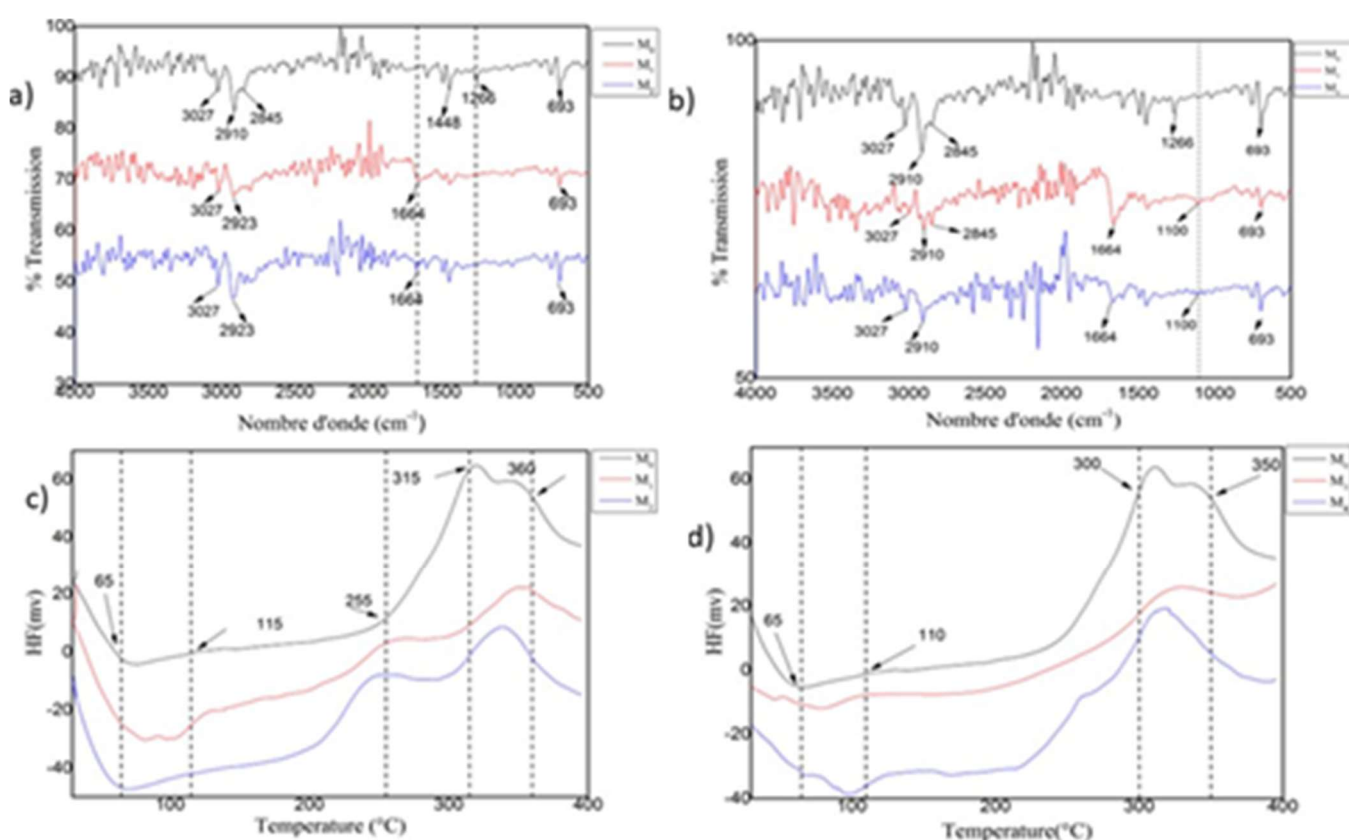
Figure 2 a) ATR-FTIR of M_0, M_1, M_2, b) ATR-FTIR of M_0, M_3, M_4, c) DTA curves of M_0, M_1 M_2, and d) DTA curves of M_0, M_3, M_4.

their concentration in the solution. This chelation process is typically time-dependent, and a time study could be performed to model the kinetics, often following first- or second-order reaction models depending on the reaction

dynamics. After the incubation, the filtrate is analyzed for the remaining metal ions using Flame Atomic Absorption Spectrometry (FAAS), which detects the metal concentration by measuring the absorption of light at characteristic

wavelengths. In this method, the sample is aspirated into a flame where the metal ions are atomized, and their absorption of light is proportional to their concentration. A calibration curve is created using known concentrations of the metal, allowing for the determination of the metal concentration in the filtrate. FAAS detection is sensitive, with detection limits typically in the range of 10^{-9} to 10^{-8} M, and potential interferences such as spectral, ionization, and chemical effects must be considered to ensure accurate measurements. The results were expressed as percentages of extraction of the metal (Table 1, Figure 2). The percentage was calculated using the following expression:

$$\%E=(\sigma_i-\sigma_f)\div\sigma_i \qquad (1)$$

where σ_i is the initial conductivity of the metal in aqueous solution and σ_f is the final conductivity of the metal.

Methods of testing

The infrared analysis using the (ATR FT-IR) technique was carried out on a Thermo Scientific Nicolet FTIR 200 spectrophotometer with a scanning range between 4000 and 400 cm^{-1}. Differential thermal analysis (DTA) was performed on a SETARAM TGA 92 device. The pH was measured with a pH and conductivity meter, VWR/CO 3000L.

RESULTS AND DISCUSSION

IR spectroscopy

The structures of the resulting chelating resins, MR-EDA and MR-TETA, were confirmed using ATR-FTIR spectroscopy, as shown in Figure 2. The ATR-FTIR spectra provided evidence for the successful functionalization of the Merrifield resin. A key observation was the disappearance of the characteristic CH_2-Cl bond, which appears at 1266 cm^{-1} in the spectrum of the Merrifield resin [7]. This disappearance indicates the loss of the chloromethyl functional group during the substitution reaction. In addition, new peaks were observed at 1644 cm^{-1} [16], corresponding to the deformation vibration of NH groups, confirming the incorporation of EDA or TETA into the resin structure. Amines exhibit characteristic bands in infrared spectroscopy, enabling their identification. The N-H stretching vibrations typically appear in the region 3300-3500 cm^{-1}. Primary amines (−NH_2) show two bands in this region, corresponding to symmetric and asymmetric stretching, while secondary amines (−NH) display only one. These bands are usually broad and of moderate intensity. Another characteristic band, associated with N-H bending vibrations, is found in the region 1500-1650 cm^{-1}. Lastly, the C-N stretching vibration appears between 1200 and 1350 cm^{-1}. These features help distinguish between primary, secondary, and tertiary amines in a mixture or compound. This observation is consistent with findings by Kadous *et al.* [12], who reported a similar peak at 1602 cm^{-1} in polystyrene resin grafted with EDA. These spectroscopic changes collectively support the substitution of the chloro group by polyamine groups. For the resins MR-EDA-BCEE and MR-TETA-BCEE, the ATR-FTIR spectra (Figure 2) displayed all the characteristic bands observed for MR-

EDA and MR-TETA. Additionally, a new valence band was detected at 1100 cm^{-1}, corresponding to the C-O-C stretching vibration. This band indicates the successful grafting of the bis(chlorodiethyl) ether group onto the amino-functionalized Merrifield resins. Similar findings were reported by Mbarki *et al.* [15], who observed a C-O-C band in the range of 1050-1170 cm^{-1} for amino-PVC modified with bis(chlorodiethyl) ether.

DTA analyses

The DTA curves of MR-EDA, MR-TETA, MR-EDA-BCEE, and MR-TETA-BCEE (Figure 2) showed that all resins present two peaks, an exothermic peak between 300 and 360 °C that could indicate their decomposition, and an endothermic peak between 65 and 115 °C that can be explained by the evaporation of residual water. Dardouri *et al.* [10] observed the same decomposition peaks at 305, 330, and 509 °C.

Metal ion extractions by the synthesized polymers

The extraction was also performed using the atomic absorption spectrometry technique. Table 1 shows the heavy metal extraction determined by conductivity measurements and by AAS. The difference between the extraction percentages determined by these two methods (the absorption and conductivity methods) is between 8% and 12%.

Effect of initial pH on modified Merrifield resins

The pH of the aqueous phase plays a crucial role in the extraction of Pb^{2+} and Li^+ ions by an extracting agent. It influences both the chemical behavior of the functional groups in the functionalized resin and the nature of the species present in the solution. Studying the retention efficiency of lead and lithium ions as a function of pH helps determine the optimal conditions for the extraction process. The effect of pH on the extraction of these ions was examined within the pH range (1.0-6.0), using an aqueous solution containing 2×10^{-4} M of Pb^{2+} and Li^+. A volume of 30 mL of this solution was treated with 0.1 g of resin, while the agitation speed was kept constant at 250 rpm using a vibrating platform. The results show that the extraction efficiency of Pb^{2+} and Li^+ ions increases with pH, reaching a maximum of 80% at pH 6.1 (Table 2). At low pH, the high concentration of H^+ ions in solution leads to competition between protons and Pb^{2+}/Li^+ ions for extraction. Additionally, in an acidic medium, the lone electron pairs of the nitrogen and oxygen atoms in the Merrifield resin are blocked by H^+ ions, reducing their availability for complexation with metals. Furthermore, in an environment rich in H^+, these ions strongly adsorb onto the resin, giving it a positive charge that creates electrostatic repulsion, thereby limiting the approach of Pb^{2+} and Li^+ ions.

The extraction percentages of metal ions Pb^{2+} and Li^+ with the chelating resins M1, M2, M3, and M4 are shown in Table 1 and Figure 3. The values are between 50% and 85%, which indicates that all resins are of a high metal nature for both Pb^{2+} and Li^+. Figure 3 shows that the order of adsorption capacity of the chelating resins against Pb^{2+} and Li^+ ions is as follows: MR-TETA > MR-EDA, which is

similar to other investigations [9,11]. This result was explained by the higher content of nitrogen groups (% N) in modified resins, which improves coordination with metallic ions. The extraction percentages of Pb^{2+} and Li^+ with the synthesized polymers MR-EDA, MR-TETA, MR-EDA-BCEE, and MR-TETA-BCEE varied between 65.6 and 85.5% and 50 and 87%, respectively. All the synthesized polymers showed more selectivity for the Pb^{2+} which has a higher size than Li^+, these results can be explained by the compatibility factor between the size of the Pb^{2+} ion and the size of the complexing cavity in the polymers, which could be influenced by the cross-linking degree, the length of amine chain and the cross-linking by the bis(chlorodiethyl) ether is directly proportional. However, the active sites are less readily available, and the efficiency of the resin is reduced. The orders of adsorption capacity for Pb^{2+} were respectively: MR-TETA-BCEE > MR-EDA-BCEE > MR-TETA > MR-EDA. Besides, the orders of adsorption capacity for Li^+ are as follows: MR-TETA-BCEE > MR-TETA> MR-EDA-BCEE> MR-EDA. When looking at all the results, as an average of all polymers, we can observe that the synthesized polymer that is the best extractant and the most selective for both Pb^{2+} and Li^+ is MR-TETA-BCEE, respectively, with 85.5% and 78%. This high adsorption selectivity could be explained by the high affinity of Pb^{2+} and

Li^+ ions to the polyamine and oxygen groups in the studied resins, which can fix the metal through non-cova-lent bonds (van der Waals bonds) as shown in Figure 5. This extraction efficiency could also be partially explained by the electro-negativities of the substituted nitrogen of the polyamine and oxygen groups. In the case of Li^+, the polymer M4 (78 %) is the better extractant; Li^+ is less voluminous than Pb^{2+}. Based on the hard-soft acid-base theory, Li^+ has affinities to hard ligands, which contain oxygen atoms like in M_4 more than Pb^{2+} [18-19].

Kinetic study

Figure 3 shows variation curves of average electrical conductivity with time for metal cations Pb^{2+} and Li^+ in contact with the modified polymers (M1, M2, M3, and M4). The kinetic study showed that the optimum extraction time obtained was approximately 35 h and 22 h for Pb^{2+} and Li^+ extraction, respectively. The extraction results are the average of three experiments. These results show that all modified resins M_1, M_2, M_3, and M_4 give better results (shorter extraction durations) with Li^+ cation. However, the development of new chelating ion exchange materials with special chelating properties can provide better kinetics of interaction between metal ions and chelating groups [6].

Table 1 Extraction percentage results of metal ions (Pb^{2+}, Li^+) by the synthesized polymers.

Metal cation	%with M_1	AAS	%with M_2	AAS	%with M_3	AAS	%with M_4	AAS
	Conductivity		Conductivity		Conductivity		Conductivity	
Pb^{2+}	65.6	57.6	73	61	82.6	72.6	85.5	75
Li^+	50	42	68.3	55.7	57.4	47	78	68

Table 2. Extraction Percentages of Pb^{2+} and Li^+ Ions as a Function of pH (M1 to M4).

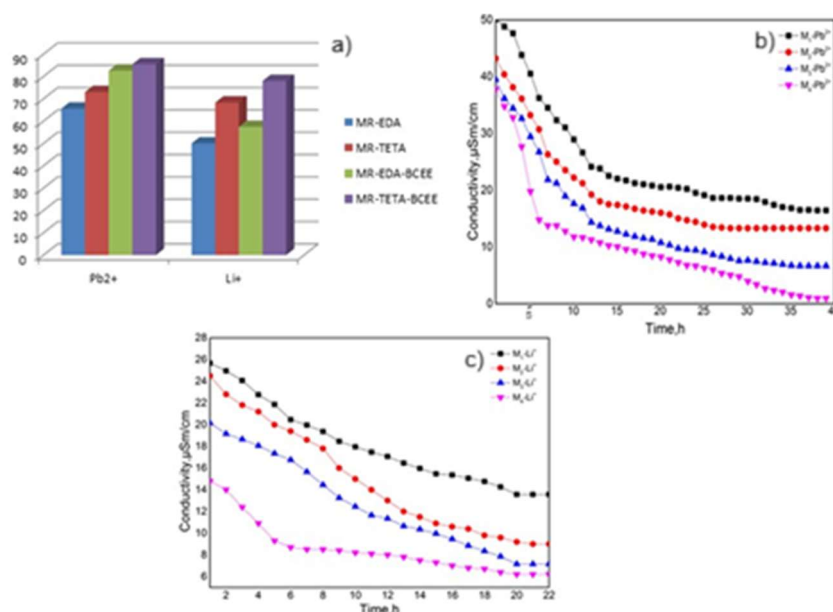| Metal cation	%with M_1 to PH=2.0	%with M_2 to PH=3.0	%with M_3 to PH=5.1	%with M_4 to PH=6.1
Pb^{2+}	62	70	80	83
Li^+	45	63	55	75

Figure 3 a) Percentages of metal ions extraction for the polymers M_1, M_2, M_3, and M_4, b) curves of the optimal duration of Pb^{2+} extractions, and c) curves of the optimal duration of Li^+ extractions.
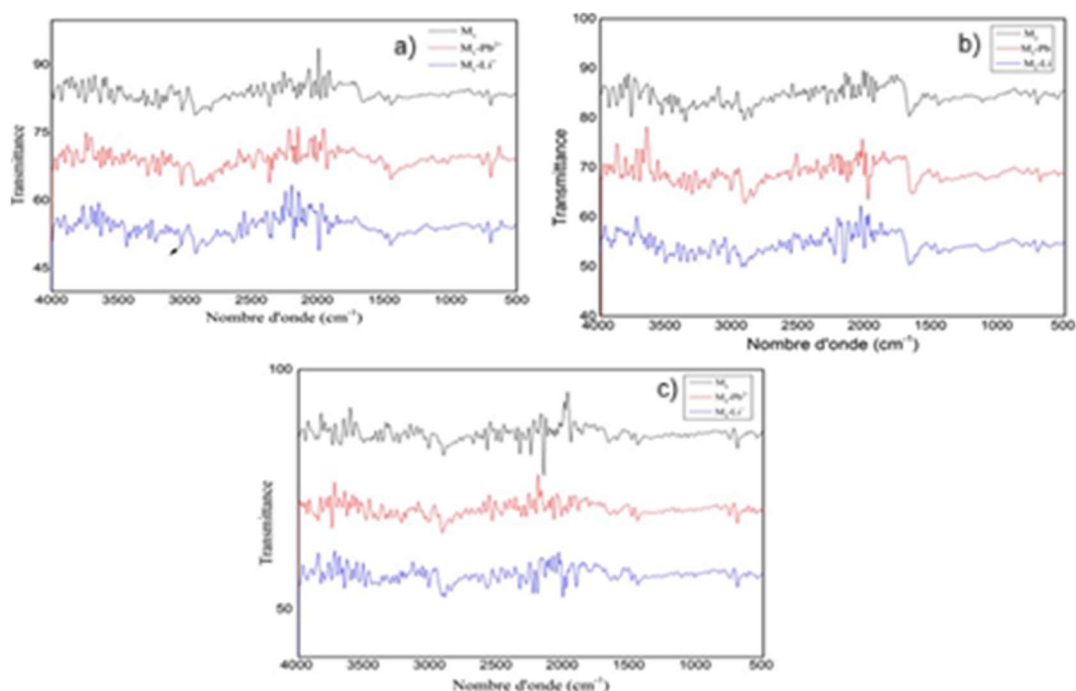
Figure 4 IR spectra of (a) polymer M_1 and complex M_1-Pb^{2+}, M_1-Li^+; (b) polymer M_2 and complex M_2-Pb^{2+}, M_2-Li^+; and (c) polymer M_4 and complex M_4-Pb^{2+}, M_4-Li^+.
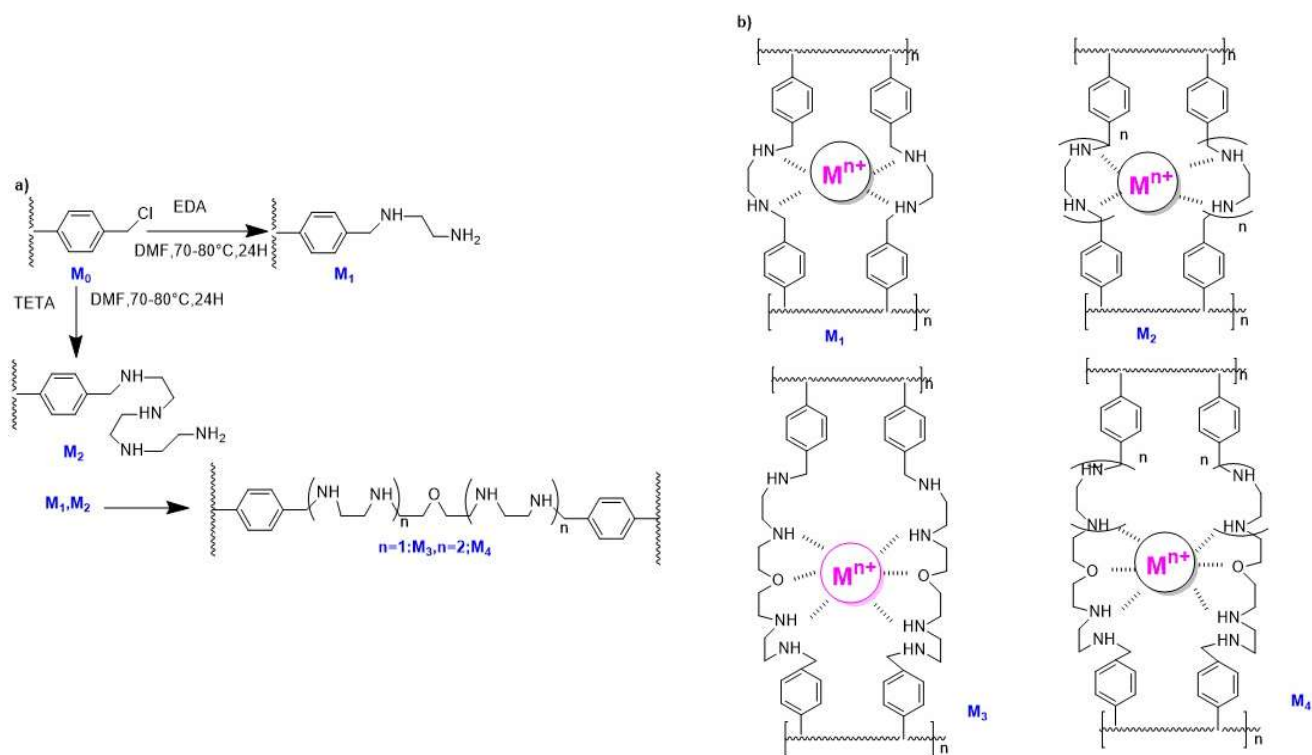
Figure 5 (a) Proposed structure of polyamine resin, and (b) Proposed complex structures of M_1, M_2, M_3, and M_4 with M^{n+}: Li^+ or Pb^{2+}

The demonstration that metal coordination occurs through amines and not simply via "entanglement" in the Merrifield resin is based on several observations from Figure 5. Graph (a) shows that resins functionalized with amines (MR-EDA, MR-TETA, and their derivatives) exhibit higher adsorption rates for Pb^{2+} and Li^+, suggesting a specific chemical interaction involving amine groups. Graphs 4 (b) and (c) illustrate a progressive decrease in solution conductivity over time, indicating the extraction of metal ions. The difference in kinetics among the resins (M_1, M_2, M_3, and M_4) and their superior performance for Pb^{2+}, which has a higher affinity for amines due to its electronic properties, supports the hypothesis of metal-amine coordination. This selective behavior and the dependence on the type of amine confirm that the interaction is chemical and specific, rather than a mere physical entanglement.

Influence of extracted metals on the IR spectra of new resins

The IR absorption spectra of the studied complexes in Figure 4 indicate that the influence of free polymers and their complexes on the IR spectra is not very significant. Ammari *et al.* [17] found the same observation with functionalized PVC, explaining it by the effect of the counter-anions of the used salts.

CONCLUSION

In this study, we demonstrated the efficiency of modified Merrifield resin-based polymers for extracting Pb^{2+} and Li^+ ions from aqueous solutions. The integration of polyamine groups, followed by cross-linking with bis(chlorodiethyl) ether, enhanced the adsorption capacity of the polymers, with a particularly high performance for lead extraction. Among the synthesized materials, MR-TETA-BCEE proved to be the most effective, highlighting the influence of functional group type and structure on selectivity and extraction efficiency. These findings suggest that the developed polymers could be promising candidates for water decontamination and the selective recovery of industrially valuable metals. Further investigations, particularly on the reusability of the resins and their efficiency under real-world conditions, will be necessary to fully assess their potential for industrial and environmental applications.

REFERENCS

[1] G. Pina-Luis, G.A. Rosquete Pina, A.C. Valdés Gonzaléz, A.O. Teran, I.R. Espejel, M.E. Diaz-Garcia, React. Funct. Polym. 72 (2012) 61-68. https://doi.org/10.1016/j.reactfunctpolym.2011.10.003.

[2] A. Sigel, H. Sigel, R.K.O. Sigel, Springer International Publishing, Basel, Switzerland (2016), https://doi.org/10.1007/978-3-319-21756-7.

[3] H. Zhang, J. Hou, Y. Hu, P. Wang, R. Ou, L. Jiang, J.Z. Liu, B.D. Freeman, A.J. Hill, H. Wang, Anal. Sci. Adv. 4 (2018) 0066. https://doi.org/10.1126/sciadv.aaq0066.

[4] L.A. Berrueta, B. Gallo, F. Vicente, J. Chromatograph, 40 (1995) 474-483. https://doi.org/10.1007/BF02269916.

[5] M.E. Leon-Gonzale, L.V. Perez-Arribas, J. Chromatogr. A 902 (2000) 3-16. https://doi.org/10.1016/S0021-9673(00)00942-0.

[6] D. Sud, Ion Exchange Technology I, Springer: Dordrecht, Holland (2012), p 376. https://doi.org/10.1007/978-94-007-4375-5_13.

[7] R. Slimi, R. Ben Othman, N. Sleimi, A. Ouerghui, C. Girard, Polymers 8 (2016) 187-193. https://doi.org/10.3390/polym8050187.

[8] M.S. Lukashova, K.N. Belikov, K.Y. Bryleva, S.G. Kharckenko, S.G. Vishnevsky, V.I. Kachenko, Adv. Funct. Mater. 23 (2016) 111-119. https://doi.org/10.15407/fm23.01.111.

[9] S.F. Puig, L. Alberto, V.V. Becerra, A.O. Teran, A.C. Ramírez, A.V. González, Mater. Res. Express. 11 (2019) 104-115. https://doi.org/10.1088/2053-1591/ab4470.

[10] M. Dardouri, F. Ammari, F. Mgananem J. Polym. Sci. 6 (2015) 782841. https://doi.org/10.1155/2015/782841.

[11] B. Zou, S. Zhang, P. Sun, Z. Ye, Q. Zhao, W. Zhang, L. Zhou, J. Colloid Interface Sci. Commun. 40 (2021) 100349. https://doi.org/10.1016/j.colcom.2020.100349.

[12] G. Duan, C. Zhanfang, H. Zhong, X. Ma, S. Wang, J. Environ. Manage. 308 (2022) 114631. https://doi.org/10.1016/j.jenvman.2022.114631.

[13] A.L. Villa-Reyna, M. Aguilar-Martínez, A. Ochoa-Terán, H. Santacruz-Ortega, M.A. Leyva-Peralta, J.T. Vargas-Durazo, J.C. Gálvez-Ruiz, Polymers 15 (2023) 2778. https://doi.org/10.3390/polym15132778.

[14] R. Qu, J. Liu, C. Sun, Y. Zhang, C. Ji, P. Yin, J. Chem. Eng. 55 (2010) 4650-4659. https://doi.org/10.1021/je100246y.

[15] F. Mbarki, F. Ammari, A.B.H. Amor, F. Meganem, Polymery 62 (2017) 109-117. https://doi.org/10.14314/polimery.2017.109.

[16] A. Kadous, M.A. Didi, D. Villemin, J. Radioanal. Nucl. Chem. 284 (2010) 431-438. https://doi.org/10.1007/s10967-010-0495-7.

[17] F. Ammari, F. Meganem, Turk. J. Chem. 38 (2014) 638-649. https://doi.org/10.3906/kim-1306-24.

[18] A. Ouerghui, M. Dardouri, N. Sleimimi, A. Bel Hadj Amor, F. Ammari, C. Girard, Polimery, 64 (2019) 3-11. https://doi.org/10.11648/j.ajpst.20190503.11.

[19] M. Dardouri, F. Ammari, A. Bel Hadj Amor, F. Meganem, Mater. Chem. Phys. 216 (2018) 435-445. https://doi.org/10.1016/j.matchemphys.2018.06.002.

MARWA MRABET

ADNEN MABROUKI

FAYÇEL AMMARI

Laboratory of Organic Synthesis, Faculty of Sciences Bizerte, University of Carthage, Bizerte, Tunisia

NAUČNI RAD

UČEŠĆE AMINOALKILIRANIH MERIFILD SMOLA RETRAKCIRANIH BIS(HLORODIETIL)-ETROM U EKSTRAKCIJI METALA

Merifild smola, umrežena polistirenska smola sa hlorometil funkcionalnim grupama, izuzetno je otporan materijal na vodu i degradaciju u životnoj sredini. Cilj rada je bio razvijanje novih supstituisanih polimera sa funkcionalnim grupama sposobnim da heliraju teške metale za primene u prečišćavanju. Umrežene polimerne mreže, koje su pretežno nerastvorljive i prilagodljive različitim hemijskim sredinama, neprocenjive su za upravljanje zagađenjem. Ključno područje od ekološkog značaja je selektivno zadržavanje organskih zagađivača za prečišćavanje zagađenih izvora vode. Ovaj rad je fokusiran na stvaranje novih helatnih polimernih sorbenata za ekstrakciju metala kalemljenjem etilendiamina (EDA) i trietilentetramina (TETA) na Merifild smolu, da bi se dobila dva polimera: MR-EDA i MR-TETA. Ovi modifikovani polimeri su dalje retikulirani bis(hlorodietil) etrom, pri čemu se dobijaju dva nova retikulisana polimera, MR-TETA-BCEE i MR-EDA-BCEE. Za karakterizaciju polimera korišćene su diferencijalna termička analiza i infracrvena spektroskopija. Smole su potom testirane na sposobnost da ekstrahuju jone olova i litijuma iz vodenih rastvora korišćenjem metode ekstrakcije iz čvrste faze. Analize provodljivosti i atomske apsorpcione spektrometrije pokazale su visoku efikasnost ekstrakcije, u rasponu od 50% do 85% za jone Pb^{2+} i Li^+. Ovi rezultati pokazuju potencijal MR-EDA-BCEE i MR-TETA-BCEE kao efikasnih polimernih sorbenata za sanaciju životne sredine i uklanjanje teških metala iz vode.

Ključne reči: Merifildova smola, etilendiamin (EDA), hlorodietil, ekstrakcija metala.

CI&CEQ

MAHSA MOHAMADIYAN

Department of Textile Engineering, Yazd Branch, Islamic Azad University, Yazd, Iran

.

NOVEL *ACHILLEA WILHELMSII* C.KOCH NANOCOMPOSITE FABRICATION WITH EXTRAORDINARY PHYSICAL AND CHEMICAL PROPERTIES

Highlights

- Influence of *Achillea wilhelmsii* C.Koch on composite properties.
- Enhancing the anti-inflammatory properties of the composite.
- Enhancing the strength and abrasion resistance of the composite.

Abstract

Two techniques, steam extraction and Soxhlet extraction, were utilized to obtain the active components of Achillea wilhelmsii C. Koch (AWC). These active substances were then used to create composite nanofibers using an electrospinning machine. The morphology of the resulting nanocomposite was examined using an FESEM, and the results demonstrated that the electrospinning method and conditions were suitable. Additionally, we investigated and analyzed the anti-inflammatory efficacy of the nanocomposite produced through both methods. Furthermore, we compared and analyzed the strength, abrasion resistance, moisture content, and water supply of the samples we produced according to certain standards. Overall, the nanocomposite derived from AWC exhibited promising properties that could be utilized in various industries.

SCIENTIFIC PAPER

UDC 582.998.1:66.017:66.061.3:537.2

INTRODUCTION

Achillea wilhelmsii C. Koch (AWC) is a fascinating herbaceous perennial that has been used for centuries for its medicinal properties. This plant is native to the Middle East and has been highly valued in traditional medicine for its numerous health benefits. What makes AWC so special is its unique combination of compounds that have been found to possess anti-inflammatory, antioxidant, and antimicrobial properties. These properties make it a valuable herb in treating various ailments and promoting overall well-being. From treating digestive disorders to relieving menstrual cramps, AWC has a wide range of uses. AWC also has ecological advantages. This plant is known to attract pollinators such as bees and butterflies, making it an excellent addition to any garden or natural landscape. Its beautiful flowers, ranging in color from white to pink to yellow, add a touch of vibrancy wherever they bloom [1-3]. Momtaz *et al.* [4] in a study intended to verify whether AWC can improve colitis by mediating inflammatory cytokines. They treated animals with the hydro-alcoholic extract of AWC at different concentrations, and the results show that the extract downregulated pro-inflammatory mediators in the colon tissue.

One of the technologies that has the power to revolutionize various industries, from healthcare to electronics, is nanofiber electrospinning. Electrospinning is a process that uses an electric field to produce polymer fibers. These fibers can be used in tissue engineering, drug delivery systems, filtration, sensors, and so much more. One of the most exciting applications of electrospinning nanofibers is in the field of regenerative medicine. These fibers can be used as scaffolds to support tissue regeneration, helping damaged organs or tissues heal and restore their function. The small diameter of the fibers mimics the natural extracellular matrix, promoting cell adhesion and growth. This could potentially lead to groundbreaking advancements in the treatment of injuries and diseases.

MOHAMADIYAN: NOVEL ACHILLEA WILHELMSII C.KOCH ...

Chem. Ind. Chem. Eng. Q. 32 (1) 59-65 (2026)

This method is used to produce nanocomposites that are also extracted from natural materials [5-15]. For example, in research, Ghiasi *et al.* [16] used this method to extract the effective elements of wheat bran and produce its nanocomposite. They announced that by producing this composite, which of course also contained nanomaterials, they obtained good anti-ultraviolet and anti-bacterial properties. On the other hand, in a study, Zohoori *et al.* [17] used effective materials of palm in combination with carbon mesoporous nanoparticles in the production of a nanocomposite, which was done by the electrospinning method. This research has shown the use of electrospinning in the production of nanocomposites, and its results have indicated the improvement of the properties of this nanocomposite. The other research was done by Asakereh *et al.* [18] who used electrospinning to produce nanocomposites of hazelnut green shell. In this paper, the researchers produced gelatin/hazelnut green shell nanocomposites with special properties (higher strength and Abrasion resistance, anti-inflammatory, and higher moisture content). Many applications of nanocomposites and nanomembranes can improve features, such as hydrophilicity, permeability, salt rejection, antifouling, and stability [19].

EXPERIMENTAL

Materials and devices

The AWC was prepared from Alborz Mountain Company (Persia). Toluene, ethanol, acetic acid, trifluoroacetic acid, and sodium chlorite were purchased from Merck. Soxhlet extractor device model EV6, 230V, 50-60 Hz (Deutschland), Steam Lab Distillation Apparatus Kit (Deschem), and a Euronda ultrasonic bath model Eurosonic 4D, 350 W, 50/60 Hz (Italy) were used. The morphology of nanofibers and nanomaterials was studied using FESEM (Field Emission Scanning Electron Microscope) (MIRA3-TESCAN). A double-head system of a rotary platform was used to investigate the abrasion resistance through ASTM D-3884-09. The tensile strength was determined by a tabletop uniaxial testing apparatus (INSTRON 3345). The viscosity of the cellulose solution was measured using a Brookfield DV3T Rheometer (AMETEK Brookfield) equipped with an SC4-21 spindle, operating at a speed of 60 rpm.

Method

In this paper, two extraction methods (steam method and Soxhlet method) were performed, and their characteristics were compared [16,18]. In the first method (which produced sample A), steam is used to gently extract the volatile compounds from the plant material through steam lab distillation. The steam passes through the plant material, causing the essential oils and other valuable components to be released and carried away in the steam. The steam and volatile compounds are then condensed and collected, resulting in a concentrated extract. This extract contains the potent ingredients of AWC, which can be electrospun in the next step. One of the key benefits of this extraction method is its ability to preserve the natural properties of AWC. Through careful processing and handling, we ensure that the extract retains its original qualities and benefits. This means that when we use products made from this extract, we are experiencing the full power and potency of AWC. In the second method (which produced sample B), the AWC of 10 grams was measured and soaked with distilled water. Milling was carried out to eliminate any wax and pollution. Then scoured with toluene/ethanol (1/2 volume percent) for 8 hours in a Soxhlet extractor apparatus. Then the solution was rested for a day at room temperature. Then, sodium chlorite (with a pH range of 4.5 - 5.5) was added with acetic acid to eliminate the lignin. The solution was neutralized with distilled water and ethanol.

The obtained from both methods was separately dissolved in trifluoroacetic acid and subjected to an ultrasonic bath. Then, the cellulose solution was prepared at a concentration of 7% (w/v) in Schweitzer's reagent to ensure full transparency and reproducibility of our approach, with a viscosity of 800 cP. The measurement of viscosity was conducted at a controlled temperature of 25°C using a temperature-regulated bath to ensure consistency. A sample volume of 10 mL was used, and the viscosity was determined under steady shear flow conditions with a shear rate range of 10-100 s^{-1} to account for potential non-Newtonian behavior. These parameters were selected to ensure accurate and reproducible viscosity measurements, providing reliable data for the study. Afterward, a blunt needle syringe of each solution was set in the electrospinning apparatus, and an electrospun nanocomposite was produced. Table 1 demonstrates the electrospinning conditions.

Table1. Electrospinning conditions.

Feeding rate (mL/h)	Drum speed (rpm)	Collector-needle distance (cm)	Traverse speed (m/min)	Voltage (kV)
0.4	135	15	0.3	20

Eleven male Wistar rats were selected for this study. The animals were obtained from Kerman Shahid Beheshti laboratory and were 8-10 weeks old, weighing between 180-220 g, as recommended for similar in vivo studies. They were housed in standard laboratory conditions with a 24-hour light/dark cycle, maintained at 22 ± 2°C, and had ad libitum access to food and water. Prior to the experiment, all rats were acclimated to their environment for at least one week to minimize stress-related variability [30]. All experiments and tests were conducted following animal welfare laws and ethical guidelines, and ethical approval was obtained from the Kerman Shahid Beheshti Ethics Committee [31]. To induce localized inflammation, carrageenan was injected subcutaneously into the shaved dorsal skin of the rats before applying the composite samples. Carrageenan-induced inflammation is a well-established model for evaluating anti-inflammatory effects, as it mimics acute inflammatory responses by stimulating pro-inflammatory cytokine release.

RESULTS AND DISCUSSION

Morphological analysis

The morphological analysis of electrospinning nanofibers involves a comprehensive investigation into their physical characteristics at the microscopic level. It allows one to study the arrangement and distribution of nanofibers, as well as their size, shape, and surface features. Through advanced imaging techniques like scanning electron microscopy (SEM), high-resolution images can be captured that showcase the intricate details of these fibers. The scanning electron microscopy image of the samples is depicted in Figure 1. The nano composite's diameter, as observed in Figure 1, measures approximately 39 nm. Additionally, Figure 1 reveals that the nanofibers are created via electrospinning. Upon closer examination, it is evident that the thickness of the nanofibers and their beads does not exceed 50nm, which is highly satisfactory. Due to the achieved images, it was concluded that the electrospinning parameters were good because there was no necking in the SEM.

FTIR analysis

The FTIR spectrum of electrospun cellulose/AWC nanofibers exhibits key functional group peaks characteristic of both cellulose and plant-derived bioactive compounds. In Figure 2B (extracted using the Soxhlet method), the broad absorption band around 3300 cm^{-1} corresponds to O-H stretching vibrations, indicative of strong hydrogen bonding within cellulose fibers. The peak at 2900 cm^{-1} represents C-H stretching, typically associated with cellulose backbone structures. A notable peak at 1700 cm^{-1} suggests the presence of carbonyl (C=O) stretching vibrations, which could originate from flavonoids, polyphenols, or other phytochemicals in AWC.

Further, the peaks at 1600 cm^{-1} and 1500 cm^{-1} are attributed to aromatic C=C stretching, confirming the presence of phenolic compounds from AWC. The characteristic cellulose peaks at 1160 cm^{-1} (C-O-C stretching) and 1030 cm^{-1} (C-O stretching) indicate the retention of cellulose's glycosidic structure after electrospinning. These spectral features confirm the successful integration of AWC into the electrospun cellulose nanofibers, suggesting potential antioxidant and antimicrobial properties while maintaining the structural integrity of cellulose.

The first FTIR spectrum of the cellulose/AWC nanocomposite, extracted using the steam method Figure 2A, exhibits similar characteristic peaks but with slight shifts and intensity variations. The O-H stretching peak (3320 cm^{-1}) remains prominent, indicating strong hydrogen bonding in cellulose. The C=O stretching peak (1720 cm^{-1}) is slightly more intense, suggesting a higher presence of carbonyl-containing compounds such as flavonoids and organic acids from AWC. The aromatic C=C (1580 cm^{-1}, 1480 cm^{-1}) and C-O-C (1140 cm^{-1}, 1010 cm^{-1}) peaks confirm the presence of phenolic compounds and cellulose structure, indicating successful integration of plant-derived components into the nanofibers.

When comparing the spectra from the steam and Soxhlet extraction methods, notable differences arise in peak intensities and slight shifts in wavenumbers. The Soxhlet method (previous spectrum) showed a more intense C-O stretching (1030 cm^{-1}) and aromatic C=C peaks (1600 cm^{-1}, 1500 cm^{-1}), suggesting a higher yield of phenolic and aromatic compounds due to the continuous solvent extraction process. In contrast, the steam method (current spectrum) resulted in a stronger C=O peak (1720 cm^{-1}), indicating a greater retention of volatile organic compounds and aldehydes. These variations suggest that Soxhlet extraction may be more effective for isolating polyphenols and flavonoids, while steam extraction better preserves oxygenated compounds, potentially influencing the bioactivity and chemical composition of the final nanocomposite.

Strength and abrasion properties

Fabrics/fibers are subjected to different forces and stressors throughout their longevity. Nanofibers, with their minuscule size and exceptional durability, have become a game-changer in various industries. In this test, a rubbing test of 30 cycles was done, and the discrepancy in sample mass before and after abrasion was studied for each sample. As shown in Table 2, the abrasion resistance of both samples produced from AWC is very good, and even after 30 rubbing cycles, they still show a resistance higher than 90%. By comparing the abrasion resistance of two samples, A and B, it can be seen that there is no significant difference between these two samples, and therefore, it can be said that the abrasion resistance of both samples is almost the same. It is worth mentioning that the abrasion resistance of both produced samples is much higher compared to other similar cellulosic fibers [20], and it can be concluded that the use of AWC in the production of nanofibers can lead to the production of fibers with high abrasion resistance.

On the other hand, to investigate the strength of the samples, the produced nanofibers were subjected to tension. The results showed that the strength of both produced samples was very high and, of course, almost the same, although the strength of these nanofibers is much higher compared to cellulose nanofibers [21]. The strength of these nanofibers can be attributed to their unique molecular structure and composition. The fibers are composed of long chains of organic molecules that are tightly packed together, creating a dense and strong material. This molecular arrangement allows the nanofiber to withstand high levels of stress and strain without breaking or deforming. Furthermore, the nanofibers' abrasion resistance is also remarkable. Abrasion resistance refers to the ability of a material to resist wear and tear caused by friction. In the case of AWC nanofiber, its high abrasion resistance can be attributed to several factors. Firstly, the dense molecular packing provides a strong barrier against external forces that could cause abrasion. Additionally, the nanofiber's surface is smooth and free from irregularities, reducing friction and minimizing the likelihood of abrasion. The reason behind the strength and abrasion resistance of AWC nanofiber can also be

linked to its natural properties. AWC is a plant that grows in harsh environments, such as arid regions. To survive in these conditions, the plant has developed mechanisms to protect itself from external stressors. These mechanisms translate into the nanofiber's exceptional strength and durability. Moreover, the presence of certain compounds
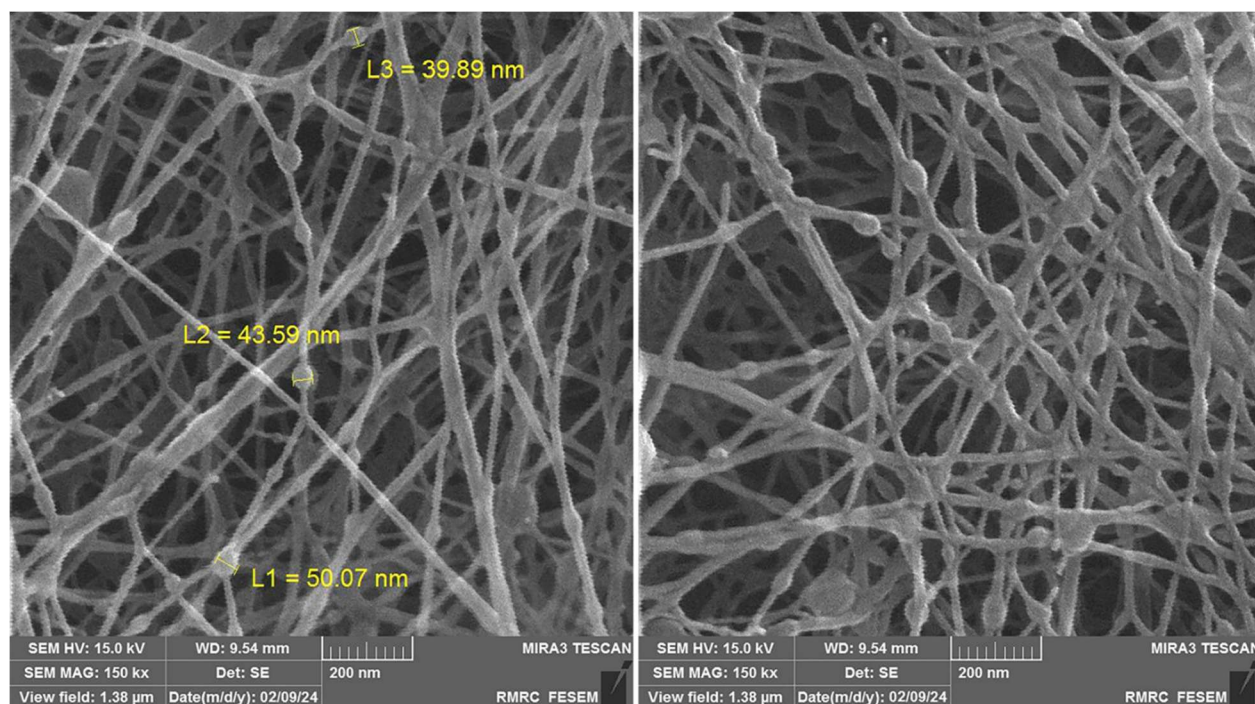

Figure 1. SEM of samples (right: sample A, left: sample B).
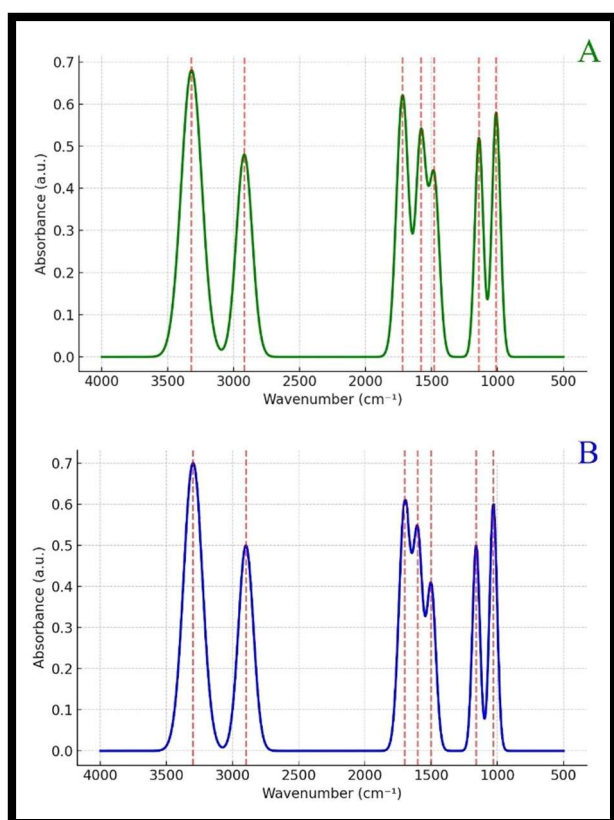

Figure 2. FTIR spectra of electrospun cellulose/AWC nanofibers extracted by A) the steam and B) Soxhlet method.

within the AWC nanofiber may contribute to its strength and abrasion resistance. These compounds could include lignin, cellulose, and other organic substances that enhance the material's mechanical properties. The combination of natural adaptations and chemical composition makes AWC nanofibers a robust and resilient material. In conclusion, the strength and abrasion resistance of AWC nanofibers can be attributed to their unique molecular structure, smooth surface, natural adaptations, and chemical composition.

Anti-inflammatory analysis

Inflammation is a natural response of the immune system to injury or infection, but when it becomes chronic, it can lead to a range of diseases, including arthritis, asthma, and inflammatory bowel disease[22-24]. This test was done based on the Winter technique [25], and this reference would validate the use of carrageenan in measuring the anti-inflammatory properties of AWC nanofibers and ensure methodological transparency. Carrageenan-induced paw edema is a gold-standard model for studying acute inflammation in rodents, as it closely mimics the early phases of inflammation seen in human conditions [32]. A digital caliper was used to measure the diameter of the hind paw, before and after injection of carrageenan. This calculation was repeated every 30 minutes for 5 hours. The results shown in the edema diagram (Figure 3) indicated that the edema reduction of samples A and B was clearly visible after 60 minutes, while this property is present in the control sample from the very beginning, and after about 240 minutes, the effects of samples A and B and the control sample were very close to each other. This is while sample A reached its

best effect earlier than the control sample, i.e., after 210 minutes (the control sample reached this point after 240 minutes). To further clarify the use of indomethacin as a control, it is important to highlight that indomethacin is a well-established nonsteroidal anti-inflammatory drug (NSAID) that functions by inhibiting the cyclooxygenase (COX) enzymes, primarily COX-1 and COX-2. These enzymes play a key role in the synthesis of prostaglandins, which are mediators of inflammation and pain. Indomethacin is widely used as a positive control in anti-inflammatory studies due to its well-documented efficacy in reducing edema and inflammatory responses in various animal models, including carrageenan-induced inflammation. By comparing samples A and B, it was concluded that both samples had a relatively similar effect and both samples worked the same, but sample A worked a little better than sample B.

This study has demonstrated that AWC nanofibers can effectively suppress the production of pro-inflammatory molecules, such as cytokines and chemokines. These molecules play a key role in the inflammatory process by recruiting immune cells to the site of inflammation and promoting tissue damage. By inhibiting their production, AWC nanofibers help alleviate inflammation and reduce associated symptoms. The anti-inflammatory effects of AWC nanofibers are attributed to the presence of bioactive compounds, such as flavonoids and terpenoids, which have been shown to possess anti-inflammatory activity. These compounds modulate the activity of inflammatory mediators and enzymes, suppressing the inflammatory response and promoting tissue repair.

Table2. Abrasion resistance and tensile strength of samples.

Sample	Fabric weight before abrasion (g)	Fabric weight after abrasion (g)	Abrasion resistance (%)	Tensile strength (MPa)
Raw			~84	~0.694
A	5.634	5.147	91.35	1.365
B	5.496	4.991	90.81	1.374

Moisture Content and Water Supply

Proper hydration is essential for maintaining healthy skin. When the skin becomes dehydrated, it can lead to dryness, flakiness, and a compromised skin barrier. This not only affects the appearance of the skin but also increases the risk of various skin conditions, such as eczema and dermatitis [26-29]. The moisture content and water supply of the produced nanocomposites were investigated and measured through the AATCC-20A standard, as Eq.(1), where W_h is the weight of the composites after being exposed to moisture and W_s is the weight of the samples after dehumidification.

$$TH\,(\%) = \frac{W_h - W_s}{W_s} \times 100 \tag{1}$$

Both samples A and B were subjected to this test five times each (due to the elimination of laboratory error), and the average data indicates that the moisture content of samples A and B is very close to each other, 18.65% and 18.48%, respectively. This difference is small and negligible. Therefore, it can be said that the wettability of both produced composites is similar. Meanwhile, according to previous research [17], the moisture content of the

cellulose sample (which is cellulosic and the same as these two samples) is about 11%. AWC nanofibers offer strong water supply benefits, making them an excellent choice for individuals looking to improve skin hydration. The nanofiber structure of AWC allows for the retention of a high amount of water, creating a moist environment that helps prevent transepidermal water loss. In addition to their water retention properties, AWC nanofibers also promote the absorption of moisture from the environment. This means that even in dry conditions, the nanofibers can continuously supply water to the skin, ensuring optimal hydration levels.
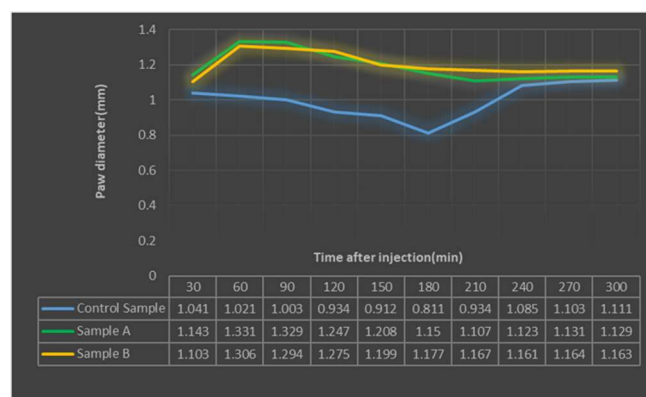

	30	60	90	120	150	180	210	240	270	300
Control Sample	1.041	1.021	1.003	0.934	0.912	0.811	0.934	1.085	1.103	1.111
Sample A	1.143	1.331	1.329	1.247	1.208	1.15	1.107	1.123	1.131	1.129
Sample B	1.103	1.306	1.294	1.275	1.199	1.177	1.167	1.161	1.164	1.163

Figure3. Inflammatory diagram of samples.

CONCLUSION

The findings presented in this study indicate that both Soxhlet extraction and steam extraction of AWC yield similar outcomes in terms of the final properties of the nanocomposite fiber. However, the steam method appears to have a slight advantage. The interaction between bioactive compounds, such as terpenoids and flavonoids, with skin cells leads to an increase in the anti-inflammatory properties of the samples. These compounds, including lignin, cellulose, and other organic substances, enhance the strength and abrasion resistance of the produced samples, contributing to their mechanical properties. On the other hand, the moisture content and water absorption of the produced nanocomposite are higher compared to other cellulosic materials. Overall, while the effects of Soxhlet and steam extraction are similar, the steam method shows slightly better results. In this particular case, the research not only provides valuable data and insights into the nanocomposite production sector but also advances our understanding of how various methods can fundamentally change the properties of composite textiles. This contribution is essential for the industry as it helps propel advancements in the field of composite material production.

Acknowledgment

REFERENCES

[1] M. Amiri, J. Navabi, Y. Shokoohinia, F. Heydarpour, G. Bahrami, L. Behbood, P. Derakhshandeh, S. Momtaz, M.H. Farzaei, Complementar. Ther. Med.

45 (2019) 262-268.
https://doi.org/10.1016/j.ctim.2019.05.001.

[2] E. Khazneh, P. Hřibová, J. Hošek, P. Suchý, P. Kollár, G. Pražanová, J. Muselík, Z. Hanaková, J. Václavík, M. Miłek, J. Legáth, K. Šmejkal, Molecules. 21 (2016) 404-421. https://doi.org/10.3390/molecules21040404.

[3] A. Dadkhah, F. Fatemi, S. Ababzadeh, K. Roshanaei, M. Alipour, B.S. Tabrizi, Bot. Stud. 55 (2014) 37-46. https://doi.org/10.1186/1999-3110-55-37.

[4] S. Momtaz, M.A. Azimian, P. Gharazi, M. Dehnamaki, Z. Rezaei, M. Rahimifard, M. Baeeri, A.R. Abdollahi, M. Abdollahi, M.H. Farzaei, A.H. Abdolghaffari, Proc. Natl. Acad. Sci., India, Sect. B. 93 (2023) 127-135. https://doi.org/10.1007/s40011-022-01404-9.

[5] M. Mirjalili, S. Zohoori, J. Nanostruct. Chem. 6 (2016) 207-213. https://doi.org/10.1007/s40097-016-0189-y.

[6] S. Zohoori, M. Latifi, A. Davodiroknabadi, M. Mirjalili, Pol. J. Chem. Technol. 19 (2017) 56-60. https://doi.org/10.1515/pjct-2017-0049.

[7] P.E. Oliveira, X. Petit-Breuilh, P.E. Díaz, W. Gacitúa, Nano-Struct. Nano-Objects. 23 (2020) 100525-100532. https://doi.org/10.1016/j.nanoso.2020.100525.

[8] G.A. Kaur, M. Shandilya, P. Rana, S. Thakur, P. Uniyal, Nano-Struct. Nano-Objects. 22 (2020) 100428-100436. https://doi.org/10.1016/j.nanoso.2020.100428.

[9] M.S. Hossain, K. Takahashi, A. Ohgoshi, K. Nakane, J. Mater. Sci. 58 (2023) 16669-16679. https://doi.org/10.1007/s10853-023-08980-9.

[10] Y. Guo, X. Wang, Y. Shen, K. Dong, L. Shen, A. Alzalab, J. Mater. Sci. 57 (2022) 58-104. https://doi.org/10.1007/s10853-021-06575-w.

[11] P. Kianfar, A. Bakry, S. Dalle Vacche, R. Bongiovanni, A. Vitale, J. Mater. Sci. 59 (2024) 3711-3724. https://doi.org/10.1007/s10853-024-09416-8.

[12] A. Al-Attabi, M.A. Abdulhadi, L.R. Al-Ameer, M.D.N. Hussein, S.J. Abdulameer, R.S. Zabibah, A. Fadhil, Int. J. Mater. Res. 115 (2024) 162-178. https://doi.org/doi:10.1515/ijmr-2023-0125.

[13] V. Şimşek, M.O. Çağlayan, Int. J. Mater. Res. 114 (2023) 1047-1.057. https://doi.org/doi:10.1515/ijmr-2022-0491.

[14] A. Momeni, A. Ghadi, R. Fazaeli, M. Khavarpour, Int. J. Mater. Res. 114 (2023) 753-764. https://doi.org/doi:10.1515/ijmr-2021-8516.

[15] T.G. Arul, V. Perumal, R. Thanigaivelan, Chem. Ind. Chem. Eng. Q. 28 (2022) 247-253. https://doi.org/10.2298/ciceq210501036a.

[16] Y. Ghiasi, A. Davodiroknabadi, S. Zohoori, Bull. Mater. Sci. 44, (2021) 89-94. https://doi.org/10.1007/s12034-021-02406-5.

[17] S. Zohoori, S. Shahsavari, M. Sabzali, S.A. Hosseini, R. Talebikatieklahijany, Z. Morshedzadeh, J. Nat.

[18] M. Asakereh, S. Zohoori, F. Mohammadisaghand, M. Sabzali, R. Mohammadisaghand, B. Soltani, J. Nat. Fibers. 19 (2022) 15552-15562. https://doi.org/10.1080/15440478.2022.2131024.

[19] M. Alghamdi, A. El-Zahhar, Chem. Ind. Chem. Eng. Q. 27 (2021) 35-44. https://doi.org/10.2298/ciceq200128022a.

[20] N. Kooshamoghadam, S. Zohoori, M. Bekrani, S. Shahsavari, R. Talebikatieklahijany, J. Nat. Fibers. 19 (2022) 4846-4853. https://doi.org/10.1080/15440478.2020.1870631.

[21] R. Mohammadisaghand, S. Zohoori, A. Shahbeigihassanabadi, F. Mohammadisaghand, F. Mousavi, V. Shorabi, J. Nat. Fibers. 20 (2023) 2152150-2152157. https://doi.org/10.1080/15440478.2022.2152150.

[22] H. Liu, B. Sun, Z. Tang, S. Qian, S. Zheng, Q. Wang, Y. Shao, J. Chen, J. Yang, Y. Ding, H. Zhang, IJC. Heart. Vasculature, 50 (2024) 101341-101350. https://doi.org/10.1016/j.ijcha.2024.101341.

[23] S. Saibeni, M. Zanetti, C. Bezzio, L. Pironi, A. Armuzzi, S. Riso, F. Caprioli, A. Lezo, F.S. Macaluso, D. Pugliese, M. Daperno, G.M. Giorgetti, Dig. Liver Dis. 55 (2023) 1028-2033. https://doi.org/10.1016/j.dld.2023.05.029.

[24] N. Moradi, G. Soufi, A. Kabir, M. Karimi, H. Bagheri, Anal. Chim. Acta. 1270 (2023) 341461-341465. https://doi.org/10.1016/j.aca.2023.341461.

[25] C.A. Winter, E.A. Risley, G.W. Nuss, Proc. Soc. Exp. Biol. Med. 111 (1962) 544-547. https://doi.org/10.3181/00379727-111-27849.

[26] L. Eggink, J. K.Hoober, JID Innovations. 2 (2022) 100142-100152. https://doi.org/10.1016/j.xjidi.2022.100142.

[27] G. Eichner, S.L. Vieira, C.A. Torres, J.L.B. Coneglian, D.M. Freitas, O.A. Oyarzabal, J. Appl. Poult. Res. 16 (2007) 344-350. https://doi.org/10.1093/japr/16.3.344.

[28] N. Tamai, M. Horii, K. Takehara, S. Kato, Y. Yamamoto, A. Naito, M. Tayama, Y. Tamahashi, S. Nakamura, T. Kadono, M. Oe, T. Nagase, H. Sanada, Eur. J. Oncol. Nurs. 17 (2013) 673-680. https://doi.org/10.1016/j.ejon.2013.05.005.

[29] E.M. Shepherd, B.D. Fairchild, C.W. Ritz, J. Appl. Poult. Res. 26 (2017) 518-528. https://doi.org/10.3382/japr/pfx024.

[30] A. Ghasemi, S. Jeddi, K.Kashfi, EXCLI. J. 20 (2021) 1431-1445. https://doi:10.17179/excli2021-4072.

[31] M. Ghasemi, A. Dehpour, J. Med. Ethics. Hist. Med. 2 (2009)

[32] S. Zohoori, N. Torabi, E. Gholami, F. Rastgoo, M. Rad, R. Pourheidari, Discover Mater. 4 (2024). https://doi.org/10.1007/s43939-024-00164-9.

MAHSA MOHAMADIYAN

Department of Textile Engineering, Yazd Branch, Islamic Azad University, Yazd, Iran.

NAUČNI RAD

IZRADA NOVOG NANOKOMPOZITA NA BAZI AKTIVNIH KOMPONENTI *ACHILLEA WILHELMSII* C. KOCH SA IZVANREDNIM FIZIČKIM I HEMIJSKIM SVOJSTVIMA

Dve tehnike, ekstrakcija parom i Soksletova ekstrakcija, korišćene su za dobijanje aktivnih komponenti Achillea wilhelmsii C. Koch (AWC). Ove aktivne supstance su zatim korišćene za dobijanje kompozitnih nanovlakana pomoću mašine za elektropredenje. Morfologija dobijenog nanokompozita je ispitana pomoću FESEM-a, a rezultati su pokazali da su metoda i uslovi elektropredenja bili pogodni. Pored toga, istraživana je antiinflamatorna efikasnost nanokompozita proizvedenog pomoću obe metode. Štaviše, uporedili smo i analizirali čvrstoću, otpornost na habanje, sadržaj vlage i snabdevanje vodom uzoraka koje smo proizveli prema određenim standardima. Generalno, nanokompozit dobijen iz AWC-a pokazao je obećavajuća svojstva koja se mogu koristiti u različitim industrijama.

Ključne reči: Achillea wilhelmsii C. Koch, kompozit, nanovlakna, antiinflamatorno, otpornost na habanje.

65

AMANDA ZVIUYA[1]

JOSEPH GOVHA[1]

PLACXEDES SIGAUKE[2],

TIRIVAVIRI A. MAMVURA[2],

GWIRANAI DANHA[2]

[1]Department of Chemical and Process Systems Engineering, Harare Institute of Technology, Belvedere, Harare, Zimbabwe.

[2]Department of Chemical, Materials and Metallurgical Engineering, Faculty of Engineering and Technology, Botswana International University of Science and Technology, Palapye, Botswana

POTENTIAL APPLICATION AS A BIO-COAGULANT FOR *MORINGA OLEIFERA* SEEDS

Highlights

- The protein in moringa seeds can potentially be used as a bio-coagulant.
- The optimum temperature for drying the moringa seeds was 100 °C for 30 min.
- The highest oil yield (31%) was obtained from n-hexane compared to ethanol yield (28.1%).
- The highest turbidity removal efficiency of 93.6% was at low dosages of 40 mg/L.
- High turbidity removal of 88.6% was obtained at an optimum pH of 6.1.

Abstract

In the current trend, industries prefer to optimize machining processes using finite This study focused on producing a natural bio-coagulant from moringa seeds. Moringa seed extract is a natural coagulant for the treatment of water containing suspended solids and colloids and is obtained through grinding, oil extraction, protein extraction from the solids using a 2 M NaCl solution, protein separation by centrifugation, followed by filtration. This study investigated the production and use of bio-coagulants. Parameters investigated when producing the bio-coagulant include the effects of temperature on the removal of moisture content in the moringa seeds, the type of solvent on the oil yield, and varying the volume of n-hexane for oil extraction. Parameters investigated when using the bio-coagulant include the effect of dosage of bio-coagulant on pH and turbidity removal efficiency, and the performance of the bio-coagulant at low, medium, and high turbidity levels. The optimum temperature and time obtained by drying the moringa seeds were 100 ºC and 30 min, and the highest oil yield obtained was 31% when using n-hexane as the solvent. Turbidity removal efficiency went up to 96.4% when using 50 mg/L of the bio-coagulant at a pH of 6.1. High turbidity removal was achieved at low bio-coagulant dosages, which was regarded as a breakthrough finding for this research.

Keywords: Moringa oleifera seeds, n-hexane, bio-coagulant, water treatment.

INTRODUCTION

Water availability for all is the ultimate realization of Sustainable Development Goal Number 6, which thrusts upon member states the obligation to ensure availability and sustainable management of water by at least decreasing the number of people lacking access to safe potable water by half [1]. Before water is distributed to consumers, conventional methods, such as coagulation, flocculation, adsorption, and activated sludge, are applied for water and wastewater treatment [2,3]. In addition, there is a high demand for using efficient and inexpensive methods from biomaterials, like biosorption and adsorption, and this is giving rise to the use of inexpensive biosorbents to reduce costs [1,4,5]. Despite the remarkable role of chemical and synthetic coagulants in water purification, they are associated with carcinogenic and neurotoxic effects due to their residues in treated water, such as aluminum [1,3,6]. The development of sustainable and eco-

friendly coagulants as an alternative to chemical coagulants have been reported [7]. The presence of numerous bioactive compounds has associated the Moringa (*Moringa oleifera*) plant with multiple nutritional and health benefits [1,2,8]. Unwanted particles from wastewater can be separated by the seed extract [6]. Over 90% of bacteria can be sedimented from raw water by using the unprocessed seed powder, thus they can be potentially used as an antimicrobial treatment. The seed extract acts as a coagulant and flocculent to clarify turbid water. Moringa seed extract destabilizes colloidal particles and thus has a good potential to lower the *E. coli* count [8], and *M. oleifera* has been used to treat wastewater from paper mills [6]. Therefore, this project focuses on the coagulation potential of *M. oleifera* seed extract in the treatment of water.

Coagulants used in water and wastewater treatment

Coagulants are either natural or inorganic. Natural coagulants are economical since a variety of users can use them at lower dosages without losing their efficacy, and they require far less sludge to be disposed of, which further lowers expenses [4,8]. Low-turbidity raw water can be effectively treated with inorganic coagulants that are primarily based on aluminum or iron. Examples include polyaluminum chloride (PAC), sodium aluminate, aluminum sulfate (Alum), ferric sulfate, and ferric chloride [2,3].

Aluminum-based coagulants are primarily used in water and wastewater treatment to: (i) remove heavy metals like cadmium (Cd), lead (Pb), arsenic (As), and iron (Fe), (ii) remove phosphorus (chemical precipitation), (iii) remove chemical and biological oxygen demands (COD) and BOD, (iv) remove color pigments, and (v) for sludge conditioning and dewatering [9]. When using inorganic coagulants, a larger dosage is needed to cause coagulation, and a lot of sludge containing dangerous chemicals is produced as a result [2].

M. oleifera

A perennial woody plant of the Moringa family, *M. oleifera* is indigenous to tropical and southern subtropical areas that are semiarid or arid [10]. The robust and swiftly expanding *M. oleifera* Lamarck (family *Moringaceae*) tree is extensively grown because of its great degree of environmental adaptability [11]. It is regarded as one of the world's most useful plants because practically every part of it can be used for industrial, traditional medicinal, and food purposes [12] and is known to be drought-resistant [13]. Many countries that are tropical or subtropical grow a lot of *M. oleifera* because practically every part of the plant can be used for food or other purposes, as it is highly valued [14].

Moringa plant is classified as an organic coagulant (bio-coagulant), and it has a variety of bioactive chemicals, from tree seeds, leaves, roots, and flowers [15], which have been linked to several health and nutritional advantages [1,8,9]. The polyphenol content of *M. oleifera* from different regions indicates high genetic diversity, likely due to differences in cultivation conditions, climate, or soil environment, resulting in the accumulation of various polyphenols and enhanced drought resistance [16]. Moreover, *M. oleifera* seeds have drawn interest due to their high turbidity removal efficiency, affordability, and low toxicity, as well as the possibility of on-site preparation [17]. Studies on seeds are focused on the purification of water and oil extraction [18]. Research has demonstrated that powdered *M. oleifera* seeds are a cost-effective, low-impact, and sustainable substitute for costly conventional chemicals [19], economical, producing less pH and biodegradability [20], low toxicity, and high cost-efficiency [9], and eliminate dangerous bacteria from water bodies [21]. In Zimbabwe, the *M. oleifera* tree grows quickly and is commonly grown, especially in tropical areas like the Binga district. In addition to producing proteins that function as efficient coagulants in the treatment of water and wastewater, moringa seeds have high-quality edible oil content–up to 40% by weight [1]. The seed extract can separate unwanted particles from wastewater, sedimenting impurities [3,9]. The raw seed powder can filter out over 90% of microorganisms from raw water, making it a viable antimicrobial treatment [8]. To clear turbid water, the seed extract works as a flocculent and coagulant [3,4,9].

Ajav and Fakayode [22] aimed to ascertain the physical characteristics of moringa seeds with respect to an oil expeller's design. Oloyede *et al.* [23] identified the engineering characteristics of moringa seeds and pods that are important for designing a moringa sheller. Arreola *et al.* [24] aimed to identify the characteristics of the coagulating proteins. Barakat and Ghazal [11] identified the physicochemical characteristics of *M. oleifera* seeds grown in various Egyptian regions. Nwaiwu and Bello [19] determined the optimum combination for *M. oleifera* and Alum, Adejumo [21] examined a few of the *M. oleifera* seeds' physical characteristics at different moisture contents. Du *et al.* [25] investigated the effects of different NaCl concentrations, and Madrona *et al.* [26] used electrophoresis to determine the protein's molecular weight in the *M. oleifera* seed. This study aimed to evaluate the efficiency of *M. oleifera* seed extract for water treatment. This investigation aimed to separate the proteins from moringa seeds into a biocoagulant and ascertain the ideal timing and temperature for drying the moringa seeds, conduct seed oil extraction, and determine the efficiency of turbidity removal in conditions of low turbidity, medium turbidity, and high turbidity using canteen and laundry wastewater.

MATERIALS AND METHODS

Materials

The wastewater samples used for testing the bio-coagulant were collected from Harare Institute of Technology's municipal water, laundry, and canteen water and were characterized according to the Environment Management Act (Effluents and Solid Waste Disposal) S1 6 of 2007. Moringa seeds (shelled) used were sourced locally in Zimbabwe, and it was utilized as the primary ingredient in the study (Figure 1).

Experimental method

The study was carried out at the Harare Institute of Technology, Zimbabwe. The raw material used was moringa seeds, and the bio-coagulant extract can be obtained through processes of washing, drying, grinding and drying, oil extraction, protein extraction, centrifugation, and filtration. The methodology (Figure 2) is similar to the one adapted from [2,8,9].

Drying and grinding

The moringa seeds were dried at 100 °C for 20 min and then ground using a mortar and pestle until a fine powder was obtained. The moisture content can be determined as:

$$Moisture\ content = \frac{difference\ in\ weigh\ of\ seeds}{weigh\ of\ seeds\ before\ drying} \times 100\% \quad (1)$$

Oil extraction

The solvent used for oil extraction was n-hexane with a ratio of moringa solids to hexane of 1:5 w/v for 24 h. The oil was separated by precipitation and then filtration.

Protein extraction and centrifugation

The protein in moringa seeds was extracted with a 2 M NaCl solution. The solid residue was removed by filtration, and the remaining supernatant was centrifuged at 4000 rpm for 30 min to remove the sediment and leave the moringa liquid extract. NaCl present in the *M. oleifera* solution improves coagulation efficiency because it helps to release the coagulant protein fraction present in the solution. Moreover, the coagulation process enhances this extraction by about 7 times higher than that extracted by distilled water [6].

Coagulation tests

To determine optimum turbidity removal percentages and dosage, standard sedimentation jar test equipment was used in this study, which comprised six 1000 mL jars that can simultaneously test each sample [5]. The procedure involved using a 1000 mL graduate and pouring the necessary amount of well-mixed raw water into one of the transparent jars. Afterwards, identical paddles were placed in each beaker, followed by setting the filled jars on the gang stirrer. For 30 seconds, beakers were agitated at 40 to 50 rpm until all dosages of the bio-coagulant had been added. For 30 seconds, the mixing was accelerated to 100-125 rpm, and then the mixing speed was reduced to 40 rpm for 60 seconds. The mixer was turned off for the mixture to settle. After 15 minutes of settling (sample point height of 23 cm), the relative speeds of settling and the appearance of the supernatant were noted, whereby the water's initial turbidity sample determined the settling rate with *M. oleifera* seed. Afterward, turbidity and/or absorption measurement of each sample was performed in triplicate, and turbidity was measured using a hand-held turbidimeter with an accuracy of ± 2%.

Coagulation efficiency

The efficiency of using MO as a bio-coagulant was calculated using turbidity by the following expression:

$$Turbidity\ removal =$$
$$\frac{Turbidity_{before/raw} - Turbidity_{after/treated}}{Turbidity_{before/raw}} = 100\% \quad (2)$$
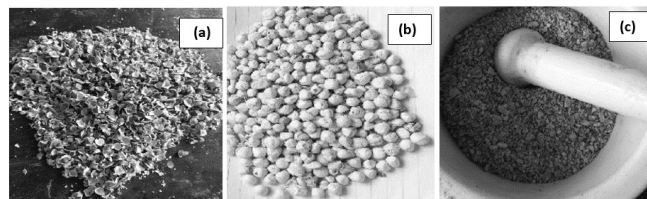

Figure 1. (a) Moringa shells, (b) seeds, and (c) ground seeds.

RESULTS AND DISCUSSION

Wastewater characterization

Table 1 shows the characterization results of a sample of wastewater for turbidity, oxygen absorbed, total dissolved solids, dissolved oxygen, and total suspended solids as 80.20 NTU, 90 mg/L, 1722 mg/L, 36.8 saturation%, and 114 mg/L, respectively. Higher collision frequencies, greater van der Waals attractions, and quicker aggregation make coagulation frequently more effective in high-turbidity water than in low-turbidity water. Total suspended solids can include harmful substances and cause turbidity, which reduces the amount of sunlight that reaches the water.

Production of bio-coagulant

Drying of moringa seeds for moisture removal

The mass change was monitored as the temperature was changed, and the results are shown in Figure 3. The mass of moringa seeds decreased rapidly with an increase in temperature from 100 °C to 120 °C hence, this meant that the moisture content in the seeds was removed. The moringa seeds' moisture content was determined as 6.8%. 7.31% moisture content on a wet basis [22], 6.3% moisture content on a dry basis [23], and 4.74% moisture content was found in the literature [27]. Moisture content has a huge effect on the storage life of the seeds, as the physical characteristics of the seed, such as its width, length, geometric mean diameter, thickness, surface area, sphericity, angle of repose, true density, and coefficient of friction, are influenced by its moisture content. These properties are crucial information for designing effective processes and equipment [21] as well as forecasting the stability and safety of seeds in terms of microbial growth based on moisture content. Therefore, it is important to note the moisture content in order to predict a reasonable possible life storage of each accession.

Effect of the type of solvent on oil extraction from moringa seeds

The oil in moringa seeds is highly soluble in n-hexane compared to other solvents such as ethanol. From the results, the oil yield obtained from hexane is 31 ± 0.06%, slightly higher than that of ethanol (28.1%). In another study, petroleum ether was determined as the best solvent (33.9%), followed by *n*-hexane at 27.1% [2]. With methanol, a 26.3% extraction was achieved.

Effects of varying volumes of n-hexane on oil extraction

n-Hexane was used to extract the oil. The effect of changing its volume was investigated at a constant moringa seed powder mass to determine the ratio of seed solid to *n*-hexane to be used. The results for the change of *n*-hexane against the amount of oil extracted are presented in Figure 4. As the volume of *n*-hexane increased, the amount of oil extracted also increased, as seen by the mass of oil extracted. Change in mass of oil extracted increased slowly after 450 mL, giving a ratio of seed to *n*-hexane of 1:5 w/v.

Validation of bio-coagulant

Effect of bio-coagulant dosage on turbidity reduction efficiency

The effects of bio-coagulant dosage on turbidity reduction efficiency can be seen in Table 2 and Figure 5a. From Figure 5a, the turbidity removal percentage increased from a dosage of 20 mg/L to 50 mg/L and then decreased slightly from 60 mg/L and 80 mg/L, where the graph plateaus. The optimum dosage is determined as 50 mg/L (turbidity removal percentage 96.4%). When the *M. oleifera* dosage goes above the optimum of 50 mg/L, the turbidity removal efficiency decreases. This is attributed to the increased turbidity because of the neutralization and precipitation of all colloids with an optimum dosage; therefore, water turbidity is brought on by the excess coagulants as they did not interact with colloidal particles, which are oppositely charged [6]. *M. oleifera* was used to treat paper mill effluent at different coagulant dosage rates (50-300 mg/L). The optimum dosage rate of 150 mg/L was determined when it had a turbidity removal efficiency of 96% [6]. *M. oleifera* was also used to treat synthetic water, and high residual nephelometric turbidity units (NTU) were determined at lower dosages (0-10 ml/L) of *M. oleifera* [2]. This was in contrast to the results of the present study.

M. oleifera and Alum were used to treat two different natural waters (Santa Helena brook and Picacha brook) at different concentrations (mg/L) [5]. The performance for the Santa Helena brook natural water was: highest turbidity removal of 90% at three different concentrations of 63, 94, and 125 mg/L for *M. oleifera* and the lowest dosage rate of 63 mg/L was taken as the optimum in this instance, and this was slightly higher than what was determined in this study. Of note is that *M. oleifera* performed better than Alum in this study, as the highest turbidity removal for Alum was 80% at an 18.8 mg/L dosage rate. The performance for the Picacha brook natural water was: highest turbidity removal of 100% at five different concentrations of 250, 281, 312, 344, and 375 mg/L for *M. oleifera,* where the lowest dosage rate of 250 mg/L was taken as the optimum in this instance. This was higher than what was determined in this study. Of note is that *M. oleifera* performed similarly to Alum in this study, as the highest turbidity removal for Alum was also 100% at 219, 250, and 281 mg/L dosage rates. *M. oleifera* was investigated as a bio-coagulant on synthetic water at different dosages from 0 to 200 mg/L [10]. They determined that the highest turbidity removal of 79% was reached at 50 mg/L, just as in the present study.

The native protein responsible for coagulation is a 13 kDa dimeric protein with roughly 6.5 kDa subunits [2]. According to Arreola *et al.* [24], proteins with molecular weights ranging from 6 to 5 kDa form the active agents of M. oleifera salt solutions, which combine to form a heterodimer with a molecular weight of 11-12 kDa. The presence of polar amino acids with both positive and negative charges in large quantities in moringa seed extracts causes the rupture brought on by the effect of salt, which permits a greater number of radical groups to exist in the product. As a result, brine solutions become more efficient in the coagulation process by encouraging the creation of chemical bridges and adsorption between the coagulant and colloidal materials.

According to the literature, protein extraction increased significantly starting at 0.25 M of salt concentration; after that, there was no discernible change in extractability. After the salt concentration reached 2.0 M, extractability rose. Additional salt concentration (>2.0 M) had a negative impact on protein extraction. Significant changes were observed in the protein extractability upon additional elevation of the salt concentration [28].

A greater concentration of NaCl during extraction was beneficial for low molecular weight *M. oleifera* salt-soluble protein [25]. Small proteins have a coagulating mechanism whereby their positive charge binds to the surface of negatively charged particles. This causes particles with distinct charge zones to form, and as a result of their collisions, the formation of follicles is encouraged [24]. Adsorption and charge neutralization are the main mechanisms of the coagulation with moringa. Studies show the protein content of *M. oleifera* is 26.7% [29], 28% [30], 37.2% [31], 33.53% [12], and 40.34% [10]. Proteins combine with other substances, thus forming sediments. As the dosage of bio-coagulant is increased, the settling velocity will also increase because the number of polypeptides that can bind the floc will increase with an increase in dosage, speeding up the settling process [32].

Effect of bio-coagulant dosage on pH

The effects of bio-coagulant dosage on pH can be seen in Figure 5b. From Figure 5b, the highest turbidity removal of 96% was at pH 4.5, while the least turbidity removal of 75% was at pH 6.2. Based on the experiments, the optimum pH obtained using moringa bio-coagulant is 6.1 with 89% turbidity removal efficiency. It lies within the WHO (2006) recommended pH range for water, which is between 6.0 and 8.0. However, a pH of 4.4 can be used to remove the turbidity and adjust the pH afterward. This will help to remove additional turbidity up to 96%. *M. oleifera* was used to treat paper mill effluent at different pH values (4-9), and the optimum pH range was determined to be 6-8 [6]. The results from the present study fell within the same range. The turbidity removal drastically dropped from a pH higher than 6.0 due to alkaline conditions, causing a decrease in protein stability [33].

Effect of different turbidity levels

The bio-coagulant was tested in water at different turbidity levels: low (5 NTU), medium (15 NTU), and high (40 NTU). The results are summarised in Figure 5c. *M.*

oleifera bio-coagulant was found to be more effective in water of high turbidity. This is due to more frequent contact of the ions in the bio-coagulant, which form heavy flocs, hence providing high efficiency. The results can be seen in Figure 5c. *M. oleifera* was investigated as a bio-coagulant on synthetic water at different dosages from 0 to 200 mg/L

from an initial turbidity of 25 NTU, and the highest turbidity removal of ~79% was reached at 50 mg/L [10]. The synthetic waters used in the study had higher turbidity, showing similar results to the present study. The *M. oleifera* dose can handle higher turbidity, as is in this study, and still achieves good removal efficiencies.
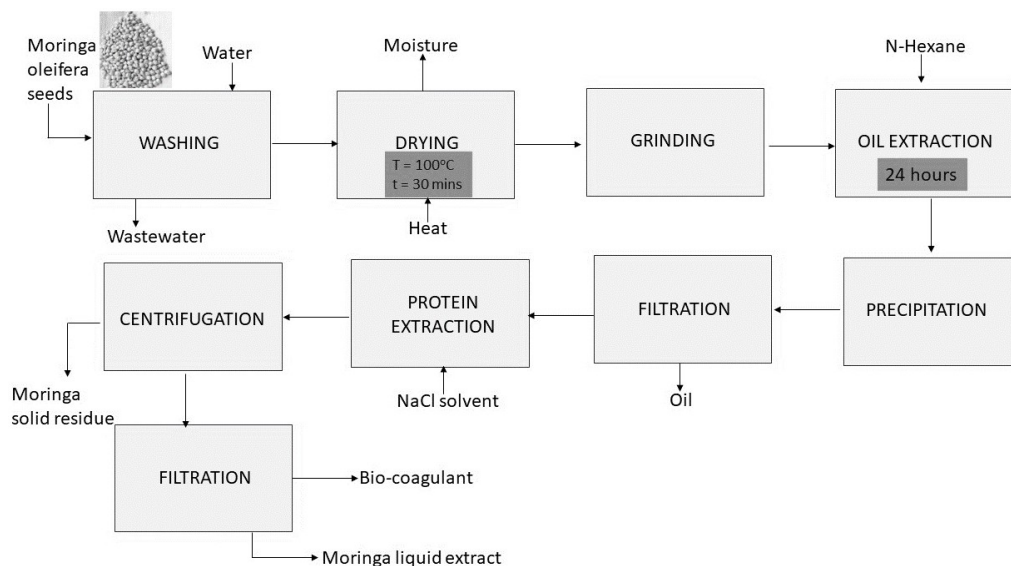

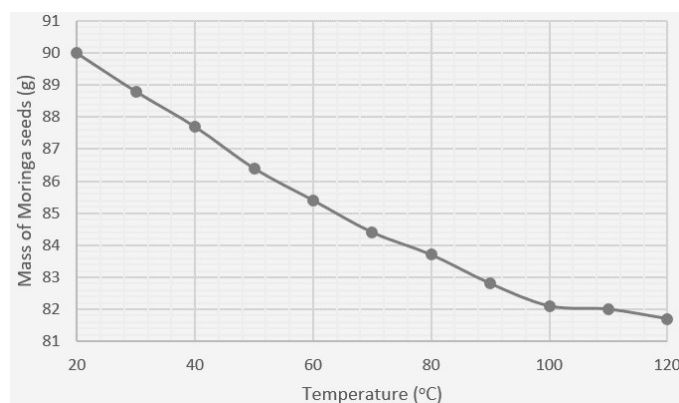Figure 2. Graphical methodology for the process.

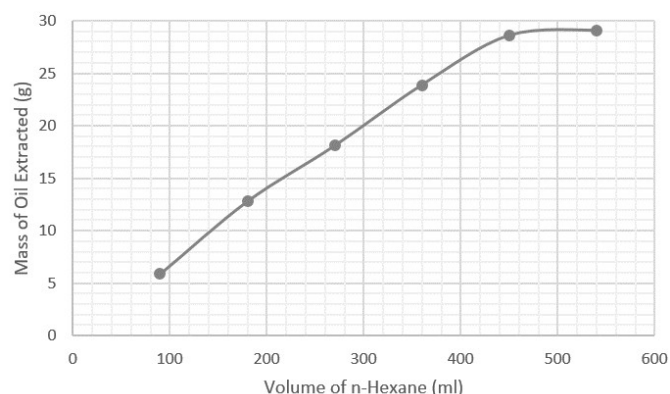Figure 3. Determination of moisture content in moringa seed.

Figure 4. Effects of varying moles of n-hexane for oil extraction.

Table 1. Wastewater characteristics.

Parameter	Method	Quantity determined
Total dissolved solids	Gravimetric SOP/CM11	1722mg/l
Total suspended solids	Gravimetric SOP/CM35	114mg/l
Dissolved oxygen	Electrode SOP/CM51	36.8 saturation%
Oxygen absorbed (PV)	Titrimetric SOP/CM25	90mg/l
Chloride	Titrimetric SOP/CM07	14mg/l Cl
Copper	AAS Flame SOP/CM22	<0.01mg/l Cu
Chromium	Spectrophotometric SOP/CM08	<0.01 mg/l Cr^{6+}
Conductivity	Electrode SOP/CM12	18.55 uS/cm
Iron	AAS Flame SOP/CM22	7.74 mg/l Fe
Lead	AAS Flame SOP/CM22	0.31 mg/l Pb
Nitrates	Spectrophotometric SOP/CM23	18.68mg/l N
Phosphates	Spectrophotometric SOP/CM28	2.8 mg/l P
Potassium	Flame photometric SOP/CM31	10.9 mg/l K
Sodium	Flame photometric SOP/CM31	575.70 mg/l Na
Sulfate	Turbidimetric SOP/CM33	120 mg/l SO_4
Zinc	AAS Flame SOP/CM22	0.23 mg/l Zn

Table 2. Effect of bio-coagulant dosage on turbidity reduction efficiency.

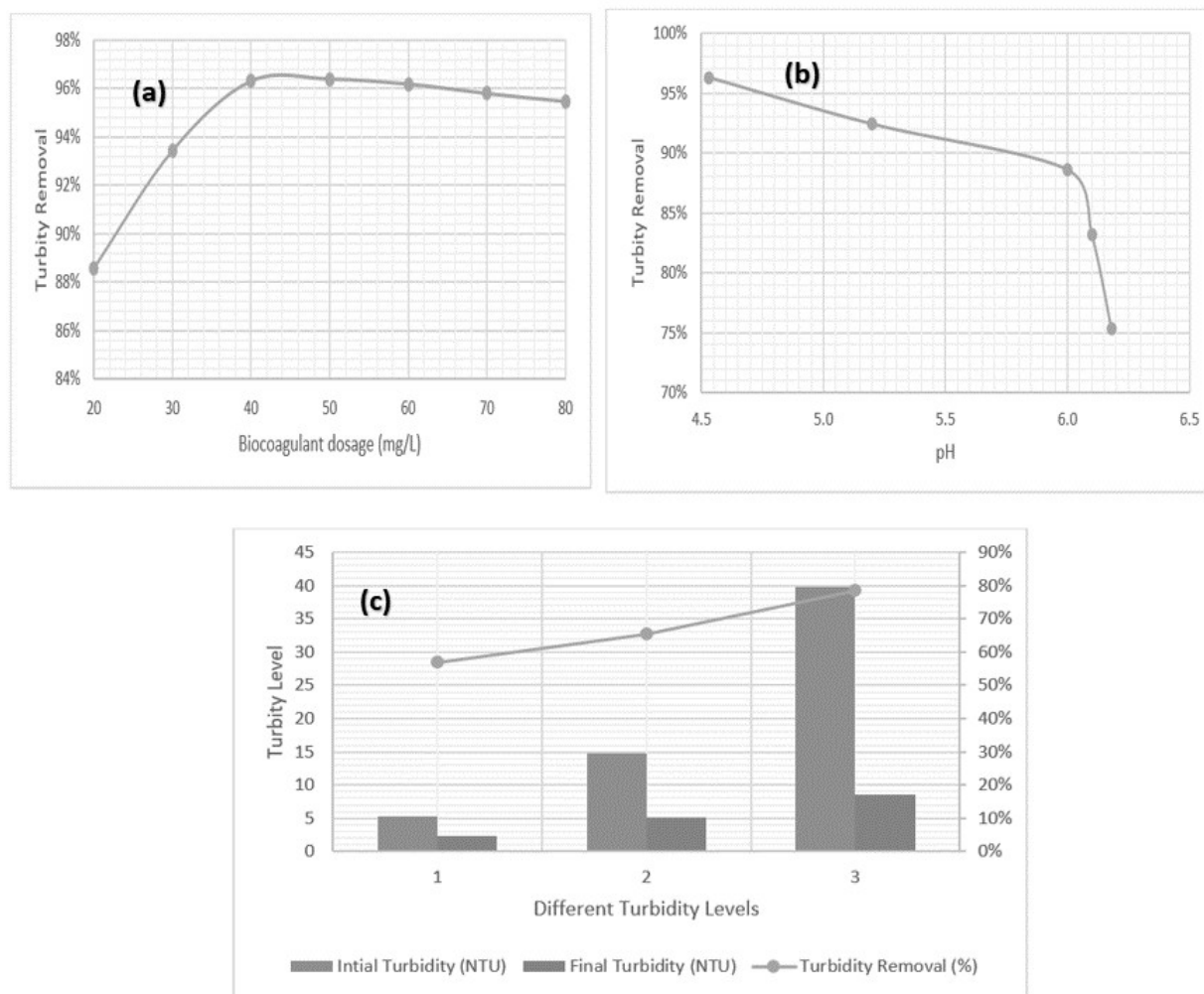| Biocoagulant dosage (mg/L)	Initial turbidity (NTU)	Final turbidity (NTU)	Turbidity removal (%)
20	38.6	4.41 ± 0.02	88.6
30	38.6	2.53 ± 0.05	93.4
40	38.6	1.42 ± 0.03	96.3
50	38.6	1.39 ± 0.04	96.4
60	38.6	1.47 ± 0.05	96.2
70	38.6	1.62 ± 0.05	95.8
80	38.6	1.75 ± 0.03	95.5

Figure 5. (a) Effects of bio-coagulant dosage on turbidity removal efficiency, (b) effect of bio-coagulant dosage on pH, and (c) performance of bio-coagulant dosage on different turbidity levels.

CONCLUSION

The protein in moringa seeds can potentially be used as a bio-coagulant. The optimum temperature for drying the moringa seeds was 100 °C for 30 min. The results showed that the highest oil yield of 31% was obtained from n-hexane since it is a more non-polar solvent, hence highly recommended for seed oil extraction. The highest turbidity removal efficiency of 96.4% was at low dosages of 50 mg/L, where all the colloids were neutralized and precipitated. A high turbidity removal of 88.6% was also obtained at an optimum pH of 6.1. *M. oleifera* bio-coagulant was found to be more effective in water of high turbidity due to more

frequent contact of the ions in the bio-coagulant and forming heavy flocs, hence providing high efficiency.

Further studies on the performance of the bio-coagulant in powder form for turbidity reduction efficiency must be carried out. Vacuum drying method or freeze-drying method can be used.

REFERENCES

[1] A. Benettayeb, M. Usman, C.C. Tinashe, T. Adam, B. Haddou, Environ. Sci. Pollut. Res. 32 (2022) 48185-48209. https://doi.org/10.1007/s11356-022-19938-w.

[2]　A. Ndabigengesere, K.S. Narasiah, B.G. Talbot, Water Res.29 (1995) 703–710. https://doi.org/10.1016/0043-1354(94)00161-Y.

[3]　S. Nouhi, H.M. Kwaambwa, P. Gutfreund, A.R. Rennie, Sci. Rep. 9 (2019)1-10. https://doi.org/10.1038/s41598-019-54069-2.

[4]　C.S.T. Araújo, V.N. Alves, H.C. Rezende, I.L.S. Almeida, R.M.N. de Assunção, C.R.T. Tarley, M.G. Segatelli, N.M.M. Coelho, Water Sci. Technol. 62 (2010) 2198-2203. https://doi.org/10.2166/wst.2010.419.

[5]　L.L. Salazar Gámez, M. Luna-del Risco, R.E.S. Cano, Environ. Monit. Assess.187 (2015) 668 https://doi.org/10.1007/s10661-015-4793-y.

[6]　S. Boulaadjoul, H. Zemmouri, Z. Bendjama, N. Drouiche, Chemosphere. 206 (2018) 142-149. https://doi.org/10.1016/j.chemosphere.2018.04.123.

[7]　W.L. Ang and A.W. Mohammad, J. Clean. Prod. 262 (2020) 121267. https://doi.org/10.1016/j.jclepro.2020.121267.

[8]　N.U. Yamaguchi, L.F. Cusioli, H.B. Quesada, M.E.C. Ferreira, M.R. Fagundes-Klen, A.M.S. Vieira, R.G. Gomes, M.F. Vieira, R. Bergamasco, Process Saf. Environ. Prot.147 (2021) 405-420. https://doi.org/10.1016/j.psep.2020.09.044.

[9]　D.L. Villaseñor-Basulto, P.D. Astudillo-Sánchez, J. del Real-Olvera, E.R. Bandala, J. Water Process Eng. 23 (2018) 151-164. https://doi.org/10.1016/j.jwpe.2018.03.017.

[10]　L. Liang, C. Wang, S. Li, X. Chu, K. Sun, Food Sci. Nutr. 7 (2019) 1754-1760. https://doi.org/10.1002/fsn3.1015.

[11]　H. Barakat G.A. Ghazal, Food Nutr. Sci. 7 (2016) 472-484. https://doi.org/10.4236/fns.2016.76049.

[12]　M. Alain Mune Mune, E.C. Nyobe, C. Bakwo Bassogog, S.R. Minka, Cogent Food Agric. 2 (2016) 1213618. https://doi.org/10.1080/23311932.2016.1213618.

[13]　K. Bombo, T. Lekgoba, O. Azeez, E. Muzenda, Environ. Clim. Technol. 25 (2021) 151-160. https://doi.org/10.2478/rtuect-2021-0010.

[14]　T.A. Aderinola, T.N. Fagbemi, V.N. Enujiugha, A.M. Alashi, R.E. Aluko, Heliyon. 4 (2018) e00877. https://doi.org/10.1016/j.heliyon.2018.e00877.

[15]　V. Javed, S. Javed, H.U. Saeed, T. Abbas, I. Technology, DSSR. 3 (2025) 77-88.

[16]　M. M. Maroneze, L.Q. Zepka, J.G. Vieira, M.I. Queiroz, E. Jacob-Lopes, A&A. 9 (2014) 445-458. https://doi.org/10.4136/1980-993X.

[17]　J.R. Silva D. S. Oliveira, Clean Technol. 6 (2024) 625-645. https://doi.org/10.3390/cleantechnol6020033.

[18]　R. W. Saa, E.N. Fombang, E.B. Ndjantou, N.Y. Njintang, Food Sci. Nutr. 7 (2019) 1911-1919. https://doi.org/10.1002/fsn3.1057.

[19]　N.E. Nwaiwu A.A. Bello, Res. J. Appl. Sci. Eng. Technol. 3 (2011) 505-512.

[20]　R.S. Putra, M. Ayu, R.Y. Amri, Key Eng. Mater. 840 (2020) 29-34. https://doi.org/10.4028/www.scientific.net/kem.840.29.

[21]　B.A. Adejumo, IOSR J. Agric. Vet. Sci. 1 (2012) 12-21. https://doi.org/10.9790/2380-0151221.

[22]　E. Ajav O. Fakayode, Agrosearch.13 (2013) 115. https://doi.org/10.4314/agrosh.v13i1.11.

[23]　D.O. Oloyede, N.A. Aviara, S.K. Shittu, J. Biosyst. Eng. 40 (2015) 201-211. https://doi.org/10.5307/jbe.2015.40.3.201.

[24]　M.M.S. Arreola, J.R.L. Canepa, J.R.H. Barajas, Interciencia. 41(2016) 548-551.

[25]　Q. Du, Y. Wu, S. Xue, Z. Fu, LWT. 155 (2022) 112988. https://doi.org/10.1016/j.lwt.2021.112988.

[26]　G.S. Madrona, I.G. Branco, V.J. Seolin, B. De, Acta Sci. Technol. 34 (2012) 289-293. https://doi.org/10.4025/actascitechnol.v34i3.9605.

[27]　A. Gautier, C.M. Duarte, I. Sousa, Foods. 11, (2022) 1629. https://doi.org/10.3390/foods11111629.

[28]　A. Jain R.S.B.M.C. Radha, J. Food Sci. Technol. 56 (2019) 2093-2104. https://doi.org/10.1007/s13197-019-03690-0.

[29]　B.O. Mbah, P.E. Eme, O.F. Ogbusu, Pakistan J. Nutr.11 (2012) 211-215. https://doi.org/10.3923/pjn.2012.211.215.

[30]　O.A. Abiodun, J.A. Adegbite, O. Omolola, Glob. J. Sci. Front. Res.12 (2012) 13-17.

[31]　P. Bridgemohan, R. Bridgemohan, M. Mohamed, African J. Food Sci. Technol. 5 (2014) 125-128. http:/doi.org/10.14303/ajfst.2014.041.

[32]　E. Kusumawati, Keryanti, E.M. Widyanti, F. Waluya, Risnawati, Adv. Eng. Res. 198 (2020) 365-370. https://doi.org/10.2991/aer.k.201221.060.

[33]　M. H. Ng M.S. Elshikh, Ind. Domest. Waste Manag. 1 (2021) 1-11. https://doi.org/10.53623/idwm.v1i1.41.

MANDA ZVIUYA[1]

JOSEPH GOVHA[1]

PLACXEDES SIGAUKE[2]

TIRIVAVIRI A. MAMVURA[2]

GWIRANAI DANHA[2]

[1]Department of Chemical and Process Systems Engineering, Harare Institute of Technology, Harare, Zimbabwe.

[2]Department of Chemical, Materials and Metallurgical Engineering, Faculty of Engineering and Technology, Botswana International University of Science and Technology, Palapye, Botswana

NAUČNI RAD

POTENCIJALNA PRIMENA SEMENA *Moringa Oleifera* KAO BIO-KOAGULANTA

Ova istraživanja su fokusirana na dobijane prirodnog bio-koagulanta iz semena moringe (Moringa oleifera). Ekstrakt semena moringe je prirodni koagulant za tretman vode koja sadrži suspendovane čvrste materije i koloide i dobija se mlevenjem, ekstrakcijom ulja, ekstrakcijom proteina iz čvrstih materija pomoću 2 M rastvora NaCl i odvajanjem proteina centrifugiranjem i filtracijom. Istraživani parametri dobijanja bio-koagulanta uključuju uticaj temperature na uklanjanje sadržaja vlage u semenu moringe, vrstu rastvarača na prinos ulja i variranje zapremine n-heksana za ekstrakciju ulja. Parametri vezani za korišćenja bio-koagulanta uključuju uticaj doze bio-koagulanta na pH i efikasnost uklanjanja zamućenosti, kao i performanse bio-koagulanta na niskim, srednjim i visokim nivoima zamućenosti. Optimalna temperatura i vreme sušenja semena moringe bili su 100 °C tokom 30 minuta, a najveći prinos ulja bio je 31% kada se koristi n-heksan kao rastvarač. Efikasnost uklanjanja zamućenosti porasla je do 96,4% kada se koristi 50 mg/L bio-koagulanta pri pH vrednosti 6,1. Visok stepen uklanjanja zamućenosti postignut je pri niskim dozama biokoagulanta, što se smatra revolucionarnim otkrićem ovog istraživanja.

Ključne reči: Seme Moringa oleifera, n-heksan, bio-koagulant, tretman vode.

BRANKA RUŽIČIĆ[1],

DRAGANA GRUJIĆ[1],

ALEKSANDAR SAVIĆ[1],

LJILJANA TOPALIĆ-TRIVUNOVIĆ[1],

ANA VELEMIR[1],

BLANKA ŠKIPINA[1],

SANDRA DEDIJER[2],

MILJANA PRICA[2]

[1]University of Banja Luka, Faculty of Technology, Bulevar Vojvode Stepe Stepanovića 73, Banja Luka, Bosnia and Herzegovina

[2]University of Novi Sad, Faculty of Technical Sciences, Trg Dositeja Obradovića 6, Novi Sad, Serbia

GRAPE POMACE EXTRACT AS A COLORANT FOR TEXTILE PRINTING APPLICATIONS

Highlights

- The extract's color is pH-dependent, with the most intense magenta at pH 2.
- Grape pomace extract showed significant antioxidant and moderate antibacterial activity.
- Printed fabrics showed antioxidant and antibacterial activity.
- Extract with a suitable carrier enhances antimicrobial efficacy in textile applications.

Abstract

The growing need to reduce the negative impact on the environment and human health, as well as to meet the growing demand for eco-friendly textiles, has led to the development of environmentally friendly printing techniques and the use of natural dyes in the textile industry. Grape pomace is an important waste material in winemaking and has been extensively studied for its potential as a source of compounds with biological properties, especially anthocyanins, pigments responsible for the red, purple, and blue colors in grapes. The aim of this paper was to examine the potential use of natural dye extracted from grape pomace of domestic cultivar crna Mirisavka (GPCM) in preparation of printing paste with alginate, citric acid, and tannic acid for printing on cotton fabric. Special focus was placed to achieve process color magenta, by adjusting the pH value of the extract obtained. The natural dye from GPCM was extracted using maceration with 80% methanol, followed by sonication to enhance the yield of bioactive compounds. GPCM extract demonstrated significant antioxidant activity measured by FRAP, DPPH, and ABTS$^+$ tests, and moderate antibacterial activity against Staphylococcus aureus and Escherichia coli. The pH-dependent stability of anthocyanins in GPCM extract was examined, demonstrating a magenta tone at acidic pH (pH 2-4) and color degradation at higher pH values. Cotton fabric printed with two different concentrations of GPCM extract (100 mg/L and 50 mg/L) showed good antioxidant and antibacterial activity. Based on the obtained results, it can be concluded that GPCM extract can be an environmentally friendly solution for the development of antibacterial and antioxidant textiles, with potential application in the production of protective clothing in healthcare institutions, as well as for the production of decorative home textiles, for the production of children's toys and textiles for packaging.

Keywords: Grape pomace extract; Antibacterial activity; Antioxidant properties; Anthocyanins; pH stability, Screen printing.

INTRODUCTION

The textile production process is considered potentially harmful due to its negative impact on the environment. Today, the main goal of the textile industry is to maintain product quality and to develop new manufacturing techniques that promote environmental sustainability, worker health, and consumer satisfaction [1]. The use of synthetic dyes became one of the major problems, which led to an increase in finding eco-friendly practices [2,3], especially with the development of eco-friendly natural dyes and biomordants for textile dyeing [4,5]. Natural dyes are better than synthetic dyes due to environmental friendliness, lack of toxicity, allergenicity, etc. [6-8]. Despite the somewhat higher overall production cost, natural inks offer added value through their biodegradability, potential functional properties (e.g., antioxidant or antimicrobial activity), and environmental sustainability. These aspects

may outweigh the economic disadvantages in niche applications such as eco-friendly textiles or functional materials [1,3].

For the extraction of biodegradable and ecologically friendly natural dyes, a wide variety of plant, floral, and fruit-based materials can be used [9]. Among the fruit-based materials, grapes are one of the most widely produced crops globally, with wine production estimated at 235 million hectoliters [10]. About 75% of grapes are used for wine, producing a large amount of by-products, mainly grape pomace, consisting of skins, pulp, seeds, and stalks. The disposal of this waste creates environmental concerns due to its capacity to pollute the soils and reduce the availability of other ingredients [11]. However, having a high content of bioactive compounds makes grape pomace valuable for various applications, including human health benefits [12].

Grape pomace has been extensively studied for its potential as a source of bioactive compounds with antimicrobial and antioxidant properties [12-16]. The main bioactive compounds in grape pomace are: polyphenols, including phenolic acids, flavonoids such as anthocyanins (ACs), etc. [12,15,16]. ACs are the pigments responsible for the red, purple, and blue colors in grapes [12,17]. ACs, particularly those found in red grape varieties have the potential to be used as natural dyes for textile applications [17]. The AC content in grape pomace can vary significantly depending on the grape variety, climate, and winemaking process [18,19]. Therefore, it is important to investigate the AC profile of different grape pomace sources to identify the most suitable ones for natural dye applications.

Additionally, factors like pH, temperature, and the presence of other compounds like ascorbic acid and maltodextrin can affect the stability of ACs and their performance as dyes [20]. The color of ACs is highly dependent on the pH of the environment [21-23]. At low pH values (pH < 3), ACs exist predominantly in the red-colored flavylium cation form [24-26]. As the pH increases, the AC molecules undergo structural transformations, leading to changes in their color [21,22,26]. In slightly acidic to neutral pH (pH 3-7), ACs can exist in various forms, including the colorless hemiketal and the blue-violet quinoidal base forms [24-26]. In alkaline conditions (pH > 7), ACs tend to become more yellow or green due to the formation of the chalcone form [27,28]. The stability of ACs is also influenced by pH value, with the most stable form being the flavylium cation at low pH values [24-26,29], which is responsible for the magenta color [30]. Beyond their coloring properties, ACs from grape pomace also exhibit antioxidant and anti-inflammatory activities, which can be beneficial for various applications, including food, cosmetics, and pharmaceuticals [12,15]. The synergistic effects of ACs and other polyphenolic compounds in grape pomace extracts have also been reported to have antimicrobial properties, which could be leveraged for textile applications [13,31].

Cantika and Hendrawan emphasized that a number of methods can be used for the application of natural dyes on textiles [32]. One of them, screen printing, can be used to add leaf and floral patterns to textiles [33]. Screen printing is an eco-printing method and the waste generated is environmentally friendly since the fabrics and dyes used are made from natural materials [34]. According to Amutha and Annapoorani, natural dyes can be printed directly onto fabrics with a suitable formulation [35].

Screen printing, a versatile and widely utilized printing technique, relies on various types of inks to achieve desired colors and effects. Also, the curing process has a huge impact on the print performance [36]. Natural inks, being biodegradable and environmentally friendly, offer a sustainable alternative to synthetic counterparts, as they reduce environmental pollution and can be sourced from renewable resources. Moreover, the unique properties of natural inks, such as bioactivity and low toxicity, align with global trends toward greener production methods, and the growing demand for environmentally conscious products [37,38]. Magenta is one of the primary colors in the subtractive color model (CMYK), alongside cyan, yellow, and black. It is essential for creating a wide spectrum of colors through blending [39]. The inclusion of natural magenta ink in screen printing not only offers an environmentally friendly alternative but also enables the creation of visually appealing and intricate patterns on textiles, enhancing both their aesthetic and functional value [40]. A natural printing process should be developed to lessen negative effects on health and the environment.

There is a significant body of research on the potential applications of grape pomace in the food, cosmetic, and pharmaceutical industries, but minimal data is available on the performance of cotton fabrics dyed with grape pomace extract as a natural colorant, and alternative to synthetic dyes, for textile printing applications [41,42]. Magenta printing paste can be prepared from grape pomace extract and can be used commercially for sustainable textile printing practices. Antibacterial and antioxidant properties of extract and printed textiles are, also, very important, and will be investigated to uphold the use of grape pomace. The results will offer essential information on the resource efficiency and economic opportunities of using natural dye from grape pomace in eco-sustainable printing of cotton, for example in sustainable fashion, home textiles, etc. Also, phenol-rich extracts can prevent oxidative and microbial damage, and offer the possibility of application in the development of natural antioxidant and antimicrobial dyes for textile printing.

Materials and methods

In this study, the potential use of GPCM for obtaining extract through ultrasonic extraction was investigated. The obtained GPCM extract was analyzed for its antioxidant and antibacterial properties, as well as spectrophotometric characteristics. The optimal pH value of the extract, at which the AC content was the highest, was determined, and cotton fabrics were printed using an alginate paste modified with extract GPCM, citric acid, and tannin. The entire research process is schematically presented in Figure 1.
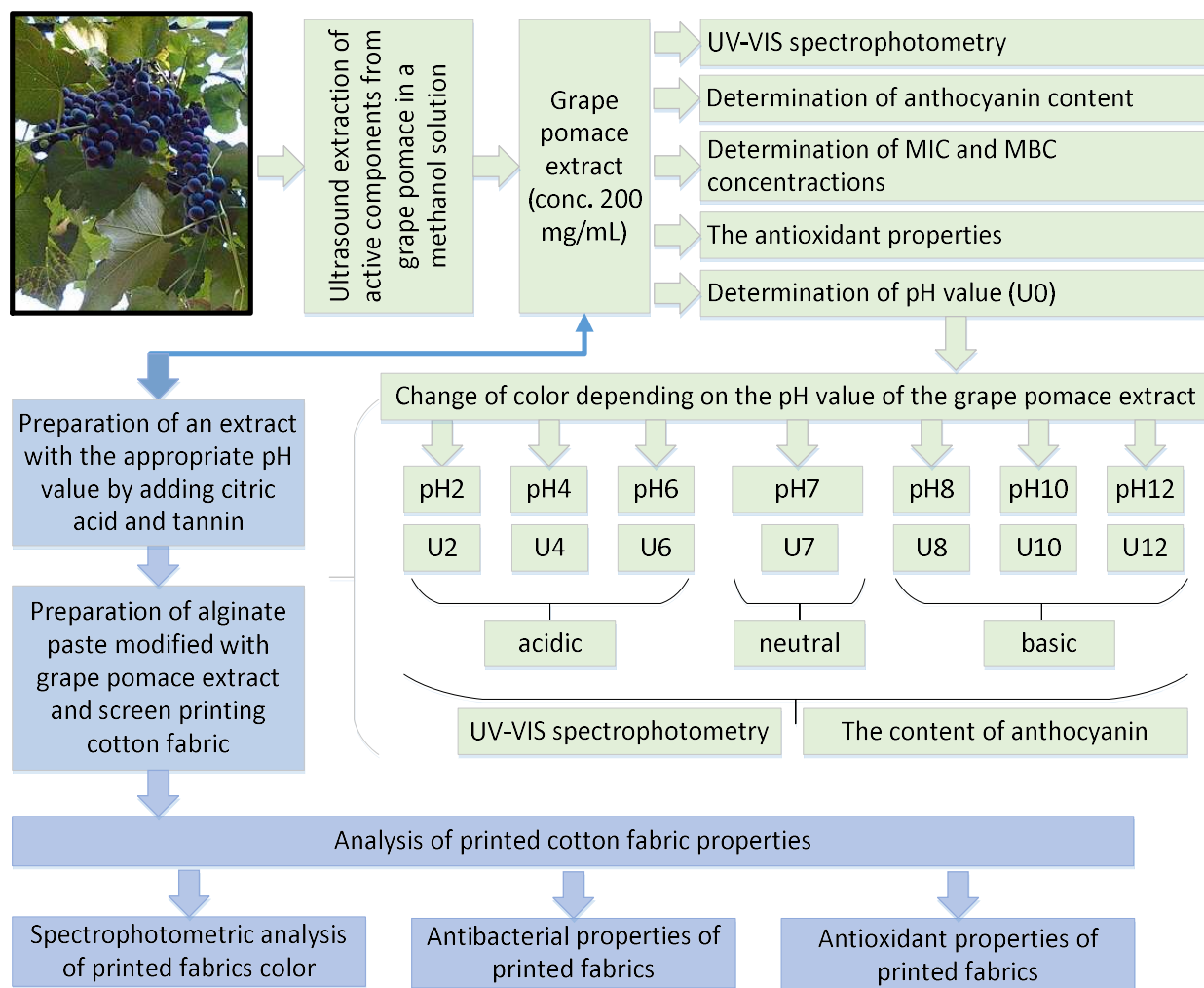
Figure 1. Schematic presentation of experiment

GPCM extract preparation

GPCM used in this study was collected as a by-product during juice preparation. After collection, GPCM was stored at a low temperature (-20 °C) until processing to preserve the biological activity of phenolic compounds. Also, prepared crude extracts of *Vitis vinifera* L. grapes are stored at -20 °C until further analysis [43]. GPCM was subjected to maceration in 80% methanol for 24 hours with occasional stirring, then treated with ultrasound for 18 min to enhance extraction efficiency. Ultrasound is an environment-friendly, inexpensive, fast, and efficient extraction technology for phenolic components due to acoustic cavitation caused by the ultrasound wave passage. Acoustic cavitation results in the rupture of cell walls, allowing solvent penetration and improving mass transfer, leading to an increase in extraction yield and shortening extraction time [44]. Azmir *et al.* [45] stated that moisture content, sample, sample size, solvent employed, temperature, frequency, and probe time are the factors that may influence the extraction process in ultrasound-assisted extraction. Many researchers have used ultrasound for more efficient preparation of medicinal plant extracts [46,47].

After maceration and sonication, the obtained GPCM extract was filtered to remove solid particles. The filtered extract was further concentrated using a vacuum evaporator at 40 °C and then dried in Petri dishes at 50 °C. The resulting dry GPCM extract was dissolved in 60% methanol to a final concentration of 200 mg/mL.

Regulation of pH value and spectrophotometric analysis

The pH value of the prepared GPCM extract was 4.3 (U0). The pH values of U0 were adjusted at: pH 2 (U2), pH 4 (U4), pH 6 (U6), pH 7 (U7), pH 8 (U8), pH 10 (U10), and pH 12 (U12) using 0.1 M hydrochloric acid (HCl) for acidification, and 0.1 M sodium hydroxide (NaOH) for alkalization. For precise measurement, the HANNA HI 2211 pH meter was used.

The spectrophotometric analysis of the pH-adjusted extracts was performed using a Perkin Elmer Lambda 25 UV/VIS spectrophotometer with glass cuvettes and 60% methanol as the control sample. The absorbance (A) and transmittance (T) of the adjusted extracts were measured in the visible spectrum range of 360-740 nm.

Antibacterial activity

In this study, to determine the antibacterial activity of GPCM extract was used the agar dilution method to obtain the minimum inhibitory (MIC) and minimum bactericidal (MBC) concentrations [48]. Two bacterial cultures, *E. coli* ATCC 25922 and *S. aureus* ATCC 25923 were used. For this study, bacterial cultures were prepared from the logarithmic phase and by direct colony suspension [48,49].

A standard inoculum of *E.coli* from the logarithmic growth phase was prepared in the following way. Namely, the culture was seeded on Miller Hinton agar plates (MHA) and incubated at 37 °C for 24 h. After that, 3-5 isolated colonies were transferred to a 5 mL tube containing Miller Hinton broth (MHB) and incubated for the next 2-6 h. On the other hand, *S. aureus* was inoculated from agar slants onto Nutrition agar plates. The prepared agar plates were then incubated for 24 h at 37 °C. Thereafter, two or three colonies were collected directly into the MHB.

After incubation for 2-6 h or after preparation of the colony suspension, the culture density was determined spectrophotometrically (at 620 nm), using the 0.5 McFarland standard (1.5×10^8 cfu/mL) for comparison. The cultures were then diluted properly and their density was adjusted to 1.5×10^6 cfu/mL.

Agar dilution method

A series of dilutions in agar was prepared by adding an appropriate amount of the GPCM extract to the dissolved medium (MHA) cooled to 45 °C. The final concentration of the extract in the medium was in the range of 10-40 mg/mL (10, 20, 30, and 40 mg/mL). Then, the substrates were shaken well and poured into sterile Petri dishes. After the medium had hardened, the cultures were seeded in 10 μL drops on the surface of the agar plates and incubated at 37 °C for 24 h. The inhibition zones of the growth of the microbial cultures were measured. The highest dilution of the tested extract that inhibited the visible growth of bacteria was considered the MIC value. From the plates that showed no visible signs of growth/cloudiness in the MIC determination, the test microorganisms were inoculated onto sterile MHA plates. The plates were then incubated at 37 °C for 24 h. The lowest concentration that showed no growth of the test organisms was considered as MBC. The medium without extract was used as a control.

Antioxidant activity

The total phenolic content (TPC) was determined spectrophotometrically using a modified Folin-Ciocalteu method [50]. Non-flavonoids (NFs) were quantified using the formaldehyde precipitation method [51], which precipitates flavonoids, and the remaining NFs were then measured using the aforementioned Folin-Ciocalteu method. Total flavonoids (TFs) were calculated as the difference between TPC and NFs.

The concentration of ACs was determined using the spectrophotometric method described by Somers and Evans [52]. This method measures the total concentration of ACs, ionized ACs, colorless ACs, and polymeric forms, as well as the degree of AC ionization.

The antioxidant analysis was performed using the following methods: FRAP [53], DPPH [54], and modified ABTS+ [55]. The data for calculating antioxidant properties were measured using a UV-VIS spectrophotometer (Milton Ray Spectronic 1201).

Preparation of printing paste

The alginate paste CHT-NV was prepared by adding 69 mL of distilled water at room temperature to 6 g of modified alginate. Continuous stirring was applied until a homogeneous paste was formed. To the prepared paste, 25 mL of GPCM extract (at concentrations of 50 mg/mL (sample E50) and 100 mg/mL (sample E100)) was added, and, as binders, 8 g/L of cross-linking agent citric acid [56], and 2 g/L of tannin to stabilize the color [57].

Momotaz *et al.* [58] observed that the antibacterial activity was superior to that of binder when the fixation process was carried out using mordant. Mordants facilitate better binding of antibacterial agents to the fabric fibers, leading to more stable and long-lasting antimicrobial properties. Tannins as natural mordants can form complexes with antibacterial compounds, enhancing their retention on the textile surface, which may improve their effectiveness.

Spectrophotometric analysis and the determination of AC content in adjusted extracts revealed that a pH of 2 is suitable for achieving a magenta color. Added citric lowers the initial extract's pH (4.3) to pH 2, which additionally contributes to the stability of ACs in acidic conditions and enhances the overall antioxidant activity of the sample.

Screen printing of cotton fabrics

For the final experiment, a plain weave cotton fabric with a surface mass of 123.36 g/m², density of 23 threads/cm in the warp, and 21 threads/cm in the weft was used as the printing substrate. The cotton fabric was printed using the semi-automatic screen printing machine S-300. The screen mesh was made of 100% polyester monofilament, with a mesh density of 10 threads/cm (25 threads/inch), a thread diameter of 300 μm, a mesh opening of 700 μm, and a thickness of 570 μm. The mesh structure was a plain weave. Each fabric sample was printed in two passes. The sieve line used (10 threads/cm), considering the viscosity of the paste, enables a good flow of the paste and adequate coverage. Ahmad *et al.* used a higher screen density (110 threads/inch), due to the different structure of the paste, to obtain a precise impression [42].

Measuring the color coordinates of printed samples

To describe color reproduction, the CIE LabCh color coordinates and spectral reflectance curves were used. A Konica Minolta CM-2600d spectrophotometer was employed to determine the color coordinates (illumination type D65, standard observer angle 10°, measurement geometry d:8°, measurement aperture 11 mm, spectral range 360-740 nm with a 10 nm step). A graphical representation of the object's spectral response at various wavelengths of the electromagnetic spectrum is referred to as the spectral reflectance curve. It shows the reflectance in the visible spectrum and can provide valuable insights for

characterizing the colors of the sample's surface [59].

Antibacterial properties of printed samples

The antibacterial activity of the printed samples was tested using the agar diffusion method [60,61]. The following microorganisms were used for testing: *S. aureus* ATCC 25923 and *E. coli* ATCC 25922. Bacterial cultures were grown on Nutrition agar plates, and a suspension of the cultures was prepared in physiological saline. The density of *S. aureus* and *E. coli* was adjusted spectrophotometrically to approximately 1.5×10^6 cfu/mL. Then, 100 μL of each culture was spread on the surface of sterile MHA plates. The culture suspension was carefully distributed across the entire Petri dish surface using a sterile glass L-shaped rod. Fabric samples were then placed on the inoculated agar surface. The plates were incubated at 37 °C for 24 hours. After incubation, the inhibition zone (mm) was measured using the following formula:

$$Z_i = \frac{(T-D)}{2} \qquad (1)$$

where: Z_i is the width of the inhibition zone (mm), T is the total width of the sample plus the inhibition zone (mm), and D is the width of the sample (mm). If no inhibition zone was observed, but there was no growth beneath the samples, it was defined as contact inhibition (CI).

RESULTS AND DISCUSSION

Antioxidant activity of GPCM extract

TPC, TF, and NF contents of the GPCM extract were determined spectrophotometrically and are shown in Figure 2. TPC was 34.73 mg GAE/g, indicating a high level of bioactive compounds. NFs were the dominant group, with 22.12 mg GAE/g, and TFs accounted for 12.61 mg GAE/g. The antioxidant activity of GPCM extract was evaluated using the DPPH, ABTS⁺, and FRAP methods. The DPPH method demonstrated significant radical-scavenging ability (28.09 mM TE/g dry weight), but the FRAP method revealed a low iron-reducing capacity (0.52 mM Fe²/g dry weight), indicating limited direct electron-donating ability. However, the GPCM extract exhibited the highest antioxidant activity according to the ABTS⁺ method (104.89 mM TE/g dry weight). This suggests that the GPCM extract is effective against various types of free radicals and may contain diverse phenolic components with complementary mechanisms of action. This suggests the potential application of the extract in the development of natural antioxidant dyes for textile printing.

Antibacterial activity of GPCM extract

The GPCM extract demonstrated moderate antibacterial activity against *S. aureus* (MIC 30 mg/mL, MBC 40 mg/mL) and *E. coli* (MIC 20 mg/mL, MBC 30 mg/mL). Similar MIC and MBC values were reported by Peixoto *et al.* [16], who established a strong correlation between antimicrobial activity and phenolic content, particularly flavonoids, phenolic acids, and ACs. Phenolic compounds disrupt bacterial membrane function, penetrate the membrane, dissociate in the cytoplasm, and exert toxic effects [62]. Contrary to Peixoto *et al.* [17], this study found that the grape pomace extract exhibited stronger inhibition of the Gram-negative bacterium *E. coli* compared to the Gram-positive *S. aureus*. However, Fernández-Pérez *et al.* [63] reported a very low MIC for grape pomace extract of *Vitis vinifera* L. *cv.* Graciano, and that a higher TPC correlated with a higher antibacterial activity of the extracts. The phenolic composition of different *Vitis vinifera* varieties, as well as varying climatic and cultivation conditions, results in differences in phenolic content and, consequently, biological activity.

Regulation of pH value and spectrophotometric analysis

Experimental results showed changes in the color of GPCM extract depending on the pH value. Based on the results presented in Table 1, the changes in the concentration of ACs (total, ionized, and colorless) at different pH values, as well as the degree of ionization (α), can be analyzed.

With an increase in the pH of the samples, a decrease in AC concentration is observed, resulting in the loss of the red hue. The color of flavylium cations (red) is transformed into colorless chromenol. At pH values of 7-8, the ionized anhydro base of ACs transformed, leading to ring opening and the formation of chalcone, which gave the samples a yellow color. Under basic conditions (pH 10-12), ACs undergo further degradation, resulting in a significant reduction in concentration, and the samples acquired a brownish hue due to the presence of degradation products [20]. The proportion of ionized red flavylium cations was the highest at pH 2 (222.43 mg/L), with a degree of ionization of 82.54%, which resulted in an intense red color of the extract.

With increasing pH values, flavylium cations become colorless, which can be noticed by changes in light absorption [64]. Spectrophotometric analysis of transmittance and absorbance showed that samples at different pH values were transparent, but transparency decreased with increasing pH. It is expected that changes in pH values to affect the stability and structure of ACs, directly influencing the color components of the sample.

Figure 3a shows the spectral data of the samples. These data indicate that below 580 nm all samples show complete light absorption with no transmittance. At lower, acidic pH values, where the AC content is higher, samples allowed greater transmittance of light in the red region of the spectrum (620-740 nm). In contrast, samples at pH 12 showed nearly complete absorption in the visible spectrum, resulting from AC degradation and the formation of darker products.

The absorption graph (Figure 3b) highlighted the stability of absorption under neutral conditions (U6, U7, U8), while in acidic and basic regions, absorption curves were unstable. In the yellow region (chalcone, 580-600 nm) changes were most evident in samples U2, U10, and U12. Similarly, in the purple region (420-480 nm), shifts in absorption corresponded to the formation of quinonoid bases.

These changes in light absorption and sample color demonstrated the significant impact of pH value on the stability and structure of ACs. The results confirmed that an

acidic environment is most favorable for preserving the stability and color of ACs, while in basic conditions, degradation occurred, leading to inactive forms of ACs. Quantification results showed that the concentration of ACs was the highest at low pH (2), and decreased with increased pH. This is particularly important for applications in the textile industry, where color stability is important for the durability of color.
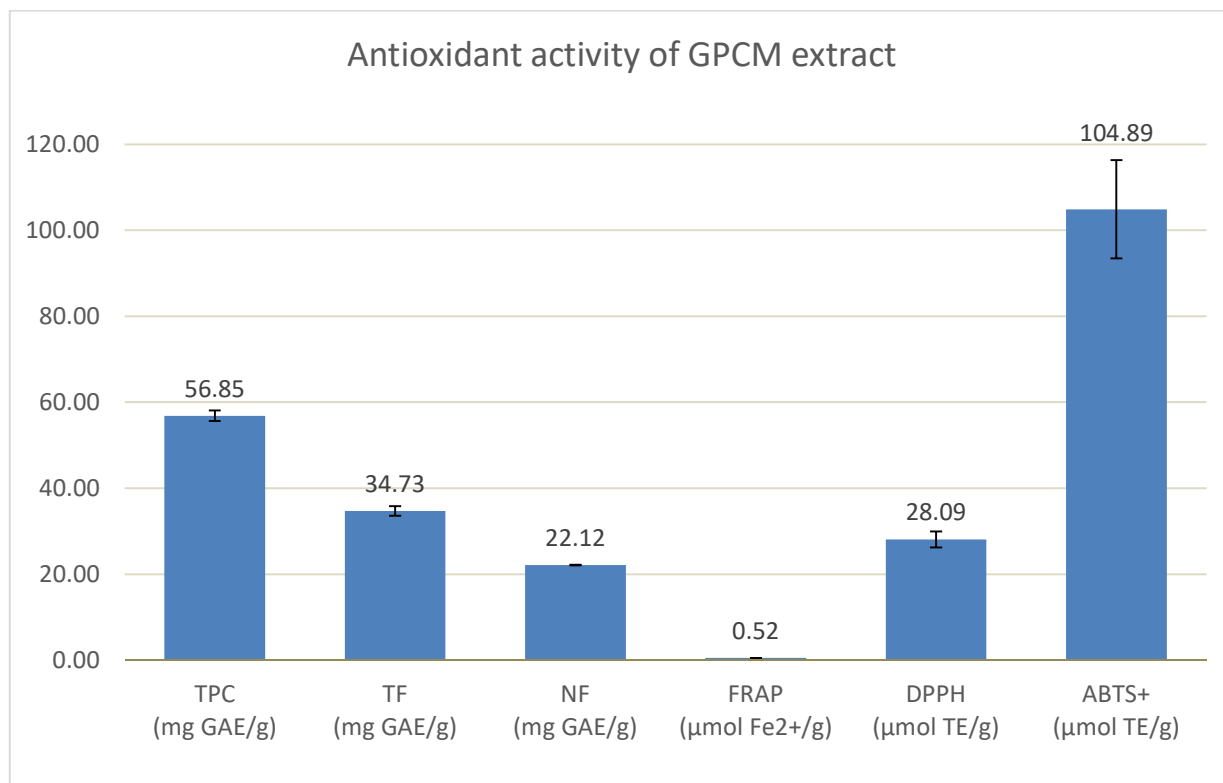

Figure 2. The antioxidant activity of the GPCM extract.

Table 1. Quantification of AC in the GPCM extract.

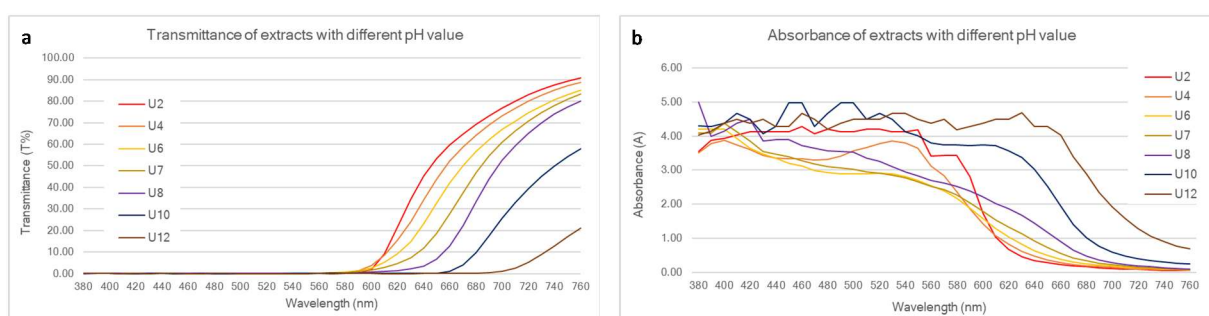| Sample label	pH value of GPE	AC (mg/L)	iAC (mg/L)	clAC (mg/L)	α
U0	4.3	265.69	73.49	192.20	27.66
U2	2	269.40	222.30	47.10	82.52
U4	4	287.91	61.46	226.45	21.35
U6	6	268.19	59.24	208.95	22.09
U7	7	237.19	52.59	184.60	22.17
U8	8	184.11	65.66	118.45	35.66
U10	10	50.07	ND	-	-
U12	12	63.91	ND	-	-

Figure 3. Spectrophotometric analysis of the GPCM extract at varying pH levels

Color coordinates of the printed samples

After mixing extracts (E50 and E100) with alginate paste and screen printing on cotton fabric, the spectrophotometric coordinates were measured (Table 2). It can be noticed that the samples have high lightness. The color was very subtle, which is expected for natural dye. Chroma rose with a higher concentration of extract, and the hue was between the blue and red axis. The hue angle (292-298°) corresponded with the desired magenta tone.

Table 2. Color coordinates of printed samples.

Sample	L*	a*	b*	C	h°
E50	90.35	3.24	-7.74	8.39	292.71
E100	88.81	4.64	-8.87	10.01	297.63

The spectral reflectance curves of the printed samples demonstrated the impact of the extract on the optical properties of the printed fabric and their potential to achieve magenta hues (Figure 4). At shorter wavelengths (360-460 nm), both samples had similar reflectance levels, with a peak reflectance observed between 440 nm and 460 nm, indicating the presence of blue tones. In the longer wavelength range (500-700 nm), the reflectance gradually decreased, with notable absorption in the 520-580 nm region, which is critical for the appearance of magenta. The sample printed with a higher extract concentration (E100) showed consistently lower reflectance values across the spectrum compared to the sample with a concentration of 50 mg/mL (E50), suggesting a darker and more intense coloration, particularly in the magenta-relevant range. These results confirmed that the higher extract concentration enhanced the ability to achieve stable and rich magenta tones.
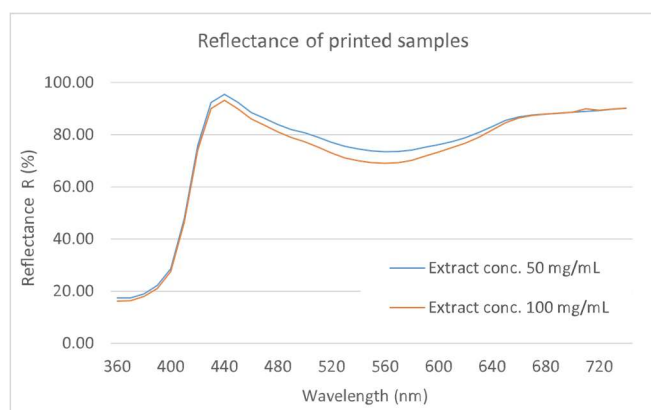

Figure 4. Spectral reflectance curves of printed samples.

Antioxidant activity of printed samples

TPC, TF, and NF content of printed samples with two extract concentrations are shown in Table 3. Sample E100 had higher TPC, TF, and NF contents than sample E50, likely due to the larger amount of extract used.

The antioxidant activity of the samples was evaluated using the DPPH, ABTS+, and FRAP methods. The results obtained using these tests showed that the sample E100 exhibited a stronger antioxidant effect than the sample printed with E50, most likely due to the higher content of phenolic compounds in the E100 sample, indicating a higher level of bioactive compounds contributing to the antioxidant properties of the printed sample. Phenol-rich extracts, particularly those high in flavonoids, have potential applications in the protection of textile materials due to their ability to prevent oxidative and microbial damage.

Table 3. The antioxidant activity of cotton fabric printed with alginate paste modified with the GPCM extract.

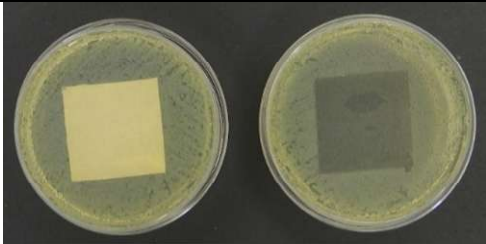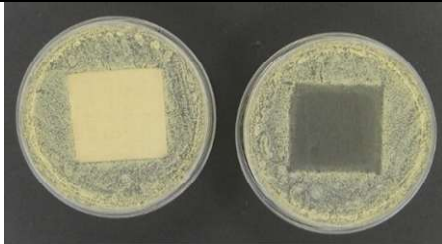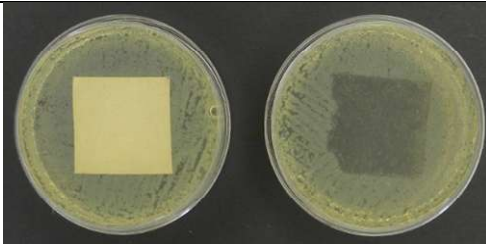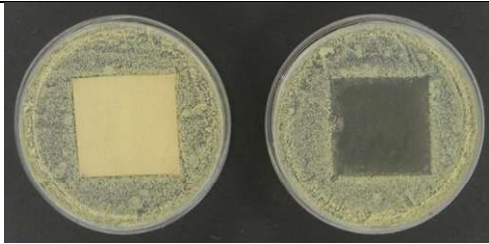| Sample	E50	E100
TPC (mg GAE/g)	1.343 ± 0.136	1.596 ± 0.107
TF (mg GAE/g)	0.17 ± 0.027	0.301 ± 0.226
NF (mg GAE/g)	1.172 ± 0.163	1.294 ± 0.119
FRAP (µmol Fe^{2+}/g)	20.87 ± 0.72	24.98 ± 0.22
DPPH (µmol TE/g)	6.715 ± 0.34	8.443 ± 0.242
ABTS$^+$ (µmol TE/g)	22.052 ± 0.997	28.606 ± 1.116

Antibacterial activity of printed samples

Based on the results of the antibacterial activity testing (table 4) of sample E100, the presence of contact inhibition on *E. coli* and *S. aureus* bacteria can be confirmed. The antibacterial activity of the sample E50 on *S. aureus* also showed contact inhibition, while on *E. coli* the effect was weaker and defined as partial contact inhibition (PCI). However, the presence of antibacterial activity in the printed sample in the form of PCI against *E. coli* still represented a significant effect, as *E. coli* is a highly resistant bacterium. The results obtained correlate well with the findings of the antioxidant properties analysis of printed samples.

Considering that the extracts were derived from grape pomace, where the MIC and MBC values of the extracts were low to moderate, the observed antibacterial activity of the printed samples can be considered a significant result. The improvement in antibacterial activity can be attributed to the reduction of the initial extract's pH from 4.3 to 2 by the addition of citric acid and tannin. These findings also highlighted the potential of the extract, when combined with a suitable binder, to enhance antibacterial efficacy in textile applications.

The functional finishing of textiles with plant extracts has indeed gained attention as an innovative area of research in the textile industry. Many researchers have explored dyeing textiles using plant extracts such as *Euclea divinorum* [38], *Achillea millefolium* [46,47], *Allium cepa*, *Zingiber ofcinale,* and *Nigella sativa* [58]. However, fewer studies have focused on textile printing using extracts [1,59]. From the studies mentioned, it is evident that the antimicrobial properties of dyed textiles are significantly better compared to those of printed textiles.

Table 4. Examination of the antibacterial activity of cotton fabric printed with alginate paste modified with GPCM extract on *E. coli* and *S. aureus* bacteria.

Sample	*E. coli*	*S. aureus*
E100		
	Contact inhibition (CI)	Contact inhibition (CI)
E50		
	Partial contact inhibition (PCI)	Contact inhibition (CI)

CI – contact inhibition (100% reduction of microorganisms under the sample

PCI – partial contact inhibition (more than 50% reduction of microorganisms under the sample)

(the right side of each petri dish indicates where the sample was removed from the agar plate)

CONCLUSIONS

This study explored the potential of grape pomace from domestic cultivar crna Mirisavka (GPCM) as a natural dye for screen printing applications on cotton fabrics. The results demonstrated that the extract's color properties were highly dependent on pH, with the most intense magenta tone observed at acidic pH values (pH 2). Spectrophotometric analysis revealed significant absorption in the magenta-relevant wavelength range (520-580 nm), confirming its suitability for achieving vibrant and stable colors. The antioxidant activity underscored the extract's potential to protect the fabric from oxidative damage, while its high flavonoid content contributed to its bioactive properties.

The printed fabrics exhibited promising antioxidant and antibacterial activity, particularly with extract at higher concentrations (100 mg/mL). These findings suggested that the extract's bioactive components, combined with alginate paste, enhanced antibacterial effects, making it a viable option for functional and aesthetic applications in the textile industry.

The use of grape pomace as a secondary raw material highlighted the potential of waste valorization to create eco-friendly products, reducing environmental impact and promoting sustainability. Investigations into the durability of these materials, color properties, antimicrobial effectiveness, and compatibility with other natural additives, would provide further insights into their industrial applicability.

The potential application of textiles printed with grape pomace extracts would be for the production of ecological antimicrobial children's toys, decorative objects, and packaging. Future research will be oriented towards the modification of printing pastes to improve the fastness of coloring to washing and UV radiation.

Acknowledgments

REFERENCES

[1] S. Rondanini, P. Díaz-García, I. Montava-Seguí, J. Gisbert Paya, E. Bou-Belda, Ann. Univ. Oradea, Fasc. Textile Leatherwork 21 (2020) 77-80.

[2] K. Niinimaki, L. Hassi, J. Cleaner Prod. 19 (2011) 1876-1883. https://doi.org/10.1016/j.jclepro.2011.04.020.

[3] J. Kang, C. Liu, S.H. Kim, Int. J. Consum. Stud. 37 (2013) 442-452. https://doi.org/10.1111/ijcs.12013.

[4] T.A. Ruhane, M.T. Islam, S. Rahaman, M.M.H. Bhuiyan, J.M.M. Islam, M.K. Newaz, K.A. Khan, M.A. Khan, Optik (Stuttgart, Ger.) 149 (2017) 174-183. https://doi.org/10.1016/J.IJLEO.2017.09.024.

[5] J. Ghosh, R. Repon, N.H. Anas, T. Noor, N. Mia, F. Khan, S. Sultana, N.S. Rupanty, SPE Polym. 5 (2024) 1-14. https://doi.org/10.1002/pls2.10144.

[6] S. Ananth, P. Vivek, T. Arumanayagam, P. Murugakoothan, Spectrochim. Acta, Part A 128

(2014) 420-426. https://doi.org/10.1016/J.SAA.2014.02.169.

[7] A. Alim, R. Repon, T. Islam, K.F. Mishfa, M.A. Jalil, M.D. Aljabri, M.M. Rahman, ChemistrySelect 7 (2022) 1-23. https://doi.org/10.1002/slct.202201557.

[8] R. Paliwal, M. Kumar, H.B. Bhatt, D. Vaya, G. Prasad, P.K. Surolia, SPE Polym. 5 (2024) 1-21. https://doi.org/10.1002/pls2.10147.

[9] B.D. Mistry, A Handbook of Spectroscopic Data Chemistry (UV, IR, PMR, 13CNMR and Mass Spectroscopy), Oxford Book Company, Jaipur, (2009).

[10] International Organisation of Vine and Wine, World Wine Production Outlook. https://www.oiv.int. [accessed 21 Dec 2024]

[11] P. Pereira, C. Palma, C. Ferreira-Pêgo, O. Amaral, A. Amaral, P. Rijo, J. Gregório, L. Palma, M. Nicolai, Foods 9 (2020) 1772. https://doi.org/10.3390/foods9121772.

[12] A.F. Vinha, C.S. Silva, G.M. Sousa, C.G. Moutinho, J. Brenha, R. Sampaio, Braz. J. Food Technol. 26 (2023) e2023020. https://doi.org/10.1590/1981-6723.02023.

[13] D. Sateriale, G. Forgione, M. Di Rosario, C. Pagliuca, R. Colicchio, P. Salvatore, M. Paolucci, C. Pagliarulo, Microorganisms 12 (2024) 437. https://doi.org/10.3390/microorganisms12030437.

[14] C.E. Luchian, V.V. Cotea, L. Vlase, A.M. Toiu, L.C. Colibaba, I.E. Raschip, G. Nadas, A.M. Gheldiu, C. Tuchilus, L. Rotaru, BIO Web of Conferences, in Proceeding of 42nd World Congress of Vine and Wine, Geneva, Switzerland (2019) p. 04006. https://doi.org/10.1051/bioconf/20191504006.

[15] E. Farina, H. Daghero, M. Bollati-Fogolin, E. Boido, J. Cantero, M. Moncada-Basualto, C. Olea-Azar, F. Polticelli, M. Paulino, Molecules 28 (2023) 3909. https://doi.org/10.3390/molecules28093909.

[16] C.M. Peixoto, M.I. Dias, M.J. Alves, R.C. Calhelha, L. Barros, S.P. Pinho, I.C.F.R. Ferreira, Food Chem. 253 (2018) 132-138. https://doi.org/10.1016/j.foodchem.2018.01.163.

[17] F.D. Fonseca, L. Symochko, M.N.C. Pinheiro, Sustainability 16 (2024) 3167. https://doi.org/10.3390/su16083167.

[18] M. Anđelković, B. Radovanović, A. Milenković Anđelković, V. Radovanović, A. Zarubica, N. Stojković, V. Nikolić, Adv. Technol. 4 (2015) 32-36. https://doi.org/10.5937/savteh1502032A.

[19] G.R. Caponio, F. Minervini, G. Tamma, G. Gambacorta, M. De Angelis, Sustainability 15 (2023) 9075. https://doi.org/10.3390/su15119075.

[20] B. Enaru, G. Drețcanu, T.D. Pop, A. Stănilă, Z. Diaconeasa, Antioxidants 10 (2021) 1967. https://doi.org/10.3390/antiox10121967.

[21] B. Gordillo, F.J. Rodríguez-Pulido, M.L. Escudero-Gilete, M.L. González-Miret, F.J. Heredia, J. Agric. Food Chem. 60 (2012) 2896-2905. https://doi.org/10.1021/jf2046202.

[22] A. Phan, N. Le, Sci. Technol. Dev. J. 20 (2018) 28-34. https://doi.org/10.32508/stdj.v20iK7.1208.

[23] B. Wiyantoko, A. Astuti, Indones. J. Chem. Anal. 3 (2020) 22-32. https://doi.org/10.20885/ijca.vol3.iss1.art4.

[24] F. Babaloo, R. Jamei, Food Sci. Nutr. 6 (2017) 168-173. https://doi.org/10.1002/fsn3.542.

[25] T. Zhao, M. Yu, Adv. Mater. Res. 113-116 (2010) 2323-2328. https://doi.org/10.4028/www.scientific.net/amr.113-116.2323.

[26] C. Ju, J. Lv, A. Wu, Y. Wang, Y. Zhu, J. Chen, Int. J. Food Sci. Technol. 57 (2022) 3556-3566. https://doi.org/10.1111/ijfs.15680.

[27] P. Veiga-Santos, C. Ditchfield, C.C. Tadini, J. Appl. Polym. Sci. 120 (2010) 1069-1079. https://doi.org/10.1002/app.33255.

[28] S. Bilgiç, E. Söğüt, A. Seydim, Turk. J. Agric. Food Sci. Technol. 7 (2019) 61-66. https://doi.org/10.24925/turjaf.v7isp1.61-66.2705.

[29] M.H. Wathon, N. Beaumont, M. Benohoud, R.S. Blackburn, C.M. Rayner, Color. Technol. 135 (2019) 5-16. https://doi.org/10.1111/cote.12385.

[30] S. Saha, S. Ganguly, D. Sikdar, Int. J. Mod. Trends Sci. Technol. 6 (2020) 54-60. https://doi.org/10.46501/IJMTST061211.

[31] L. Sanhueza, R. Melo, R. Montero, K. Maisey, L. Mendoza, M. Wilkens, PLoS One 12 (2017) e0172273. https://doi.org/10.1371/journal.pone.0172273.

[32] M.I. Cantika, A. Hendrawan, eProc. Art Des. 8 (2021) 3616-3632. ISBN: 2355-9349. https://openlibrarypublications.telkomuniversity.ac.id/index.php/artdesign/article/view/16993.

[33] B. Annesha, F. Ciptandi, eProc. Art Des. 7 (2020) 3957-3976. ISBN: 2355-9349. https://openlibrarypublications.telkomuniversity.ac.id/index.php/artdesign/article/view/12966.

[34] W.D. Rahmaningtyas, A. Hendrawan, M.S. Ramadhan, eProc. Art Des. 8 (2021) 3601-3615. ISBN: 2355-9349. https://openlibrarypublications.telkomuniversity.ac.id/index.php/artdesign/article/view/16992.

[35] K. Amutha, S.G. Annapoorani, Asian Dyer 16 (2019) 35-39. ISSN: 0972-9488

[36] S. Dasgupta, S. Ghosh, Trends Text. Eng. Fashion Technol. 2 (2018) 217-222. https://doi.org/10.31031/TTEFT.2018.02.000546.

[37] N.N. Patil, A.G. Datar, Color. Technol. 132 (2016) 98-103. https://doi.org/10.1111/cote.12193.

[38] S. Manyim, A. Kiprop, J.I. Mwasiagi, A.C. Mecha, Tekstilec 66 (2023) 38-46. https://doi.org/10.14502/tekstilec.65.2022072.

[39] F. Ng, K.R. Kim, J. Hu, J. Zhou, Text. Res. J. 84 (2014) 1820-1828. https://doi.org/10.1177/0040517514527377.

[40] M. Rekaby, A.A. Salem, S.H. Nassar, J. Text. Inst. 100 (2009) 486-495. https://doi.org/10.1080/00405000801962177.

[41] A.D. Pranta, M.T. Rahaman, Nano-Struct. Nano-Objects 39 (2024) 101243.

https://doi.org/10.1016/j.nanoso.2024.101243.

[42] F. Ahmed, M.R. Repon, A.D. Pranta, S.R. Yasar, F. Rakib, I. Ahmed, T.A. Emon, T.A. Nishat, SPE Polym. 6 (2025) e10159. https://doi.org/10.1002/pls2.10159.

[43] A. Krol, R. Amarowicz, S. Weidner, J. Plant Physiol. 189 (2015) 97-104. https://doi.org/10.1016/j.jplph.2015.10.002.

[44] Y. Tao, Z. Zhang, D.W. Sun, Ultrason. Sonochem. 21 (2014) 1461-1469. https://doi.org/10.1016/j.ultsonch.2014.01.029.

[45] J. Azmir, I.S.M. Zaidul, M.M. Rahman, K.M. Sharif, A. Mohamed, F. Sahena, M.H.A. Jahurul, K. Ghafoor, N.A.N. Norulaini, A.K.M. Omar, J. Food Eng. 117 (2013) 426–436. https://doi.org/10.1016/J.JFOODENG.2013.01.014

[46] D. Grujić, A. Savić, Lj. Topalić-Trivunović, M. Bizjak, A. Velemir, J. Milanović, J. Tex. Inst. 114 (2022) 1206-1217. https://doi.org/10.1080/00405000.2022.2114287.

[47] M. Ivanović, D. Grujić, J. Cerar, M. Islamčcević Razboršek, Lj. Topalić-Trivunović, A. Savić, D. Kočar, M. Kolar, Antioxidants 11 (2022) 724. https://doi.org/10.3390/antiox11040724.

[48] European Committee for Antimicrobial Suscepti-bility Testing (EUCAST) of the European Society of Clinical Microbiology and Infectious Diseases (ESCMID), Clin. Microbiol. Infect. 6 (2000) 509–515. https://doi.org/10.1046/j.1469-0691.2000.00142.x.

[49] J.H. Ortez, Manual of Antimicrobial Susceptibility Testing, American Society for Microbiology, Washington (2005), p. 39-53, ISBN 1555813496.

[50] K. Wolfe, X. Wu, R.H. Liu, J. Agric. Food Chem. 51 (2003) 609-614. https://doi.org/10.1021/jf020782a.

[51] M. Alberto, M. Canavosio, M. Nadra, Electron. J. Biotechnol. 9 (2006) 205-209. https://www.ejbiotechnology.info/index.php/ejbiotechnology/article/view/v9n3-1.

[52] C.T. Somers, M.E. Evans, J. Sci. Food Agric. 28 (1977) 279-287. https://doi.org/10.1002/jsfa.2740280311.

[53] I.F.F. Benzie, J.J. Strain, Anal. Biochem. 239

(1996) 70-76. https://doi.org/10.1006/abio.1996.0292.

[54] C.M. Liyana-Pathirana, F. Shahidi, J. Agric. Food Chem. 53 (2005) 2433-2440. https://doi.org/10.1021/jf049320i.

[55] R. Re, N. Pellegrini, A. Proteggente, A. Pannala, M. Yang, C. Rice-Evans, Free Radical Biol. Med. 26 (1999) 1231-1237. https://doi.org/10.1016/s0891-5849(98)00315-3.

[56] J. Saha, R. Ara, A.D. Pranta, S. Hossain, J Vinyl Addit Technol. 30 (2024) 1659-1671. https://doi.org/10.1002/vnl.22150.

[57] C. Gauche, E.da S. Malagoli, M.T. Bordignon Luiz, Sci. Agric. (Piracicaba, Braz.) 67 (2010) 41-46. https://doi.org/10.1590/S0103-90162010000100006.

[58] F. Momotaz, R. Repon, U.S. Prapti, A.D. Pranta, R. Hasan, Cellulose 32 (2025) 261-273. https://doi.org/10.1007/s10570-024-06270-4.

[59] B. Ružičić, D. Grujić, B. Škipina, M. Stančić, Đ. Vujčić, M. Dragić, Proceedings, in Proceedings of 11th International symposium on graphic engineer-ing and design "GRID 2022", Novi Sad, Serbia (2022), p. 755-761. https://doi.org/10.24867/GRID-2022-p83.

[60] ISO 20645:2004 (2018) Textile fabrics - Determina-tion of antibacterial activity - Agar diffusion plate test

[61] C. Wiegand, M. Abel, P. Ruth, P. Elsner, U.C. Hipler, J. Mater. Sci.:Mater. Med. 26 (2015) 18. https://doi.org/10.1007/s10856-014-5343-9.

[62] F. Campos, J. Couto, T. Hogg, J. Appl. Microbiol. 94 (2003) 167-174. https://doi.org/10.1046/j.1365-2672.2003.01801.x.

[63] R. Fernández-Pérez, S. Ayuso, C. Moreta, M.-J. Saiz-Abajo, M. Gastón Lorente, F. Ruiz-Larrea, C. Tenorio, Foods 14 (2025) 17. https://doi.org/10.3390/foods14010017.

[64] R. Brouillard, B. Delaporte, J. Am. Chem. Soc. 99 (1977) 8461-8468. https://doi.org/10.1021/ja00468a015.

BRANKA RUŽIČIĆ[1],

DRAGANA GRUJIĆ[1],

ALEKSANDAR SAVIĆ[1],

LJILJANA TOPALIĆ-
TRIVUNOVIĆ[1],

ANA VELEMIR[1],

BLANKA ŠKIPINA[1],

SANDRA DEDIJER[2],

MILJANA PRICA[2]

[1]Univerzitet u Banjoj Luci,
Tehnološki fakultet, Banja Luka,
Bosna i Hercegovina

[2]Univerzitet u Novom Sadu, Fakultet
tehničkih nauka, Novi Sad, Srbija

EKSTRAKT TROPA GROŽĐA KAO BOJA ZA ŠTAMPU TEKSTILNIH MATERIJALA

Smanjenje negativnog uticaja sintetičkih boja na životnu sredinu i ljudsko zdravlje dovela je do razvoja ekološki prihvatljivih tehnika štampe i upotrebe prirodnih boja u tekstilnoj industriji. Trop grožđa je važan otpadni materijal u proizvodnji vina i opsežno se proučava zbog značajnog sadržaja jedinjenja sa biološkim svojstvima, posebno antocijanina, pigmenata odgovornih za crvenu, ljubičastu i plavu boju grožđa. Cilj ovog rada bio je da se ispita potencijalna upotreba prirodne boje ekstrahovane iz tropa domaće sorte grožđa crna mirisavka (GPCM) u pripremi alginatne paste sa limunskom i taninskom kiselinom za štampanje pamučnih tkanina. Posebna pažnja posvećena je postizanju procesne boje magenta podešavanjem pH vrijednosti dobijenog ekstrakta. Prirodna boja iz GPCM ekstrahovana je maceracijom sa 80% metanolom, nakon čega je uslijedila sonifikacija radi povećanja prinosa bioaktivnih jedinjenja. GPCM ekstrakt je pokazao značajnu antioksidativnu aktivnost mjerenu FRAP, DPPH i ABTS+ testovima, i umjerenu antibakterijsku aktivnost protiv Staphylococcus aureus i Escherichia coli. U zavisnosti od pH vrijednosti ispitana je stabilnost antocijanina u GPCM ekstraktu, koja je pokazala magenta ton pri kiselom pH (pH 2-4) i degradaciju boje pri višim pH vrijednostima. Pamučna tkanina štampana sa dvije različite koncentracije GPCM ekstrakta (100 mg/L i 50 mg/L) pokazala je dobru antioksidativnu i antibakterijsku aktivnost. Na osnovu dobijenih rezultata, može se zaključiti da je GPCM ekstrakt ekološki prihvatljivo rješenje za razvoj antibakterijskog i antioksidativnog tekstila, sa potencijalnom primjenom u proizvodnji zaštitne odjeće u zdravstvenim ustanovama, kao i za proizvodnju dekorativnog kućnog tekstila, dječijih igračaka i tekstila za pakovanje.

Ključne reči: ekstrakt tropa grožđa; antibakterijska aktivnost; antioksidativna svojstva; antocijani; pH stabilnost; sito štampa.